A TENDON MODEL USING MECHANICAL OVERLOAD CAUSES DEGENERATIVE MULTISCALE CHANGES IN STRUCTURE AND FUNCTION

by

Ellen T. Bloom

A dissertation submitted to the Faculty of the University of Delaware in partial fulfillment of the requirements for the degree of Doctor of Philosophy in Biomedical Engineering

Winter 2023

EVALUATING OVERLOAD TENDINOPATHY THROUGH MULTISCALE TENDON MECHANICS, STRUCTURE, AND DAMAGE

by

Ellen T. Bloom

Approved: ____
Kristi Kiick, Ph.D.
Chair of the Department of Biomedical Engineering

Approved: ____
Levi T. Thompson, Ph.D.
Dean of the College of Engineering

Approved: ____
Louis F. Rossi, Ph.D.
Vice Provost for Graduate and Professional Education and
Dean of the Graduate College

I certify that I have read this dissertation and that in my opinion it meets the academic and professional standard required by the University as a dissertation for the degree of Doctor of Philosophy.

Signed: ______________________________

Dawn M. Elliott, Ph.D.
Professor in charge of dissertation

I certify that I have read this dissertation and that in my opinion it meets the academic and professional standard required by the University as a dissertation for the degree of Doctor of Philosophy.

Signed: ______________________________

Elise Corbin, Ph.D.
Member of dissertation committee

I certify that I have read this dissertation and that in my opinion it meets the academic and professional standard required by the University as a dissertation for the degree of Doctor of Philosophy.

Signed: ______________________________

Michael H. Santare, Ph.D.
Member of dissertation committee

I certify that I have read this dissertation and that in my opinion it meets the academic and professional standard required by the University as a dissertation for the degree of Doctor of Philosophy.

Signed: ______________________________

Karin Grävare Silbernagel, Ph.D.
Member of dissertation committee

ACKNOWLEDGMENTS

First, I would like to acknowledge my thesis advisor, Dr. Dawn Elliott, for her exceptional guidance encouragement during my graduate studies journey. I relied on her during my time at University of Delaware for not only scientific mentorship, but personal and professional support as well. I have learned to be a more resilient, inquisitive, innovative, and insightful engineer and researcher as a result of her astute judgement and expertise. I decided to enroll at the University of Delaware after meeting with her and with the intention of joining her lab, and my initial assessment of her as a generous, innovative, and eminent researcher couldn't have been more correct. I am beyond thankful for the training and guidance I received from her as I continue in my professional career.

I would also like to thank other individuals who aided me in the genesis and completion of this dissertation. First, I would like to thank the rest of my committee for their insightful direction, feedback, and advice in constructing this body of work, as well as their generous mentorship beyond my research. They were always willing to answer questions or engage in discussion when I needed assistance and were always enthusiastic about my proposed directions. I would also like to extend a warm thank you to Dr. Jeffery Caplan, Jean Ross, Shannon Modla, Chandran Sabanayagam, and the rest of the DBI staff for their extensive knowledge, generous assistance, and advice, as many of the imaging techniques and analysis in this work would not have come to fruition without them. I would also like to thank Dr. Justin Parreno, for his extensive advisement and collaboration in pushing my research forward, which was instrumental to my completion of this work. I would also like to thank my undergraduate students, Emily Eichenlaub, Alyssa Giordani, and Erin Krassan, for their dedicated efforts in assisting me with the work in this dissertation.

I would also like to thank many of my colleagues whom I worked and spent most of my time with at Delaware. I would especially like to thank the current Elliott Lab members Dr. John Peloquin, Kyle Meadows, Harrah Newman, Lily Lin, and Milad Imeni for the many hours of discourse and coffee breaks they were willing to engage in the concepts and techniques that were necessary for me to complete this dissertation. I have extra gratitude for Kyle Meadows and Harrah Newman with our extensive overlapping time in the lab, and Lily Lin for her participation in the work in this thesis and her friendship. I would also like to thank former Elliott Lab members Dr. John DeLucca, Dr. Andrea Lee, and Dr. Babak Safa for the same, as well as their mentorship. Finally, I would like to extend my gratitude to Dr. Victor Barocas and Dr. Julia Quindlen-Hotek for the opportunity to conduct my undergraduate research which influenced my current path, as well as their continuing support and guidance.

Finally, I would like to express my eternal gratitude to my friends and family who have unwaveringly supported me throughout this endeavor. I would like to thank my mother, father, brother, grandparents, and the rest of my family for their love and strength. My decision to pursue my doctoral research 1,200 miles from any family is one that was difficult for me to make, but one that was made possible by their constant support. Finally, I want to thank my closest friends including Jamie Benson, Cailin Gonyea, Elise Hoover, Samantha Harding, and Katelyn Holmquist for their friendship, love, support, and numerous phone calls behind the scenes.

This thesis is dedicated to my parents.

TABLE OF CONTENTS

Appendix

LIST OF TABLES

LIST OF FIGURES

ABSTRACT

Tendon injuries are exceedingly common and afflict 16.4 million people yearly in the United States. As tendons are involved with all movement, these injuries can be debilitating for everyday life. Frequent among these injuries include tendon rupture and tendinopathy, both arising from excess mechanical loading to the tissue, leading to damage and degeneration. Tendon degeneration and mechanical damage are widely referred to as an overuse injury, with little distinction in the clinical or research communities between the magnitude of load (overload) or the number of cycles (overuse) as the injury mechanism. Because the clinical presentation between tendinopathy and tendon rupture are quite different, it is likely that different mechanisms and pathways lead to the end-stage degenerative state. Overuse and overload injuries develop over months in humans and early changes are not detectable, necessitating the use of animal models to evaluate the structural and mechanical changes throughout the degenerative process. However, animal models used to study tendon degeneration are mostly focused on overuse. As a result, it remains unknown how overload, in the absence of overuse, leads to tendon degeneration. Without a full understanding of the multiscale structure-function relationship and damage of tendon, treatments and interventions are doomed to remain ad hoc and not founded in rigorous physiology or etiology.

This dissertation addresses this gap in understanding the progression of degeneration by using novel multiscale structural and functional techniques in combination with an *in vivo* model of tendon overload. To help researchers and

clinicians discuss and interpret the complexities of tendon loading and tendon injuries, a new visual framework for use in the field was also designed. In one of the aims in this dissertation, we were able to assess tendon structural and functional degeneration in our *in vivo* surgical model of tendon overload using activity monitoring, high-resolution MRI, histology, confocal microscopy, Serial Block Face Scanning Electron Microscopy, and multiscale mechanical testing. To ensure that we were accurately describing physiological damage, we first evaluated the effect of bathing solution osmolarity on *ex vivo* tendon mechanics. To measure collagen fibril geometry from a volumetric sample, we also developed a method using electron microscopy and machine learning to determine the 3D ultrastructure of collagen fibrils in dense tendon samples. From these three aims, we determined that bathing solutions which prevent tissue swelling result in more accurate tendon mechanics; successfully measured collagen fibril geometry in 3D tendon samples; and confirmed that our model of *in vivo* overload induced degenerative structural changes and impaired mechanical function of tendon.

The outcomes of this dissertation established an *in vivo* model to study overload-induced degeneration, separate from overuse, and will be used to study mechanisms and treatments for tendon overload injuries. The novel tools developed in this dissertation will be used in future research studying structure-mechanics studies of tendon and other highly aligned, collagenous soft tissue, as well as improving treatments and prevention strategies for tendon injuries.

Chapter 1

INTRODUCTION

Tendons are fibrous connective tissues which transfer load between muscle and bone to facilitate movement. Tendon is primarily made up of highly aligned collagen, which enables it to withstand high magnitudes of mechanical forces over long durations [1–4]. These high mechanical demands make tendons susceptible to degeneration, or tendinosis. Degeneration can lead to two highly prevalent disorders: tendinopathy and tendon rupture. Tendinopathy is a combination of degeneration and pain [5,6], while tendon rupture occurs suddenly without early pain symptoms [7–10]. As tendinopathy and rupture are both increasing in incidence, improved prevention and rehabilitation strategies are necessary [11–13]. Currently, the distinction between the underlying mechanisms and progression of degeneration leading to either painful tendinopathy or acute rupture is not well elucidated, leaving clinical intervention difficult.

Tendon degeneration and mechanical damage has been studied using a variety of ex vivo explant testing and in vivo animal models [14–17]. Due to tendon's hierarchical structure, multiscale structural and mechanical assays are necessary to fully describe the changes that occur with degeneration [18–27]. Animal models are useful as they allow for control of mechanical loading and usage of numerous assays. However, there is little distinction within research as to the effect of increasing loading magnitude (overload) and loading cycle number or duration (overuse). Most animal studies are focused on increasing only loading cycles to induce degeneration

[28–34]. A clear inquiry on the effect of increasing loading magnitude on tendon degeneration would further elucidate the environment which leads to tendon injury and help describe the different mechanisms which determine whether degeneration leads to rupture or tendinopathy.

Thus, this thesis will investigate the structural and functional changes induced by studying the multi-scale mechanics of tendons and hierarchical structure following in vivo overload. Chapter 2 will include pertinent background information to illuminate the significance of the dissertation and contribution to the field. Chapter 3 will study the effect of bathing solution osmolarity on multiscale mechanics and damage mechanisms of tendon explants, to determine which testing conditions best recapitulate the tendon physiological environment. A novel method using serial block face scanning electron microscopy (SBF SEM) to evaluate 3D tendon collagen fibrillar geometry will be presented in Chapter 4. Chapter 5 will focus on the multiscale structural and functional changes which occur in tendon following overload in a surgical rodent model and introduce a new visual framework to separate overload and overuse in tendon loading. Finally, Chapter 6 will provide a summary and conclusion of this dissertation, and future studies based on the findings of the dissertation are proposed.

Quantification of the contributions of altered loading states to the multiscale tendon degeneration will improve prevention and rehabilitation strategies, as well as identify structural targets for functional regeneration, repair, and replacement. In addition, the novel methods established in this dissertation can also be applied to evaluate other highly aligned, collagenous tissues (e.g., ligament, meniscus, annulus fibrosis) in the future.

Chapter 2

BACKGROUND

Tendon is a hierarchical structure of highly aligned collagen, other matrix components such as proteoglycans, spanning multiple length scales and cells [1,2]. By dry weight, tendon is 65-80% aligned collagen, or Type I, as well as Type III and Type IV [1,3–5]. Tendon has a generally low cellular density, with cells consisting mainly of tenocytes and tendon stem cells [6–8]. The collagen fibrils, the main component of the tissue, seem to span the entire functional length of the tendon, at least within the animal tendons imaged in research, though mechanical experiments show evidence of discontinuous fibrils [9–12]. The diameter distributions of collagen fibrils are dependent on the functional capacity of tendon [13,14], and collagen fibrils in energy-storing tendons have more stable cross-links [15]. The various length scales of tendon structure also exhibit complex geometry, specifically with helical superstructures, as we move from collagen molecules to the whole tendon (Fig 2.1) [15–20]. Collagen molecules consist of a tight triple helix comprised of peptide chains which can also form cross-links with adjacent molecules [21–26]. Some collagen fibrils also twist independently or form double or triple helices with adjacent fibrils [16,27,28]. Collagen fibrils form cross-links with each other via advanced glycation end products (AGEs), as well as interact with tenocytes via integrins [29–32].

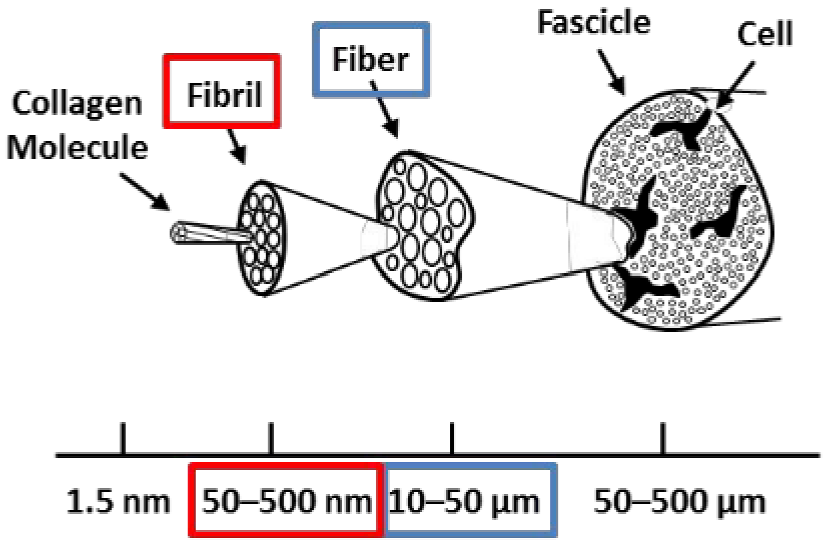

Figure 2.1: Hierarchical tendon structure. Hierarchical structure of tendon showing respective length scales encompassing the collagen molecule, collagen fibril, collagen fiber, and tendon fascicle. [33]

2.1 Tendon Mechanical Function

Tendons are responsible for transferring load from muscle to bone and must support very high loads and high frequencies of loading during normal motion throughout their lifespan. Under tensile loading, tendon exhibits a characteristic nonlinear S-curve with a toe-region as collagen fibrillar crimp straights out, a linear region of recoverable loading, and plastic deformation as collagen fibrils are damaged with a decrease in overall load-bearing capacity until failure or rupture (Fig 2.2) [13,34–37]. The hierarchical arrangement of aligned collagen is the main contributor of tendon's tensile strength [10,38–42]. At the collagen fiber level, tendons experience fibrillar strain and sliding as interfibrillar shear between collagen fibrils aids in load bearing of the tissue [42–44]. Further, the exact mechanical function of tendons is determined by their physiological niche; load-bearing tendons are more fatigue-resistant [45].

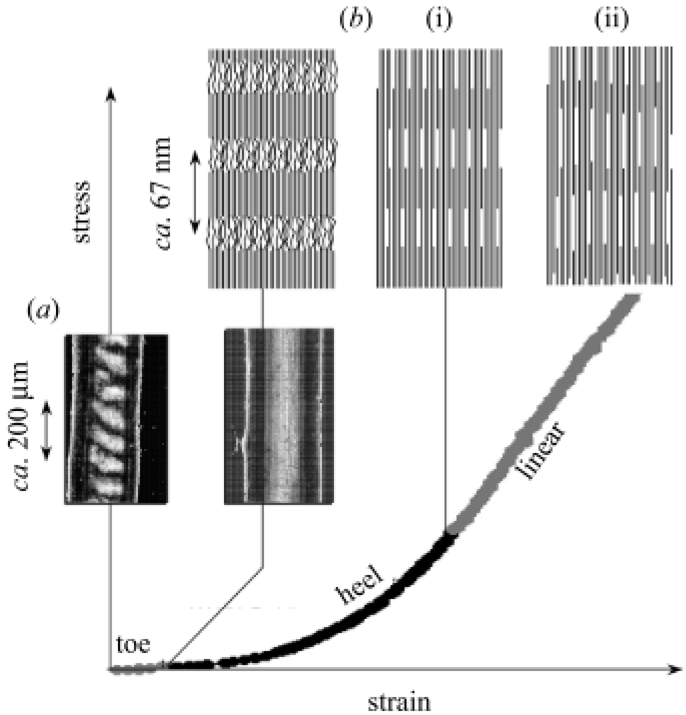

Figure 2.2: Tendon loading curve schematic. Characteristic partial S-curve of tendon showing the macroscopic crimp of tendon straightening out (*a*¸viewed with Raman spectroscopy) and illustrating the gliding of collagen fibrils (*b(i-ii)*) [46].

2.2 Tendon Structure-Function Relationships

Tendon's hierarchical structure leads to differences in mechanical behavior across the length scales. Loading curves appear to become more nonlinear, and Young's modulus increases when comparing a collagen molecule, tendon collagen fibril, and whole tendon (Fig 2.3) [36]. Similarly, applied strain decreases from the macroscale (whole tendon, ~cm) to the microscale (collagen fiber, ~100 µm) [11,43,47]. Various structural changes across the hierarchy can lead to changes in the macroscale function. An increase in collagen fiber cross-links (AGEs) reduces fiber sliding and viscoelasticity [23,30,48]. Reduction of specific proteoglycans, either with enzymes or genetic models, either decreased or had no effect on tendon mechanics [41,49,50].

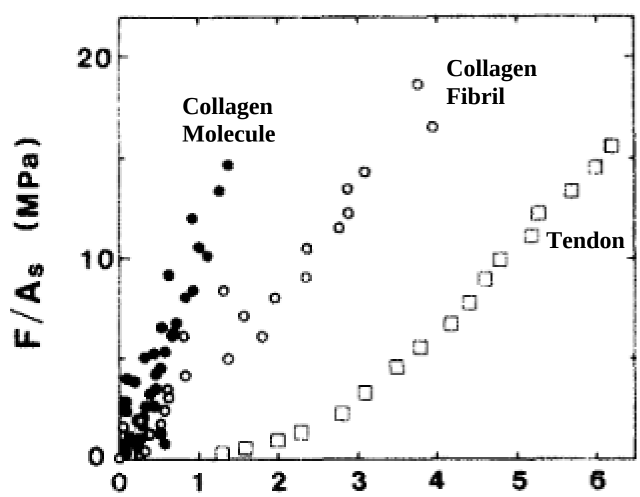

Figure 2.3: Multiscale tendon stress-strain curves. Comparison of force-strain curves for a collagen molecule (filled circles), collagen fibril (open circles), and tendon (open boxes). [36]

2.3 Tendon Damage, Tendinopathy, and Tendinosis

Tendon is susceptible to damage during mechanical loading, as collagen fibrils first plastically deform into “kinks”, and eventually rupture with increasing strains [2,34,35,51,52]. This is observed functionally as a loss in mechanical properties, specifically modulus, as well as microscale damage measures such as non-recoverable fiber sliding and collagen fibril denaturation [43,47,52–55]. *In vivo*, this local microscale damage is either repaired as a part of tendon maintenance or leads to tendon pathology when tendon’s healing capacity is overcome (Fig 2.4) [26,29,51,54,56–59].

Underloading tendon also leads to functional deficits, and thus the loading environment of tendon can also be considered as a linear continuum (Fig 2.5) [60]. Tendon’s healing capacity is somewhat limited, due to its low cellularity, lack of vascularization, and low collagen fibril turnover [61]. Accumulation of microdamage is widely understood to lead to tendinosis and tendinopathy. There is a lack of consensus within the field whether cellular dysregulation from excess load leads to impaired matrix, or impaired matrix leads to cellular dysregulation, but both contributors are involved in degeneration [29,62]. Tendinosis is degeneration of both tendon structure and function resulting from excess mechanical loading. Tendinopathy is any tendon pathology which causes pain and may result from tendinosis [63–65].

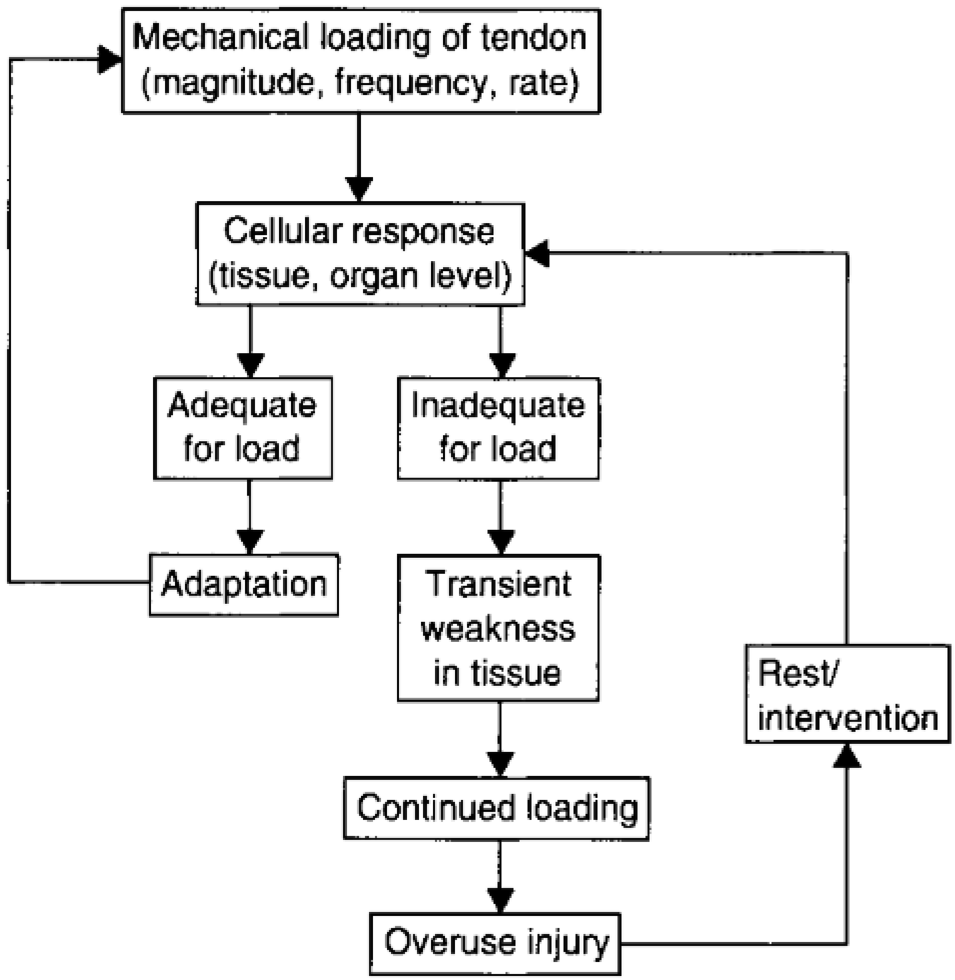

Figure 2.4: Model of tendinopathy initiation. Schematic showing divergent pathways to tendon adaptation or tendon degeneration. [59]

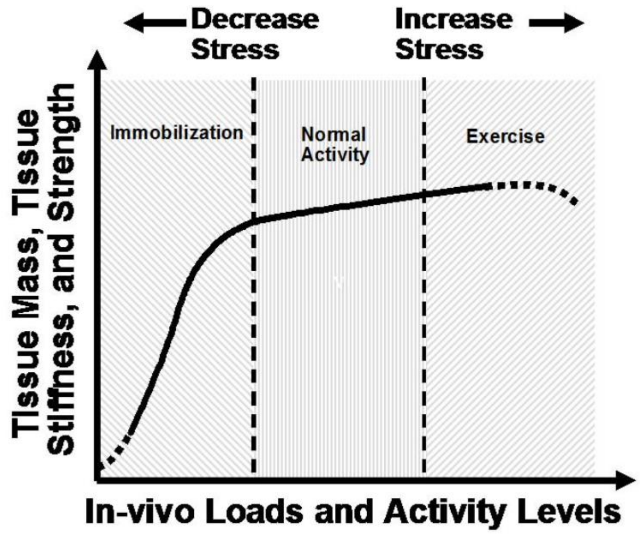

Figure 2.5: Tendon physiological loading curve. Continuum of structural and functional changes occurring with varying loading environments in tendon. [60]

2.4 Tendon and Altered Loading

When the loading environment of tendon is changed, tendon structure remodels in response. This adaptation can be positive and return the tissue to homeostasis, or degenerative and lead the tissue towards impairment. The thresholds between positive adaptation or degeneration are neither fully defined nor equally explored for different altered loading environments, and further, altered loading can be generally divided into underload or overload.

Underloading or fully unloading tendons induces changes in tendon structure, including a reduction in glycosaminoglycan content [66], increase in fibrillar adhesion [67], inconclusive changes in collagen content either increasing [67] or remaining unchanged [68] but a decrease in collagen fibril diameter [68], and a short-term decrease in tendon CSA following unloading [69]. An overall decrease in mechanical function has also been observed in numerous studies [66,68,70–74]. Underload starves tendon of necessary mechanical load for homeostasis, resulting in degeneration without increasing microdamage. It is not clear that there is any beneficial, or subthreshold, amount of unloading for tendon [66,75,76].

Increasing tendon load with well-structured exercise within the physiological range reinforces tendon by making the tissue larger and increasing mechanical strength [77–81]. However, defining a universal demarcation between positive adaptation and pathological response is difficult, due to its dependence on highly variable intrinsic and extrinsic factors such as individual age, genetic factors, environmental conditions, heavy activity levels, or other systemic diseases [29,82,83].

Excessive overload to tendon results in degeneration including heterogeneous thickening of the tendon [2,29,84], changes in cellular density and cellular morphology show an alteration of the tendon composition to a more chondrocyte-like morphology [2,62,85,86], disorganization of collagen [87–92], neovascularization [92,93], and changes in proteoglycan content [94–96]. Mechanically, a reduction in tendon modulus and strength have been observed [90,97–101].

2.5 Animal Models of Tendinosis

Evaluating the progression of tendon injuries in humans is a difficult talk, as tendon degeneration does not typically with pain or symptoms until damage is already widespread [29]. As a result, animal models are essential to studying the initiation and progression of tendon degeneration [102–104]. Animal models which alter tendon loading and keep the tendon intact are useful for tendinosis etiology, as it allows for observation and investigation of controlled overload over time, as well as the use of destructive experimental assays to evaluate structural and mechanical tissue changes.

Tendons can be unloaded in vivo by lower limb suspension [75,76], casting/wiring [66,105] , immobilization via Botox [67,106–108], surgical intervention [108–110], and the removal of gravity via spaceflight [68,69,111]. While unloading is an interesting state of altered loading, due to tendon's intended function of supporting loads, mechanical environments that increase tendon loading are more valuable for understanding underlying mechanisms and injury pathways.

Tendons can be exposed to excess mechanical load *in vivo* by treadmill running, direct tendon loading, and forced muscle contraction [102,103,112–114]. Direct tendon loading has the advantage of controlling the applied load and frequency but has a limited time course for use due to animal use guidelines for anesthesia [115–118]. Treadmill running has the advantage of increasing frequency of load and keeping the tendon intact and is widely used to study tendon injuries resulting from excess mechanical use [98,119–122]. However, treadmill running combines increasing frequency and load, especially if on an incline. Exercise can also cause systemic stress such as increased serum corticosterone [123], and the remodeling results may be variable depending on exercise regimen [124]. In all these models, tendon overloading is accomplished by increasing the frequency of loading on the tendon. To investigate remodeling changes occurring from simple overload without increasing frequency, a different model is needed.

Synergistic ablation (SynAb) is a surgical animal model originally developed to study muscular hypertrophy [125–131]. Rat plantaris tendon, the tendon of interest, is overloaded by surgically ablating the synergist Achilles tendon. The plantaris tendon then experiences an excess of load without increasing the number of loading cycles, as animals are allowed to maintain typical activity levels. This model has been applied to investigating tendon changes as well, but only shortly after surgical intervention [132–135].

2.6 Research Objectives

The objectives of this thesis were to investigate the structural and mechanical changes that occur when tendon is overloaded using a novel animal model. First, multiscale mechanical testing was conducted on healthy rat tail tendons to determine which bathing solution for mechanical testing best preserves *in vivo* damage conditions. Serial Block Face Scanning Electron Microscopy and successful implementation of a U-Net machine learning for collagen fibril segmentation and reconstruction was used to investigate the difference between positional and load-bearing tendons, as well as differences in complex fibrillar geometry in the different regions of healthy tendon. A novel surgical rat model, Synergist Ablation, was established to overload the plantaris tendons of rat without increasing loading frequency. The structural changes occurring from overload were assessed with longitudinal MRI measures, histology, serial block face scanning electron microscopy (SBF-SEM), and second harmonic generation (SHG); while the mechanical changes occurring from overload were assessed with multiscale mechanical testing and these were assessed with microscale SBF-SEM structure.

Chapter 3

TENDON MULTISCALE STRUCTURE, MECHANICS, AND DAMAGE ARE AFFECTED BY OSMOLARITY OF BATH SOLUTION

Based on published work: Bloom, ET; Lee, AH; Elliott, DM. "Tendon Multiscale Structure, Mechanics, and Damage are Affected by Osmolarity of Bath Solution," Annals of Biomedical Engineering, **2020,** 1-11. *Reproduced with permission from Springer Nature.*

3.1 Introduction

Bath solutions are frequently necessary during tissue mechanical testing to maintain tissue hydration, mechanics, and microstructure. One of the most common bath solutions used for tendon and other musculoskeletal samples is phosphate buffered saline (PBS). However, even at physiological concentrations (15 mM), PBS causes tissue swelling. In tendon, this swelling results in decreased tendon modulus and induces microstructural changes [136,137]. SEM images of tendon equilibrated in PBS show that collagen fibril diameter is increased and fibril packing density is decreased in rat tail tendon [137]. The swelling effect of PBS has been observed in collagenous other tissues as well, including ligament, annulus fibrosus, and meniscus [138–140]. Along with inducing swelling, solutes present in buffer may diffuse into tissue and alter structure and mechanics [141–145].

With evidence of PBS solution altering tissue-level mechanics and microscale structure, is it critical to evaluate the multiscale mechanical behavior of tendon under these conditions. We have previously investigated multiscale mechanics and damage in tendon by comparing sequential loading curves and microscale recovery [11,44,47].

In these experiments, microscale damage was related to changes in tissue-level mechanical parameters after loading. By using a similar multiscale approach, it is possible to link the observed PBS related changes in structure to changes in mechanical behavior.

For many tests, using a bath solution is not optional, either as a result of sample cross section or test duration. The duration of our multiscale experiments is long enough that a buffer solution is necessary to avoid tissue drying (> 55 minutes), thus no buffer-free "fresh" control can exist. Our group previously investigated possible bath alternatives to PBS. We showed that a combination of 8% weight polyethylene glycol (PEG) by volume of Tris-buffered saline maintained physiological levels of tissue hydration [146]. PEG was selected because the available large particle size (~20 kDa) does not readily diffuse into the tissue [147,148]. In addition to its large size restricting diffusion, PEG is a hydrophilic polymer, contributing to its ability to maintain tissue hydration [50,149–151]. Using the PEG and saline solution (SPEG) as a bathing solution to prevent swelling facilitates investigation of the difference in mechanics between swollen and non-swollen tissue. Previous studies on multiscale mechanics and damage were completed with PBS [11,43,44], and understanding this effect of swelling offers a lens to interpret prior work as well as providing information to better design future studies.

The objective of this study was to compare the effects of PBS and 8% SPEG bathing solutions on multiscale tendon mechanics and damage as well as tendon microstructure to understand the effect of osmotic pressure on tendon. We hypothesized that increased tendon swelling due to the use of physiological PBS causes microstructural changes that alter microscale sliding and increase tendon damage during tensile loading compared with a bath that maintains fresh tendon hydration.

3.2 Materials and Methods

3.2.1 Sample Preparation

Rat tail tendon samples were harvested from fresh-frozen female Long-Evans rats, aged 4-7 months, which were obtained from another study not affecting musculoskeletal tissues. The samples were limited to a maximum of 2 freeze-thaw cycles, and a maximum storage time 4 months at -20 ˚C, with all tendons coming from frozen, undissected animals [44]. The entire tail was removed, with the 80 mm proximal section preserved with skin intact. Tendon fascicles were individually removed from the proximal tail portion using forceps. A centimeter from each end of the tendon was removed, to eliminate any tissue possibly damaged during sample preparation. Each sample was stained with a 10 μg/ml solution of DTAF (5-(4,6-Dichlorotriazinyl) Aminofluorescein) (5-DTAF, Life Technologies) for thirty minutes, to prepare the sample for photobleaching [43,44].

3.2.2 Mechanical Testing Protocol

The testing protocol was like that used in prior studies [41,44]. There are known mechanical differences between testing at room temperature and at physiological temperature; however, we completed our experiments at room temperature as we were interested in comparing our results to similar prior studies [41,43,44,47,136,146,152,153]. Each sample was tested using a custom uniaxial testing device mounted on an inverted confocal microscope (LSM 5 LIVE, objective Plan-Apochromat 10x/0.45), which allows for simultaneous imaging and mechanical loading. The sample was gripped and loaded to a reference length by applying a 5 mN (0.5 g) preload. Each sample was then preconditioned with 5 cycles between 0 and 2% strain. Following preconditioning, four parallel photobleached lines were made on the midportion of the tendon, between the ink markers, equally spaced 200 μm apart. Each sample was then ramped to 6% strain (Baseline), held for 15 minutes at constant 6% grip strain, and unloaded back to the reference length. The sample remained at the reference length for a 40-minute recovery period before undergoing a second ramp (Diagnostic) until failure (Fig 3.1). All loading and unloading rates were 0.1%/sec. We chose 6% strain as our previous study indicated it was sufficient to induce damage [41,44,47]. While the applied grip strain was 6%, post-test optical imaging indicated that tissue strain was 3.9 ± 0.4% and 3.6 ± 0.4% for the PBS and SPEG groups, respectively, with no difference between groups (t-test, $p > 0.1$).

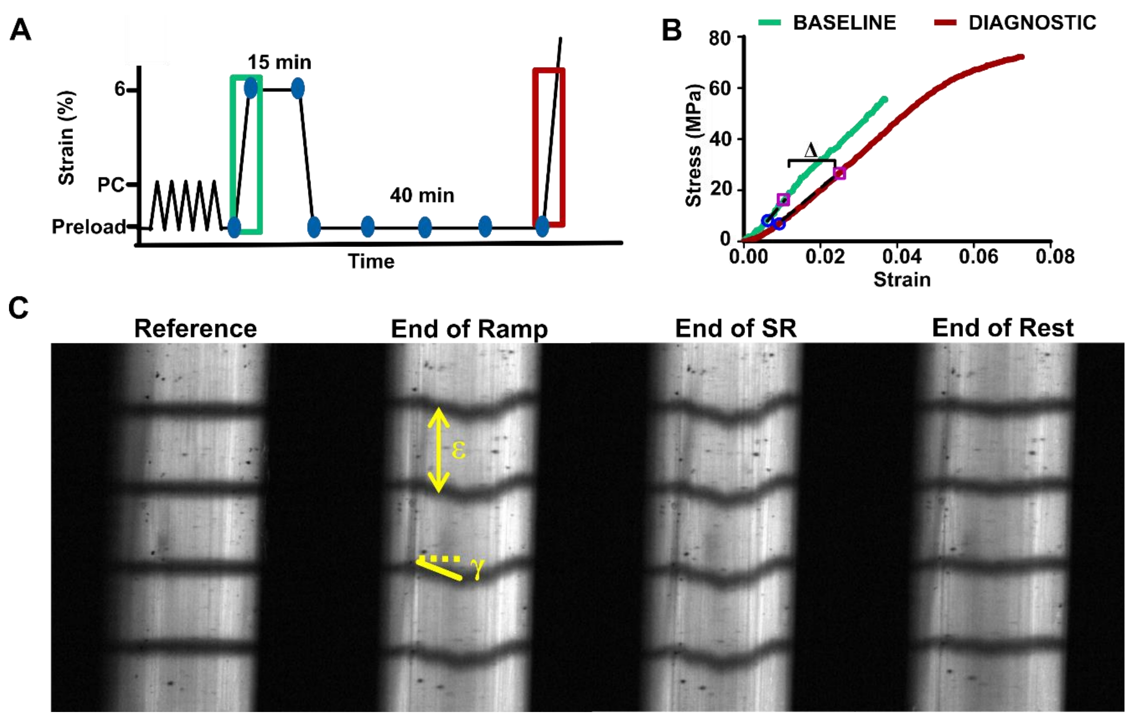

Figure 3.1: Multiscale mechanical parameter quantification. (a) Mechanical loading protocol used in experiment, showing the time points for confocal imaging with blue circles. The Baseline and Diagnostic ramps are indicated in green and red, respectively. (b) A representative stress-strain curve, showing the Baseline and Diagnostic curves. Transition point (blue circle), modulus (dashed line), and inflection point (purple square) are indicated, as well as the Δ value difference between them. (c) Confocal images of a sample tendon at the reference, end of ramp, end of stress-relaxation (SR), and end of rest. Microscale strain (ε) and microscale sliding (γ) are also indicated.

3.2.3 Imaging and Data Acquisition

To measure the tissue strain, we imaged the tendon with a CCD camera to track displacement of the ink markers on the midportion surface using digital image correlation (Vic 2D, Correlated Solutions). For microscale analysis, confocal image stacks were taken after preconditioning, at the beginning and end of loading, immediately after unloading, and every 10 minutes during the recovery (blue dots in Fig 3.1A). The cross-sectional area was calculated using confocal imaging of the major and minor axes of each sample at the reference length and an ellipse fitted to obtain area of the cross-section.

3.2.4 Tissue-Scale Data Analysis

Tissue-level strain (ϵ) was measured from tracking displacement of surface ink markers, while tissue-level stress (σ) was calculated by dividing the tensile force by the initial cross-sectional area. Transition point, inflection point, and linear region modulus were all calculated from the σ-ϵ curve, with the transition point defined as the end of the toe region and inflection point as the change between strain-stiffening and strain-softening behavior (Fig 3.1B). The inflection point was calculated by fitting a cubic smoothing spline with the csaps function in MATLAB and finding the first zero crossing point of the second derivative. The stress-strain curve between zero and the inflection point was fit to a nonlinear exponential constitutive model which was optimized to obtain the transition strain (p), transition stress (q), and linear region modulus (E):

$$\boldsymbol{\sigma} = \begin{Bmatrix} \boldsymbol{A} * (\mathbf{exp}(\boldsymbol{B\epsilon}) - \mathbf{1}), & |\forall \boldsymbol{\varepsilon} \ \leq \boldsymbol{p} \\ \boldsymbol{E} * (\boldsymbol{\varepsilon} - \boldsymbol{p}) + \boldsymbol{q}, & |\forall \boldsymbol{\varepsilon} \ > \boldsymbol{p} \end{Bmatrix} \tag{3.1}$$

The optimization was performed on three of the parameters (p, A, B) and was completed using the MATLAB function fmincon to minimize the mean square error. Optimization was performed for both the Baseline and Diagnostic ramps. The change in these measures between the Baseline and Diagnostic ramp was quantified as a delta value (Δ), of the Baseline – Diagnostic, where a non-zero delta values indicate damage as a result of mechanical loading (Fig 3.1B). Conversely, when Δ=0, or Baseline and Diagnostic measures are the same, no damage is observed.

3.2.5 Microscale Data Analysis

The microscale parameters were measured from the photobleached lines, where the deformation was tracked to calculate microscale strain and sliding. Microscale strain was calculated from the average displacement of the photobleached lines, while microscale sliding was calculated as the average tortuosity of the lines (Fig 1C). Sliding recovery after unloading was decomposed into elastic recovery, viscous recovery, and non-recoverable, using the sliding measured at the end of loading (EL), start of rest (SR), and end of the rest (ER). Elastic recovery, the sliding that immediately recovered after unloading, was calculated as:

$$\text{(EL-SR)/EL} \times 100\% \tag{3.2}$$

The viscoelastic recovery, or the sliding recovered during the rest period after subtracting the elastic recovery, was calculated as:

$$(SR-ER)/EL \times 100\% \tag{3.3}$$

Finally, the non-recoverable sliding was the residual sliding remaining at the end of the rest period, calculated as the sliding value at EL minus the elastic and viscous recovery.

In order to evaluate the strain transfer between the tissue and microscale levels, the ratio of microscale strain to tissue strain was calculated at the end of the Baseline ramp (beginning of stress-relaxation period).

3.2.6 Transmission Electron Microscopy (TEM)

Samples were prepared for TEM without any mechanical testing. Samples were in 3 different groups: PBS, SPEG, and Fresh (n = 3/group). For the PBS and SPEG samples, a single fascicle was bisected, with one half going to each group. Samples in PBS and SPEG were equilibrated in the appropriate buffer for 90 minutes prior to processing, while the Fresh group was processed immediately following dissection. Each sample was fixed with 2% glutaraldehyde and 2% paraformaldehyde in 0.1M sodium cacodylate buffer overnight at 4ºC. The next day, the sample was cut to 1 mm segments and fixed for an additional hour in the fixative solution. The sample spent 2 hours in a 1% osmium tetroxide in 0.1M sodium cacodylate buffer before being washed with DI water three times for 15 minutes each. Next, dehydration was completed in an ascending acetone series, including a 95% acetone step lasting 48 hours (or 2 days). Dehydration was finished with two 30-minute fixations in 100% anhydrous acetone. The sample was finally subjected to multiple ascending steps of first polypropylene oxide and the EMBed-812 Resin before polymerization in a vacuum. After processing, the sample was ultramicrotomed before TEM imaging (Libra 120 TEM, Zeiss). TEM images were segmented manually using GIMP software (GIMP 2.10.12), and the distributions of fibril diameter and area density calculated using FIJI. Images with artifacts or other features which might affect the density calculation, such as cells or large gaps, were excluded.

3.2.7 Statistical Analysis

The difference in mechanical parameters between the SPEG and PBS groups was determined using a two-tailed Student's t-test with significance set to 0.05. A Kolmogorov-Smirnov test was performed to evaluate the normality of all data. Of the forty-eight measured parameters, all were normally distributed except four. The non-normal measured data were PBS Diagnostic Transition Strain, and PBS microscale strain at three of the seven time points. For any comparisons involving these data, a nonparametric two-tailed Mann-Whitney test was used with significance set to 0.05. Additionally, the Δ values comparing the differences between Baseline and Diagnostic between the two ramps in a single group were evaluated using a one-sample t-test to determine if a statistically significant difference from zero existed ($p < 0.05$). All statistical tests were completed in GraphPad Prism.

3.3 Results

3.3.1 Tissue-Scale Parameters

For the tissue-level parameters, we first compared the SPEG and PBS mechanical parameters from the Baseline ramps, which represented a pre-mechanically damaged state (Fig 3.2). The SPEG samples had a higher linear region modulus, consistent with prior literature ($p = 0.0003$). SPEG also had a higher inflection point stress compared to the PBS samples (p = 0.009), while there were no differences between the groups for inflection point strain, transition strain, or

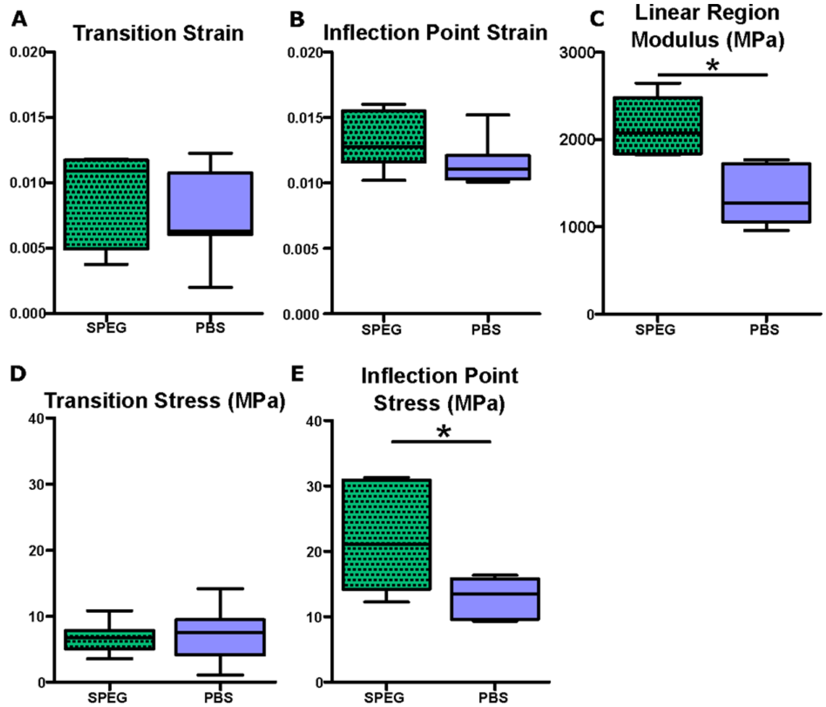

transition stress.

Figure 3.2 Baseline mechanical results. The Baseline values for A) transition strain, B) transition stress, C) inflection point strain, D) inflection point stress, and E) modulus were calculated for both for SPEG (n = 7) and PBS (n=8) groups. There was no difference between groups for transition strain, transition stress, or inflection point strain. * ($p < 0.05$). Error bars represent 95% confidence interval.

In order to compare the effect of swelling on damage in the tissue, the change in mechanical parameters was calculated using a Δ parameter (calculated as difference between Baseline and Diagnostic) (Fig 3.3). A non-zero Δ value indicates tissue-level damage, while a zero Δ indicates no damage induced by mechanical loading. For transition strain, SPEG showed damage, while PBS did not (p= 0.003, p = 0.053).

Consequently, the Δ transition strain was higher in SPEG samples than in PBS ($p = 0.014$). For transition stress, neither group showed damage nor were not different from each other ($p = 0.22$, $p = 0.64$, $p = 0.15$). For inflection point strain, both SPEG and PBS showed damage ($p = 0.007$, $p = 0.001$), though were not different from each other ($p = 0.42$). For inflection point stress, SPEG did not show damage, though PBS did ($p = 0.70$, $p = 0.008$). Consequently, the Δ inflection point stress was higher in PBS ($p = 0.043$). For modulus, both SPEG and PBS showed damage ($p = 0.0002$, $p = 0.006$). Additionally, SPEG showed greater damage than PBS ($p = 0.0002$). This modulus result is consistent with previous work using this loading regime [43,47].

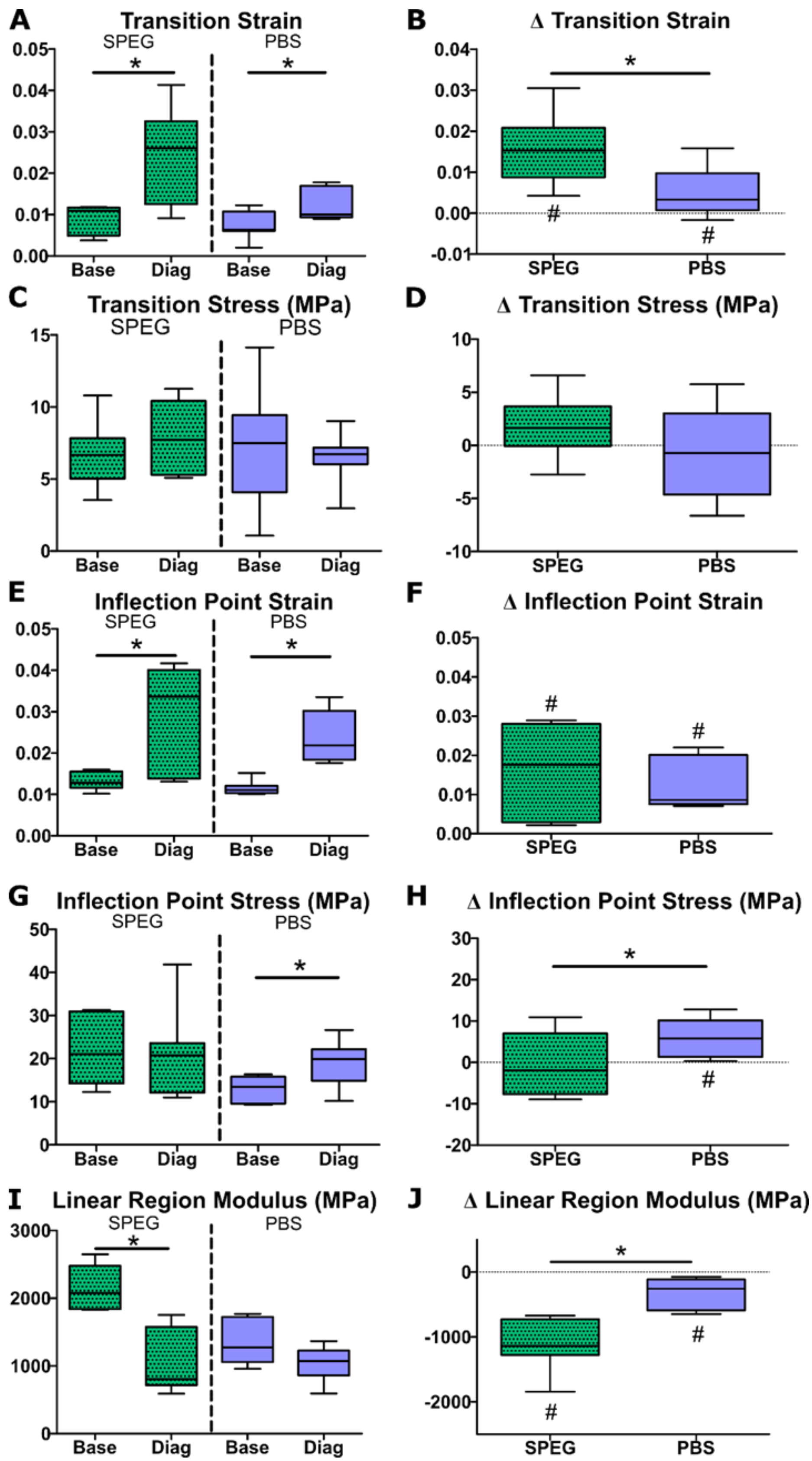
A
Transition Strain
SPEG
PBS
Base
Diag
Base
Diag
B
Δ Transition Strain
SPEG
PBS
C
Transition Stress (MPa)
D
Δ Transition Stress (MPa)
E
Inflection Point Strain
F
Δ Inflection Point Strain
G
Inflection Point Stress (MPa)
H
Δ Inflection Point Stress (MPa)
I
Linear Region Modulus (MPa)
J
Δ Linear Region Modulus (MPa)

Figure 3.3 Baseline and Diagnostic mechanical parameters. The Baseline and Diagnostic values for A) transition strain, B) transition stress, C) inflection point strain, D) inflection point stress, and E) modulus were calculated for both SPEG (n=7) and PBS (n=8). The difference between Baseline and Diagnostic was calculated as a Δ value F-J. * ($p < 0.05$), # significantly different from zero ($p < 0.05$). Error bars indicate the 95% confidence interval.

3.3.2 Microscale Parameters

In order to evaluate the microscale mechanics, we measured mechanical changes using photobleached lines on the midportion of the tendon. Microscale results were calculated for each time point of confocal imaging. Microscale strain was calculated as the average strain between the photobleached lines. SPEG samples experienced higher microscale strain during the end of the ramp ($p < 0.05$), at the end of stress relaxation ($p < 0.05$), and throughout the relaxation period, excepting the time point at 20 minutes ($p = 0.39$) (Fig 3.4A). While neither group returned to zero strain, the SPEG group had a greater partial recovery with a final mean strain of -0.0031 and the PBS group with a final mean strain of -0.0094 (Fig 3.4A). Microscale sliding was calculated as the average tortuosity of the photobleached lines, normalized to the reference measurements. Microscale sliding only partially recovered for both groups and sliding was not different between groups at any time point (Fig 3.4B, $p > 0.10$).

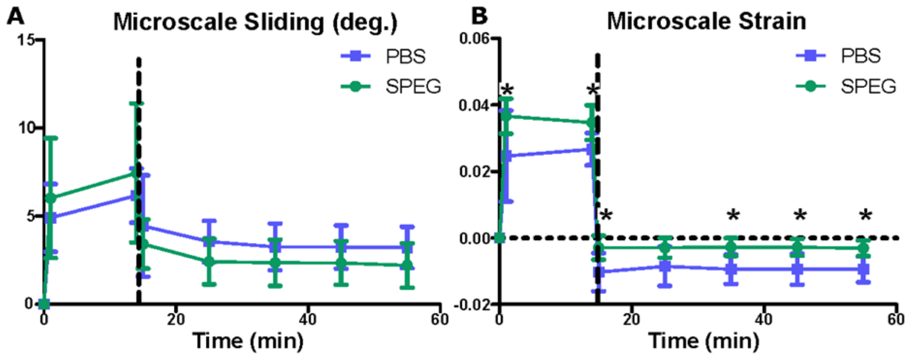

Figure 3.4 Microscale mechanical behavior. Microscale mechanical behavior for SPEG (n=7) and PBS (n=8). A) Both groups experienced partial recovery of microscale strain after unloading, with significantly different magnitudes throughout recovery ($p < 0.02$). This suggests that collagen fibrils experienced more damage with PBS incubation. B) Microscale sliding also showed only partial recovery for both groups. * ($p < 0.05$).

The microscale sliding recovery was decomposed into elastic recovery, viscous recovery, and non-recoverable sliding as described in the methods (Fig 3.5). There was no difference between the groups for both elastic and viscous recovery ($p > 0.20$ and $p > 0.80$). The amount of non-recoverable sliding, a measure for microscale damage, was lower in SPEG samples compared to PBS samples ($p < 0.05$).

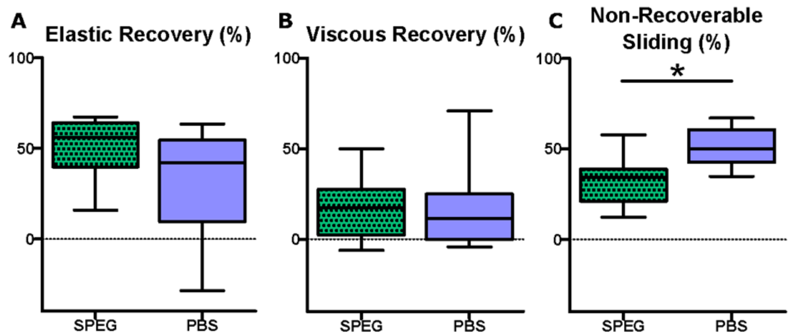

Figure 3.5 Decomposed recovery for microscale sliding. Decomposed recovery for microscale sliding for SPEG (n=7) and PBS (n=8). A) Elastic and B) viscous recovery showed no significant differences between groups. C) Non-recoverable sliding (residual sliding at the end of recovery) was higher in the PBS group. Error bars represent the 95% confidence interval. * ($p < 0.05$).

In order to evaluate the transfer of strain between the different hierarchical levels of tendon, we calculated the strain ratio from the microscale measurements to the tissue-level measurements. The time point for which we have simultaneous strain measurements was at the end of the Baseline ramp. The microscale to tissue strain ratio at this time point was higher in SPEG compared to PBS (Fig 3.6, $p < 0.001$).

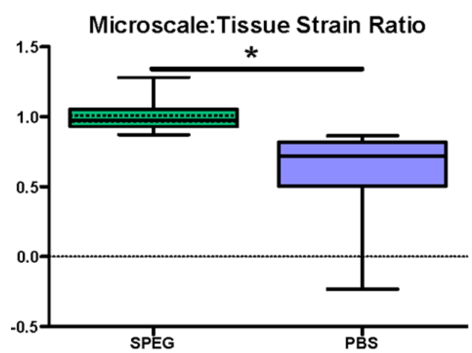

Figure 3.6 Micro: Tissue-scale strain ratio. The microscale strain to tissue strain ratio was calculated at the end of the Baseline ramp for SPEG (n=7) and PBS (n=8). SPEG had a significantly higher Microscale: Tissue ratio compared to PBS. Error bars indicate 95% confidence interval. * ($p < 0.05$).

3.3.3 TEM

Representative images and segmented masks from each group show the effect of bath solution on image quality (Fig 3.7A-F). The distributions of fibril diameters for each group were all found. (Fig 3.7G-I). The medians of the distribution of fibril diameter and the % area density (Fig 3.7J-K) were measured for SPEG, PBS, and Fresh.

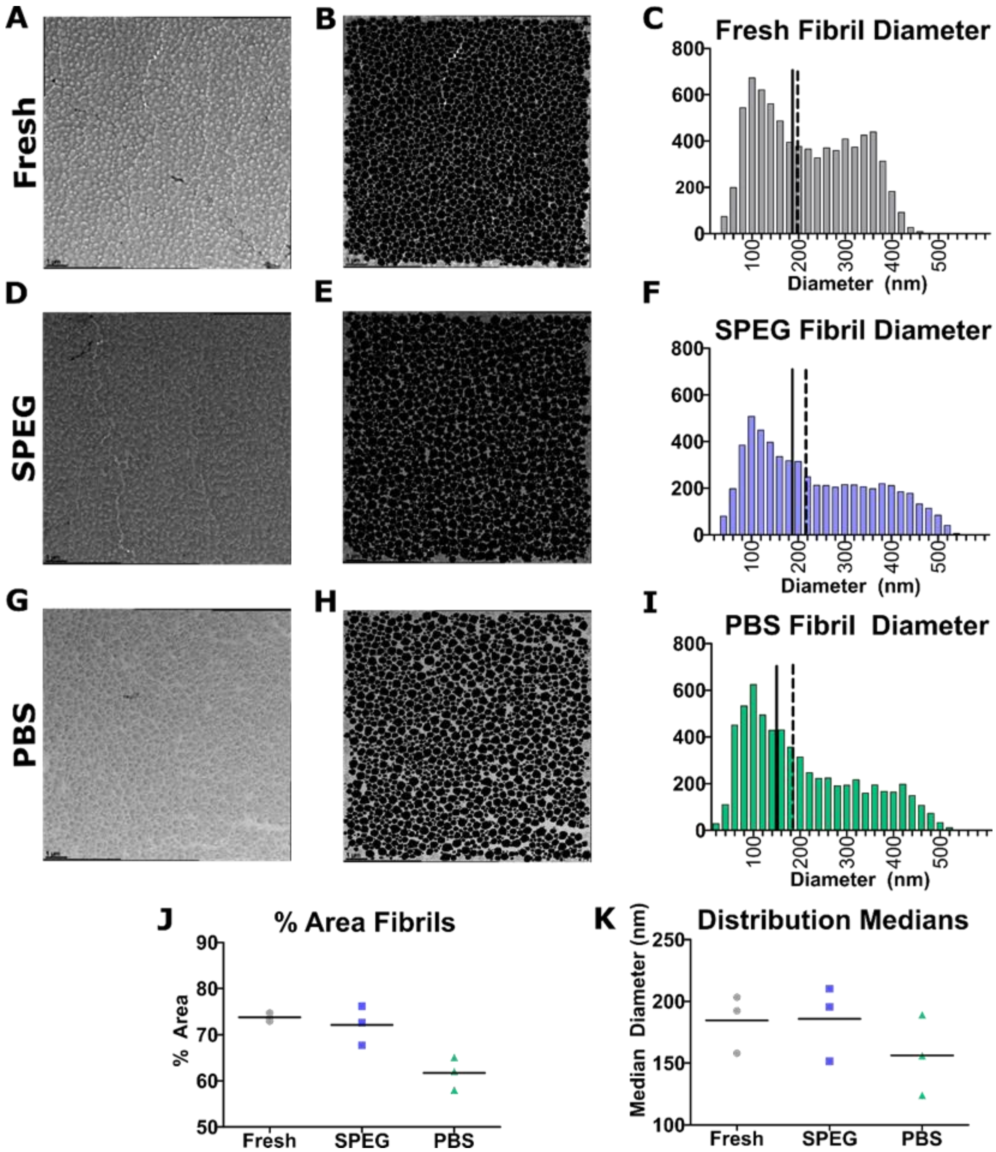

Figure 3.7: TEM structural changes with bath solution. Representative TEM images from A) Fresh (fixed immediately after dissection), B) SPEG, and C) PBS groups. D-F) Masks of representative images. Fibril diameter distribution for G) Fresh, H) SPEG, and I) PBS. The distributions were all significantly different from each other as determined by a one-way ANOVA ($p = 0.0009$). The solid line indicates the combined distribution mean, while the dashed line indicated the median. J) The % area of fibrils was not different between Fresh and SPEG, though Fresh and SPEG both had % area densities larger than PBS. (n=3) K) The fibril diameter distribution medians were not different between any groups. (n=3) * ($p < 0.05$).

3.4 Discussion

In this study, we have shown that a PBS bathing solution alters tendon multiscale mechanics and increases microscale damage compared to an SPEG bathing solution. At the tissue level, tendons in the PBS group had a lower modulus than SPEG samples for their baseline curves. PBS samples also showed an increased amount of non-recoverable sliding, which was an analog for microscale damage. In relation to load transfer between hierarchical levels, SPEG had a higher microscale to tissue strain ratio, which was close to 1. Thus, fibrils in SPEG experienced less strain attenuation between hierarchical levels than those in PBS.

The tissue-level mechanical behavior for PBS was consistent with previous findings [43,44,47,146], as was the baseline tissue-level behavior for the SPEG samples [44,146]. We showed that using PBS decreases the baseline modulus of tendon, which is consistent with prior findings [152]. We were particularly interested in any effects on transition and inflection point strains, as the stresses were all calculated with using the cross-sectional area measured at the reference length, thus, it is unclear whether bath solution influenced changes in the behavior of cross-sectional area during loading, apart from the already increased cross-sectional area as a result of swelling. Although the transition and inflection point strains were not different between groups at the baseline, the Δ value for transition strain was different. The Δ measurements, meant to evaluate the mechanical damage induced in the tissue as a result of mechanical loading, showed some differences between groups. Thus, PBS alters the tissue-level mechanical behavior beyond the previously observed decreases in modulus. Specifically, these changes for transition point strain suggest that bath solution may influence collagen fiber recruitment in the tissue.

At the microscale, SPEG samples illustrated a greater ability to recover microscale strain and sliding compared to PBS. PBS samples also showed a lower magnitude of microscale strain during mechanical loading compared to SPEG, further supporting our conclusion from the micro: tissue-scale strain ratio that PBS samples have reduced loading of the fibrils. As PBS increases the interfibrillar spacing of collagen fibrils, the ability of the tissue to bear load via interfibrillar shear could be restricted, leading to the observed reduction in load-bearing capacity, tissue level modulus, and microscale to tissue strain ratio [11,152,154].

Unexpectedly, SPEG samples had larger magnitude Δ values for modulus, transition point strain, and inflection point stress. The larger Δ, which corresponds to an increased amount of tissue-level damage, could be a result of the changes induced in the PBS samples from swelling prior to mechanical loading. That is, the Δ modulus for the SPEG group as a result of mechanical loading is larger in magnitude because the PBS modulus was already reduced as a result of swelling prior to mechanical loading. Whether or not this apparent decrease in material properties due to tissue swelling is reversible is a point for further investigation, though these effects have been seen to be reversible in other fibrous tissues [140].

The TEM images illustrate the structural changes as a result of bath solution on collagen fibril diameter and density. The % area density of fibrils was larger in both Fresh and SPEG groups than in PBS, showing that the tissue swelling decreases the collagen fibril density. This decrease in density reduces the amount of possible shear transfer by reducing contact between fibrils, altering the load sharing between collagen fibrils and influencing the observed changes in mechanical behavior and damage. Contrary to our expectation, the fibril diameter medians showed no difference between any groups, though the distributions were all different. It is possible that there is a difference which is lost due to the relatively low sample size for medians (n=3/group). Additionally, the high diameter distributions of Fresh and SPEG samples may be affected by their high densities. The high densities decrease resolution first by hindering the perfusion of staining medium and resin into the tissue; second, the high-density samples have fibrils in much more direct contact with each other. Both limitations make the defined boundaries between fibrils harder to define in the Fresh and SPEG samples, particularly for the boundaries of smaller fibrils. It is also possible that the large PEG molecules further restrict diffusion of the fixation solutions into the tendon, further hindering image quality. The resulting distributions may thus not be adequately reporting the amount of smaller diameter fibrils in the Fresh and SPEG samples. Though the resolution challenges made the definition of distinct boundaries difficult, the difference between fibril and matrix was still clear, and thus the % area density measurement was not affected to nearly the same extent by the resolution change. Overall, these TEM results show clear structural changes as a result of bath solution choice to tendon fascicles, with SPEG appearing to more like Fresh, which may help explain the altered mechanical behavior with PBS.

The use of various salts and differing hydration levels has been shown to alter the self-assembly of collagen fibrils, as well as mechanics of collagen's molecular triple helix [155,156]. It thus possible that the large, hydrophilic PEG molecules present in the SPEG buffer may alter the surface hydration of the collagen triple helix [155]. Also, the difference between the Tris and phosphate ions in the respective buffers could alter the intrafibrillar collagen mechanics [156]. However, this study was focused on the geometric changes induced by the buffers and the resulting effect on mechanics. A discussion of the chemical mechanisms within the collagen fibrils is beyond the scope of this study.

The mechanical effects of altered water content have been observed in other tissues [139,140]. Tendon's uniaxial fibers leave the tissue relatively unrestrained to swell in the lateral direction. Tissues which have a more complex fiber network, such as articular cartilage or cornea, may therefore experience less swelling. A study with annulus fibrosus showed swelling in PBS; however, the samples were excised and sectioned to release residual stress in the fibers and thus freed the tissue for lateral swelling [140]. While some of these previous studies were able to have a fresh-frozen control [137,140,146,152], our test duration and the small cross-section of rat tail tendon made this unfeasible. A recent study done in human iliotibial band investigated the effect of water content on tissue and microscale properties using atomic force microscopy and tensile testing. The results of this study similarly found that micro- and tissue level mechanics were altered with changes in water content [157]. The effect of choice of bath solution on swelling and mechanics in the rat tail tendon demonstrated here are likely to also occur in other fibrous tissues, as PBS equilibration effects the interfibrillar space of collagen in annulus fibrosus, meniscus, human tendon, and ligament [138–140,157]. However, the magnitude of these effects is likely to be tissue and species specific due to differences in composition, fiber density and alignment, and size.

With this study, we have shown that the osmotic pressure of bath solution changes the microscale loading and mechanical damage in tendon, in addition to altering microstructure and tissue-level mechanical behavior. The mechanical protocol completed in this study was about an hour in duration following at least an hour of bath equilibration, and involved only a single ramp, hold, and recovery period before the Diagnostic ramp. Longer duration tests or tests with repeated loading such as cyclic fatigue may be further affected by bath osmotic pressure. Rat tail tendon is a commonly used model for studying tendon mechanics and degeneration, and due to its small size and diameter may be especially susceptible to bath solution effects.

In conclusion, this study demonstrates the differences between a PBS and SPEG bath on tendon microstructure and mechanical behavior. The TEM imaging, in which tendon microstructure in SPEG appears like Fresh tendon, suggests that SPEG bath may better represent Fresh tissue mechanical behavior by reducing the swelling that occurs with PBS. Thus, SPEG may be a more appropriate choice for bathing solution for mechanical testing of tendon, especially for samples with a small cross section. Previous tests completed in PBS are still valid if appropriate control groups were used; however, true tissue properties measured from experiments with PBS baths should be used with careful consideration for modeling. Although previous studies have illustrated that PBS alters tendon modulus, hydration, and microstructure, our study shows that PBS also increases microscale damage in tendon and alters multiscale mechanics, compared to an SPEG bath that does not induce swelling. Future ex vivo mechanical testing should consider using SPEG as a bath solution with an osmotic pressure which preserves fresh tissue water content.

Chapter 4

TENDON COLLAGEN FIBRIL AUTO-SEGMENTATION WITH NUERAL NETWORKS AND THREE-DIMENSIONAL RECONSTRUCTION FROM SERIAL BLOCK FACE SCANNING ELECTRON MICROSCOPY IMAGES

4.1 Introduction

The main load-bearing component of tendon is its aligned collagen [1–3]. Tendon collagen has a hierarchical structure spanning length scale from nanometer (tropocollagen and molecule) to millimeter (fibril, fiber, and fascicle) [2,3,21,33,137]. The ultrastructure at these hierarchical levels directly impacts tendon mechanical function [16]. While tendon collagen has a low turnover rate [61], fibril structure is altered with tendon loading and is associated with changes in mechanical properties [36,100,119,158]. Therefore, it is important to measure the three-dimensional tendon ultrastructure across the hierarchical length scales, including at the nanometer scales.

Several imaging techniques has been used to visualize collagen structure at its smaller length scales, included x-ray crystallography, x-ray diffraction, electron microscopy, and second harmonic generation confocal microscopy [10,21,25,36,159,160]. Electron microscopy provides excellent high-resolution images of collagen fibrils to quantify two-dimensional (2D) parameters of fibril diameter, shape, and density [10,16]. However, traditional electron microscopy only provides an image in a single plane and cannot provide the three-dimensional (3D) structure that informs mechanical function. Serial Block Face Scanning Electron Microscopy (SBF-SEM) is a newer technique that uses automatic sequential microtoming between image captures to collect a series of images which span a sample volume, in an advance of earlier manual serial sectioning techniques [161,162]. These large datasets can by analyzed to reconstruct the 3D fibril structure and from this structure quantify parameters such as tortuosity, fibril alignment and fibril chirality [163]. The 3D fibril structure has important implications for load bearing via mechanisms such as fibril shear [16,33]. SBF-SEM has recently been used to evaluate structural changes which occur during development and to characterize the collagen fibrils within mature tendons [9,16,17,41,162–166].

Two considerable challenges are presented by the large image stacks from SBF-SEM: 1) the burden of segmenting thousands of fibrils, and 2) the difficulty of creating 3D reconstructions from segmented fibril cross-sections. When fibril density is low, contrast agents can easily diffuse into the sample, providing images with high contrast for which routine image processing can identify and segment collagen fibril cross-sections [41,162,167]. The rat tail is an example of a high contrast and low-density tendon (Fig 4.1A). Yet many tendons have high fibril density, making it difficult for contrast agents to diffuse into the sample and where fibril boundaries are less identifiable, making manual tracing necessary [9,16]. The rat plantaris is an example of a high-density tendon (Fig 4.2A, Fig 4.3A). Moreover, manual segmentation is not practical for large SBF-SEM datasets extending over many slices. For example, a typical dataset within a 20 x 13 μm field of view may have ~2,000 fibrils, and a 150-slice stack would contain ~300,000 total cross-sections for segmentation. To manually segment this large dataset in a single image stack would require ~1,750 hours. Thus, recent advances in machine learning using computer vision, such as u-net, a deep convolutional neural network (dCNN) developed for biomedical imaging, could be an alternative approach to traditional threshold-based image processing and manual segmentation. [168]

Following fibril segmentation, the second challenge is reconstruction into 3D collagen fibrils for evaluation of the fibrillar ultrastructure such as fibril length, tortuosity, angle to fascicle axis, merging and branching. Previous 3D reconstructions have been created from relatively low-density segmentations (either skeletally immature or prenatal tissue), or from manual segmentations of only a fraction of fibrils [16,162,166]. Reconstructing segmentations of highly dense tissue involves large numbers of fibrils that are often in contact with each other, necessitating robust workflows that consider the 3D structure to correctly recreate the fibrils. The challenge of 3D reconstruction is also likely to be more difficult for disorganized tendon, such as with degeneration or following injury and remodeling.1`

The objective of this work was to establish a u-net machine learning algorithm to automatically segment collagen fibril cross-sections from tendon SBF-SEM data sets and create 3D reconstructions of fibril ultrastructure for tendons that have low fibril density (rat tail tendon), high fibril density (rat plantaris tendon), and a high fibril density hypothesized to have disorganized 3D fibril ultrastructure (degenerated rat plantaris tendon due to 8-weeks of overload, Chapter 5). A secondary objective of this work is to compare the fibril geometries between the groups, to evaluate possible differences between positional (tail), and load bearing (plantaris) tendons.

4.2 Methods

4.2.1 Sample Preparation

A rat tail tendon, healthy plantaris tendon, and degenerated plantaris tendon were obtained and processed for SBF-SEM. The tail tendon from a 3-month-old male Sprague-Dawley rat was equilibrated in phosphate buffered saline, processed, and imaged in a previously published study [16]. The healthy plantaris tendons were female Long-Evans retired breeders. The healthy plantaris tendon was removed after euthanasia and immediately processed for SBF-SEM. The degenerated plantaris tendon was obtain from a model of synergist ablation in which the Achilles is excised, which overloads the plantaris tendon, resulting in degenerative changes at 8 weeks including increased area, increased cell density, fiber disorganization, and decreased material properties (Chapter 5).

Each tendon was sectioned into a 1mm x 1mm block and fixed in a 2% paraformaldehyde, 2% glutaraldehyde, 2mM calcium chloride in 0.1M sodium cacodylate buffer for a minimum of 5 days [169]. Next, each block was stained according to an established protocol that included steps with osmium tetroxide, potassium ferrocyanide, thiocarbohydrazide, 1% uranyl acetate, and *en bloc* lead aspartate [169]. Each block was then dehydrated with an ascending ethanol series. Finally, samples were infiltrated with Epon hard resin in an ascending series over 10 days and polymerizated in a 60°C oven for 48 hours [169].

4.2.2 Image Acquisition

The SBF image stacks were acquired using a ThermoFisher Scientific Apreo Volumescope SEM (Hillsboro, OR) in low vacuum mode at 50 Pa with accelerating voltage of 2.5 keV and at beam current of 0.1nA. The tail image stack had a 20.27 x

16.74 µm in-plane field of view with a 10 nm/pixel resolution; 432 slices were collected with 200 nm spacing, resulting in an image stack along an 86.20 µm total axial length and 2028 x 1675 image size. The plantaris tendon image stacks had a 20.49 x 13.66 µm in-plane field of view with a 6.67 nm/pixel resolution; 175 slices were collected with 200 nm spacing, resulting in an image stack along 35 µm in total axial length and 3072 x 2048.

4.2.3 Image Pre-processing

Image preprocessing and segmentation operations were performed with a Unix high performance computer (96 GB RAM, 4x Intel Xeon Gold 5118 CPUs @ 2.30GHz). SBF-SEM images were first processed in FIJI to remove noise by applying a Gaussian blur with sigma=1.25, followed by an anisotropic diffusion filter [170]. Each sample was segmented using two techniques: routine Otsu thresholding and u-net machine learning. For Otsu thresholding of the degenerated plantaris, a Gaussian blur with sigma=2 gave an Otsu segmentation with a better IOU value and was thus used instead of Gaussian sigma=1.25.

4.2.4 Otsu Thresholding Segmentation

Otsu thresholding was completed in FIJI after pre-processing. Otsu was selected as the threshold method in the FIJI thresholding function [171]. After thresholding, a watershed transform was applied followed by 2x erosion to separate joined collagen cross-sections.

4.2.5 U-net Machine Learning Segmentation

Manual segmentation was performed for u-net training and validation. Two training rounds were required. For the first training round, five image slices, randomly spaced along the image stack, were selected. A 1024 x 1024 region of interest (ROI) was chosen in each slice and this ROI was checked to confirm that it included representative background material such as voids and cells. Each ROI was then imported into Seg3D and the ROI was manually segmented to create fibril masks [172]. The segmented masks and corresponding ROIs were exported and used to train the u-net.

The u-net architecture was based on Ronneberger et. al [168]. The model was built in Python using the Keras machine learning library with TensorFlow backend and runs on a high-performance computer with an Nvidia v100 GPU. Our u-net architecture utilized four contracting and expansion blocks with 3x3 convolutional layers. A patch size of 64 was used for training, and the dataset was augmented by patch rotations (90, 180, 270 degrees), and horizontal and vertical flipping. Training consisted of 200 epochs, with a loss function based on the Tversky index.

After training the u-net on the first five ROIs, the output weights were used by the u-net to segment the entire image stack. The resulting segmentation of the entire image stack was inspected and an additional five slices with qualitatively poor segmentation results were selected. A second set of 1024 x 1024-pixel ROIs from these image slices were manually segmented for a second round of training. The u-net was then re-trained using all 10 manually segmented ROIs. Weights from the second training round were used by the u-net to segment the entire image stack. The u-net segmented dataset was imported into FIJI, and a watershed transform was applied followed by 2x erosion to separate joined collagen cross-sections.

4.2.6 Validation

To evaluate the success in the collagen segmentations, a random subset of the manual segmentation data (20%) was reserved, and the accuracy of the u-net and Otsu methods were calculated with the Intersection over Union method (Table 1).

4.2.7 2D Analysis

To compare to previous work, 2D analysis of the segmentation masks was performed. A 1024 x 1024 region with no cells or interruptions was selected. The estimated fibril diameter (calculated from area as assumed circle), fibril circularity (calculated as 4pi(area/perimeter^2)) and fibril area fraction were calculated using the Analyze Particles function in FIJI. These metrics were calculated for every single fibril cross section for each slice, resulting in each fibril being represented multiple times. The results are shown as normalized histograms comparing the parameters from both automatic segmentation techniques, Otsu thresholding and u-net, as well as from the limited manually segmented ROIs.

4.2.8 3D Reconstruction

A 3D model of the collagen network was created in Amira Software (ThermoFisher Scientific) for the Otsu threshold and the u-net machine learning segmentations. Joining segmented collagen cross-sections along the z-axis was accomplished by first applying a 3D Distance Map to the dataset, followed by a 3D Anisotropic Diffusion transform. Next, fibrils were filtered using interactive thresholding, before being labeled as individual objects. Finally, collagen fibrils that were cut off by the image borders were removed using the Selective Border Kill Python plugin, where all fibrils touching the outside edges (XZ and YZ, where Z is the long axis of the fibrils), were removed. Finally, fibrils were filtered by length such that only fibrils persisting in at least 50% of the axial length of the sample remained. The 3D network structures were inspected, and the number of persisting fibrils were evaluated.

4.3 Results

Representative ROIs of the automatic and manual segmentations are shown in Figures 1-3. From the raw images, the tail SEM images have the least density and best contrast, with well-defined boundaries between fibrils, while both plantaris samples are much denser, and with less clear boundaries. Overall, the u-net results across samples appear to match the rounded shape of the fibrils than the Otsu results, which have more straight lines and sharp corners. The automatic segmentations also seem to result in smaller cross-sections than the manual tracing, which is likely from the erosion step in the analysis. While u-net and Otsu segmentations appear extremely similar for the more ideal tail images, the difference in shape is more pronounced for both plantaris samples.

Table 4.1 – IOU Values for Segmentations

Sample	Otsu IOU	U-net IOU
Tail	0.821	0.816
Healthy Plantaris	0.783	0.652
Degenerated Plantaris	0.599	0.605

To assess the accuracy of the segmentation, Intersection over Union calculations were performed, where a value of 1 indicated perfect agreement. Overall, the segmentation accuracies were similar between Otsu thresholding and u-net machine learning and accuracies decreased as the tendon structural complexity increased (Table 1) For tail tendon, the Otsu IOU was 0.821 and the u-net was 0.816 (Fig 4.1). For healthy plantaris tendon, Otsu IOU was 0.783 and u-net was 0.652 (Fig 4.2). For degenerated plantaris tendon, Otsu IOU calculation was 0.599 and u-net was 0.605 (Fig 4.3).

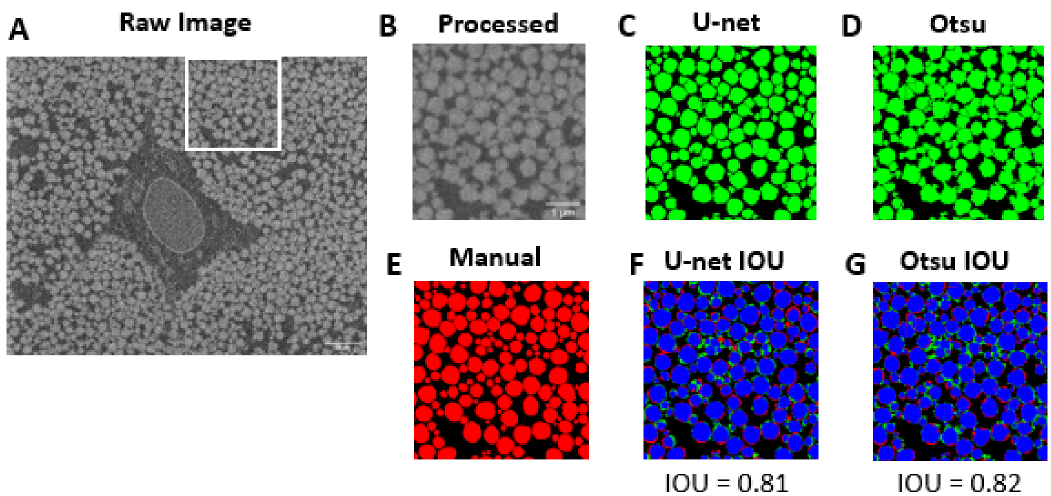

Figure 4.1: Tail segmentation results. A) Full raw tail SBF-SEM slice, showing a B) 1024 x 1024-pixel ROI following preprocessing. The segmentation results from C) u-net, D) Otsu thresholding and from E) manual segmentation. The Intersection over Union figures are shown for F) u-net v. manual, G) Otsu v. manual with manual segmentation in red, automatic segmentation in green, and intersection in blue.

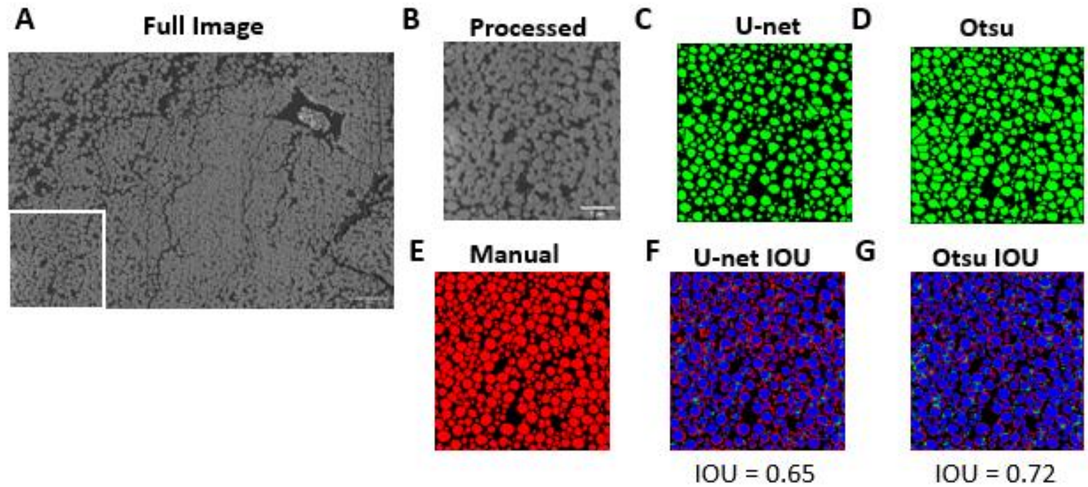

Figure 4.2: Healthy plantaris segmentation results. A) Full raw plantaris SBF-SEM slice, showing a B) 1024 x 1024-pixel ROI following preprocessing. The segmentation results from C) u-net, D) Otsu thresholding, and E) manual segmentation. The Intersection over Union figures are shown for F) u-net v. manual and G) Otsu v. manual segmentation, with manual segmentation in red, automatic segmentation in green, and intersection in blue.

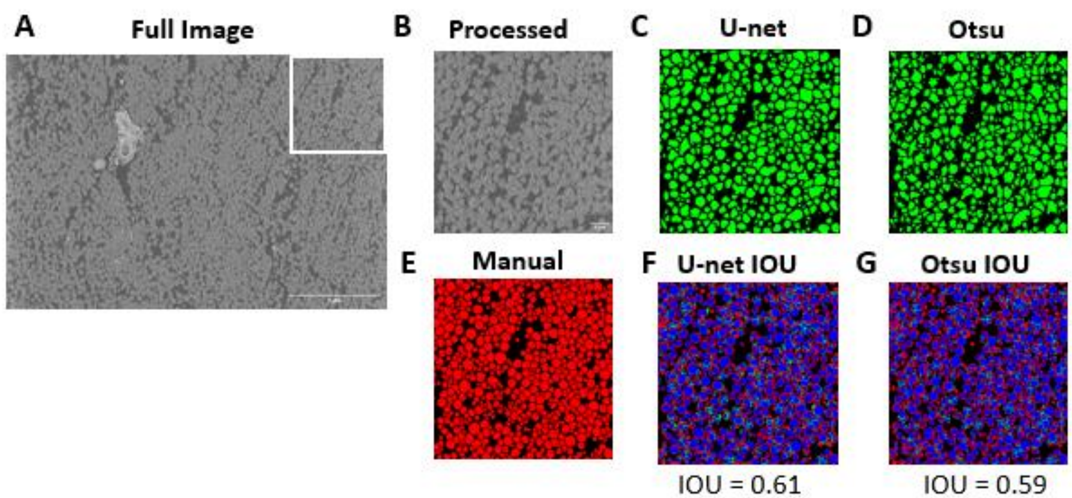

Figure 4.3: Degenerated plantaris results. A) Full raw plantaris SBF-SEM slice, showing a B) 1024 x 1024-pixel ROI following preprocessing. The segmentation results from C) u-net, D) Otsu thresholding, and E) manual segmentation. The Intersection over Union figures are shown for G) u-net v. manual and G) Otsu v. manual segmentation, with manual segmentation in red, automatic segmentation in green, and intersection in blue.

The 2D segmentations were analyzed to compare the Otsu and u-net results to manual segmentation (Table 2). For tail, mean Otsu and u-net diameters were 0.26 µm, compared to 0.35 for manual segmentation. For healthy plantaris, mean Otsu diameter was 0.19 µm and u-net was 0.18 µm, compared to 0.23 µm for manual segmentation. For degenerated plantaris, mean Otsu diameter was 0.20 µm and u-net was 0.17 µm, compared to 0.19 µm for manual segmentation. Overall, u-net and Otsu results were startlingly similar when evaluating fibril diameter. However, the mean fibril circularity was lower from Otsu results compared to u-net. For tail, mean Otsu circularity was 0.72 and u-net was 0.82, compared to 0.81 for manual; for unloaded plantaris mean Otsu circularity was 0.75 and u-net was 0.81 compared to 0.80 for manual; and for overloaded plantaris mean Otsu circularity was 0.73 and u-net was 0.76 compared to 0.82 for manual (Fig 4.4D-F).

Table 4.2 – 2D Geometry Comparison Between Segmentations

	Diameter (µm)			Circularity		
Sample	Otsu	U-net	Manual	Otsu	U-net	Manual
Tail	0.26	0.26	0.35	0.72	0.82	0.81
Healthy Plantaris	0.19	0.18	0.23	0.75	0.81	0.80
Degenerated Plantaris	0.20	0.17	0.19	0.73	0.76	0.82

To compare the segmentation results between samples, 2D analysis was completed on the image stacks. The tail sample had a lower collagen area fraction, with a mean value of 38%, while the unloaded plantaris sample had a mean value of 46%, and overloaded plantaris samples a mean value of 47% (Fig 4.5A). Fibril diameter and fibril circularity were also compared between samples. Tail fibril diameter was slightly larger than both plantaris tendons, with tail having a mean diameter of 0.26 μm, 31% larger than the plantaris mean fibril diameter of 0.18 μm, and 35% larger than 0.17 μm for overloaded plantaris (Fig 4.5B). The degenerated plantaris fibrils were slightly less round than those from tail and healthy plantaris, with the tail sample having a mean fibril circularity of 0.82, unloaded plantaris sample a mean circularity of 0.81, and overloaded plantaris a mean circularity of 0.76 (Fig 4.5C).

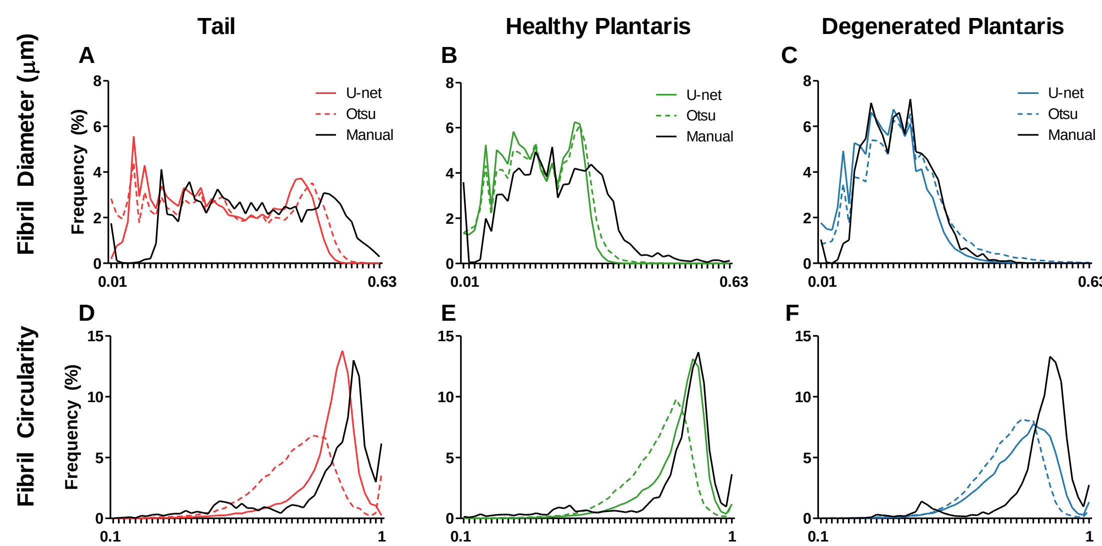

Figure 4.4: 2D segmentation analysis. A-C) Histogram of fibril diameter and D-F) fibril circularity for tail, healthy plantaris, and degenerated plantaris for u-net (color solid line), and Otsu (color dashed line), and manual (black solid line) segmentations. While u-net and Otsu perform similarly compared to manual segmentation for diameter, u-net much more accurately matched circularity from manual segmentation in comparison to Otsu.

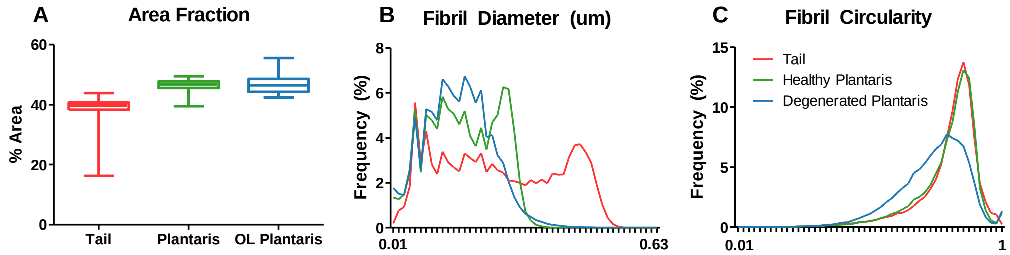

Figure 4.5: 2D fibril geometry analysis. A) The collagen area fraction from each slice in tail, healthy plantaris, and degenerated plantaris plotted with means and error bars showing maximum and minimum values. Histograms of individual fibril B) diameter and C) circularity for all segmented cross-sections in the image stack from tail, healthy plantaris, and degenerated plantaris. Overall, plantaris fibrils were denser and smaller compared to tail fibrils, while degenerated plantaris was less round than both healthy plantaris and tail.

To compare the reconstruction results between Otsu thresholding and u-net segmentation, the number of fibrils remaining after filtering from reconstructions using both segmentations were assessed (Fig 4.6E-F). Tail reconstruction resulted in 749 fibrils with u-net and 739 with Otsu; unloaded plantaris in 1424 fibrils with u-net and 1410 with Otsu; and overloaded plantaris in 3019 fibrils with u-net and 189 with Otsu.

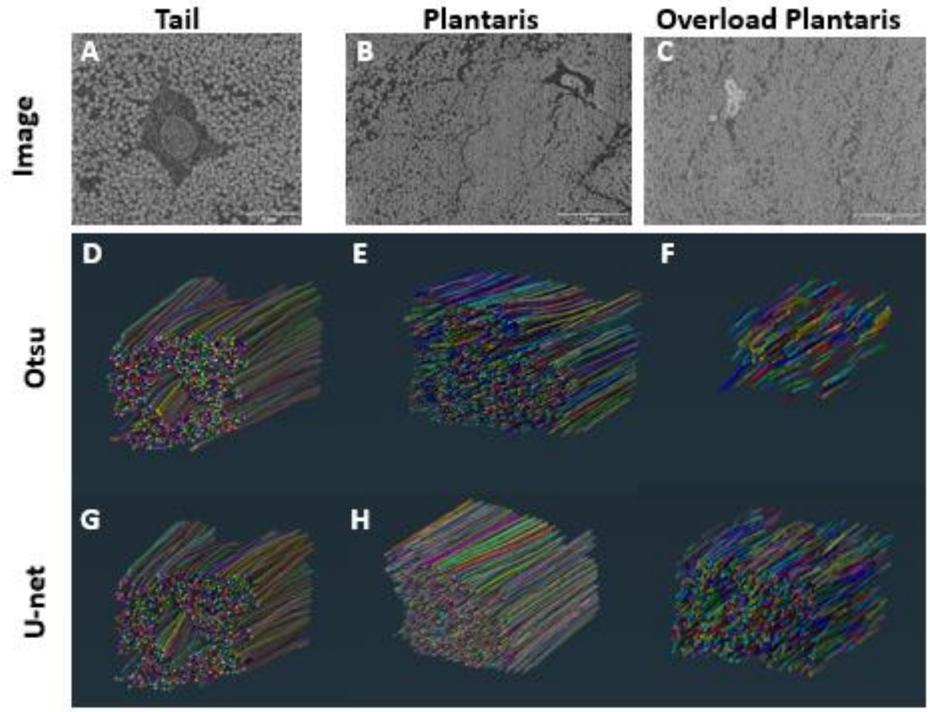

Figure 4.6: 3D fibril reconstruction and analysis. Raw image slice for A) tail, B) healthy plantaris, and C) degenerated plantaris tendon samples. D-F) show reconstructions from Otsu segmentation, while G-I) show reconstructions from u-net segmentation. While Otsu performs similarly to u-net while reconstructing the tail and healthy plantaris tendons, it is unable to reconstruct many fibrils from the denser, lower contrast degenerated plantaris sample.

4.4 Discussion

In this work, we applied a u-net machine learning algorithm to automatically segment collagen fibril cross-sections from tendon SBF-SEM data sets and created detailed 3D reconstructions of this data. We evaluated the success of the u-net results compared to manual segmentation and Otsu thresholding. Manual segmentation is the gold standard in the field for accuracy, but is not practical to evaluate large images, due to the extreme time demands. Otsu thresholding is fully automatic and thus very fast but struggles to accurately recapitulate fibril shape and handle high-density images. U-net was able to accurately segment three different tissues, and these segmentations were high enough quality to create fibril reconstructions including thousands of collagen fibrils. Using u-net segmentation, we were able to analyze three different tissue samples: one from tail tendon, one from healthy plantaris tendon, and one from a degenerated plantaris tendon. Rat tail tendon fascicles, a positional tendon, and rat plantaris tendon, an energy-storing tendon, were selected as traditional electron microscopy has shown differences in fibril diameters for functionally different tendons, with both bovine and equine load-bearing tendon having a lower fibril diameter than positional tendon [14,15]. Between the imaged samples, the tail had a lower collagen fibril density and larger mean fibril diameter compared to both plantaris tendon samples. The measured difference in fibril diameter for the load bearing plantaris tendon compared to tail also matched that to previous studies in traditional electron microscopy in equine and bovine forelimb tendons [14,15]. From the fibril circularity results, degenerated plantaris fibrils were slightly less round than those from tail and healthy plantaris.

Our successful implementation of a u-net algorithm for automatic segmentation of collagen fibril cross-sections allows for analysis of more dense, complicated tissues. Tendon is far from an idealized tissue for automatic segmentation – image contrast may be low as stain diffusion is hindered from high density, and the high fibril density is itself a challenge. Interestingly, while u-net resulted in a segmentation that was more accurate in describing manually traced fibril circularity, it slightly underperformed in IOU calculations and in matching fibril diameter compared to Otsu segmentation. It is possible that the unprocessed segmentation from u-net is more accurate than Otsu, and that the repeated erosion step is too aggressive for the u-net results but brings Otsu closer to the manual segmentation. Raymond-Hayling et al recently created another analysis pipeline to track collagen fibrils through SBF-SEM image stacks. This work used different techniques for both the segmentation and reconstruction phases, with some shared steps. Segmentation was completed by cropping images and applying a Gaussian filter to remove image noise, as completed in this work, before using adaptive thresholding followed by watershed analysis. Unlike u-net analysis, adaptive thresholding is based solely on local image contrast, and does not involve error minimization during segmentation. For samples with extremely high contrast and clear boundaries, thresholding – whether adaptive, Otsu, or another method – is likely sufficient for accurate segmentation. This holds especially true if only diameter or centroid information is desired, and not accurate description of fibril cross-sectional shape. The success of our segmentation with multiple tissues of varying image clarity shows that this method would be easily applied to any imaging with highly aligned collagen – including cornea, ligament, meniscus, intervertebral disk, and engineered tissues.

Beyond developing a method which improved segmentation accuracy, in this work 3D reconstructions of the fibrils were also created using Amira software. In comparison, Raymond-Hayling fibril tracking was achieved using an error minimization method of Euclidean distance of fiber centroids in adjacent slices, as well as fibril cross section shape. This is a fundamentally different approach from the 3D technique used in this work, which involved 3D image processing filters such as diffusion mapping and 3D anisotropic diffusion. Importantly, a reconstruction workflow that can handle many fibrils can give a robust evaluation of 3D geometric features of the collagen fibrils that have important implications in load transfer.

After reconstruction, work by Safa et. al. in manually segmented fibrils calculated tortuosity as a metric of the complexity of fibrillar structure, finding that smaller diameter fibrils were more likely to have a higher tortuosity, or more complex structure [16]. Raymond-Hayling also assessed the 3D geometry of the fibrils after reconstruction with fibril tortuosity, as well as alignment, and chirality. Increases in complexity suggest more opportunities for load dispersion by mechanisms such a fibril shear and conversion of tensile load to off-axis loading and contribute to the higher fatigue resistance of energy-storing tendons, and is valuable information that can be obtained from successful fibril reconstructions [41,173].

One limitation of the completed work is that the reconstruction workflow was optimized to evaluate the structure of fibrils which crossed the entire region of interest, and misses other interesting features, such as fibril ends [9]. Further, cells and cellular components were not segmented from the image stacks. The interaction of tenocytes and collagen fibrils can inform the understanding of mechanotransduction within tendon and is of great interest to the field.

In summary, this study used a u-net algorithm to automatically segment collagen fibril cross-sections and created a 3D reconstruction of those fibrils for three different tendon samples. Our u-net segmentation outperformed a more standard Otsu thresholding technique when describing fibril shape, and in reconstructing fibrils for the most challenging sample. We also observed that tail, a positional tendon, had a lower collagen fibril density and larger mean fibril diameter compared to both plantaris tendon samples, a load-bearing tendon. This method’s successful application to multiple different tendon samples shows promise to can be applied in a variety of conditions to better understand how differences in collagen fibril structure lead to functional changes. Additionally, degenerated plantaris fibrils were slightly less round than those from tail and healthy plantaris. Overall, between the workflow developed in this work and others in the field, there are a range of approaches available to the field depending on the relatively complexity of collected image stacks.

Chapter 5

OVERLOAD IN A RAT IN VIVO MODEL OF SYNERGIST ABLATION INDUCES TENDON MULTI-SCALE STRUCTURAL AND FUNCTIONAL DEGENERATION

5.1 1. Introduction

Tendon degeneration and mechanical damage are widely referred to as an overuse injury, with little distinction in the clinical or research communities between the magnitude of load (overload) or the number of cycles (overuse) as the injury mechanism. Clinically, there are two primary tendon disorders, overuse tendinopathy and acute tendon rupture, and these are associated with different loading environments. Overuse tendinopathy is a painful disorder that most commonly occurs in individuals who perform a high number of repeated motions at relatively normal load magnitudes such as athletes and manual laborers [174–176]. In contrast, tendon rupture most commonly occurs in an apparently asymptomatic (pain-free) tendon and is associated with rapid increases in force magnitude or direction during activity [177–180]. Importantly, both tendinopathy and tendon rupture occur in degenerating tendons, as indicted by evaluation of the tendon after acute rupture [180–182]. Because the clinical presentation between tendinopathy and tendon rupture are quite different, it is likely that different mechanisms and pathways lead to the end-stage degenerative state. However, animal models of tendon degeneration are mostly focused on overuse [102,114,183]. As a result, there is a need to understand how overload, in the absence of overuse, leads to tendon degeneration.

Prior animal models of overuse induce damage primarily via increasing the number of loading cycles (e.g., using treadmill running). Additionally, previous animal models have used an increased number of loading cycles to induce degeneration combined with a moderately increased magnitude of load via inclined treadmill running [98,184]. Notably, some overuse animal models do not develop degenerative tendon changes; and therefore, may be more accurately considered exercise models, where tendons adapt to the increased loading demands with increasing cross-sectional area (CSA) and stiffness but without degenerative changes, like humans [70,185]. Degenerative structural tendon changes in animal models include atypical collagen fibril size, organization, type, and content; increased proteoglycan content; and increased cell density as well as cell and nuclear morphology changes [17,86,98,184,186–192]. Degenerative tendons also experience functional deficits, such as decreases in tendon stiffness or modulus, and ultimate stress [98,102,103,184,193–195].

In contrast to overuse models, synergistic ablation (SynAb) is an animal model originally used to study muscular hypertrophy in which the tendon-muscle unit of interest is overloaded by surgically ablating its synergist [127,129,196,197]. To overload the plantaris tendon in rodent hindlimbs, the Achilles tendon has been surgically ablated [129,132–134]. Short term remodeling of the plantaris up to four weeks following SynAb has demonstrated increases in CSA, proteoglycan content, collagen expression, and regional increases in cell density [132–135]. Similarly, a recent study used a comparable procedure in the murine shoulder where the infraspinatus tendon was ablated and the synergist tendon (supraspinatus) exhibited increased CSA, decreased proteoglycan content, and decreases in stiffness, maximum force, and ultimate stress after 4 weeks [193]. It remains unknown, however, whether tendon overload will lead to chronic tendon degeneration, as previous studies of isolated overload cover a relatively short time duration [133–135,193]. Clinical and pre-clinical model definitions for "chronic" tendon disorders vary, with clinical chronic tendinopathy spanning 3 months to 30 years, while previous pre-clinical animal studies have considered timepoints from 6-8 weeks as the beginning of chronic changes [57,113,198–202]. Therefore, the objective of this study was to investigate whether overload of the plantaris tendon leads to chronic degeneration by investigating the multiscale structure and function up to 8-weeks following SynAb of the Achilles tendon. We hypothesized that tendon overload via SynAb will result in degenerative changes, such as an increase in tendon CSA, increased cell density, decreased collagen alignment, increase in collagen fibril diameter, and decrease in tissue modulus.

5.2 2. Methods

5.2.1 Surgical Procedure

All experiments were approved by the University of Delaware Institutional Animal Care and Use Committee. Seven-month-old Long-Evans female virgin rats were obtained (Charles River Laboratory, Table 2). These rats were randomly assigned to one of three groups: surgical synergistic ablation of the Achilles tendon (SynAb), sham surgery (Sham), or intact nonsurgical control (Intact). To increase loading of the plantaris tendon in the SynAb group, bilateral Achilles tenectomy was performed under 2-3% isoflurane anesthesia. First, a subcutaneous injection of bupivacaine (0.1 mg/kg) was administered at the site of incision to reduce sensation during the procedure, while a subcutaneous buprenorphine injection (0.05 mg/kg) was given to alleviate pain at the end of the procedure. Incision sites were closed with vicryl 3-0 sutures or skin glue (VetBond, 3M, Maplewood, MN). Silver sulfadiazine was applied topically to the incision site to mitigate infection risk for incisions closed with sutures. Following surgery, animals were allowed to ambulate at will with access to water, solid food, and a heat source for at least 4 hours before returning to their normal cages. The sham group followed the same bilateral surgical protocol described for SynAb without resection of the Achilles tendon. The intact group included age-matched animals which received no surgical intervention. Animals were evaluated for activity and tendon geometry for up to 8 weeks, as described below. After 8 weeks, animals were euthanized, and the left and right tendons were block randomized. One tendon was immediately prepared for histology and scanning electron microscopy (SBFSEM), while the other limb was left intact and frozen for multi-scale biomechanical testing and second harmonic generational (SHG) imaging, as described below.

Table 5.1 – Distribution of Study Animals:

Assay	# Animals	# Tendons
Activity Monitoring	6 (2/group)	N/A
MRI	18 (6/group)	36 (12/group)
Histology	H&E: 12 (4/group) PSR: 17 (5-6/group)	H&E: 12 (4/group) PSR: 17 (5-6/group)
SBF-SEM Imaging	3 (1/group)	3 (1/group)
Mechanical Testing	17 (5-6/group)	17 (5-6/group)
SHG Imaging	18 (6/group)	18 (6/group)

5.2.2 Activity Monitoring

Activity monitoring was performed to evaluate animal activity post-surgery. Rats (n=2/group) were housed individually on the evening of monitoring (~5PM) into a standard clear cage with a frame containing an infrared activity monitoring system placed on the outside of the cage (ActiTrack, PanLab, Barcelona, Spain). Distance traveled and number of hindlimb rearings were monitored throughout the night, and the recorded data was analyzed for an 8-hour dark cycle, in 10-min bins and summed. Recordings were made pre-operatively for 3 consecutive nights for an average baseline activity and for one monitoring cycle 3 days, 2-, 4-, and 8-weeks post-surgery.

5.2.3 Longitudinal High-Resolution MRI

To evaluate changes in cross-sectional area and shape of the plantaris tendon, rats were anesthetized using 2-3% inhaled isoflurane and limbs were imaged using high-resolution magnetic resonance (MR) images (Bruker Biospec 94/20, Billerica, MA). MR images were acquired 2-3 days before surgery as a baseline measurement and at 4- and 8-weeks post-surgery (n=4 rats/group, Table 2). The intact controls were imaged only at baseline and 8 weeks. For MR image acquisition, a 2 cm surface coil with global shimming was used to acquire multi-slice axial images using a 3D T1 FISP sequence (TR/TE = 584/2.9 ms, Field of View = 16 x 31 x 86 mm, matrix = 165 x 224 x 43, spatial resolution = 100 x 140 x 200 μm, excitations = 4, flip angle = 10.0° and acquisition time = 6 min). The plantaris tendon and granulation tissue (in the SynAb group) were manually segmented using ITK-SNAP software [203]. After segmentation and realignment of the tendon neutral axis in ITK-Snap, the tendon CSA and eccentricity and the granulation tissue CSA were calculated using MATLAB

[203]. As the aspect ratio of the tendon changes rapidly close to the enthesis, we compared the median plantaris CSA and eccentricity at each time point for all segmented slices in a sample. This was to reduce the bias from the distance of a slice to the enthesis, as there was some variation between samples in number of slices with free tendon visible. Therefore, no comparisons were made along the length of the tendon because of the relatively large slice thickness and difficulty indexing location between slices.

5.2.4 Histology

Immediately post-euthanasia, one plantaris tendon from each animal was dissected for use in structural assays, with half the tendon prepared for SBF-SEM, and the other going to histology. The plantaris tendon was dissected and then one-half fixed with 4% paraformaldehyde in Sorenson's buffer for at least 48 hours before paraffin embedding, with the other half prepared for electron microscopy. Tendons were processed for paraffin histology. Paraffin processed tendons were transversely bisected at the midline, with one half randomly assigned to longitudinal sectioning. Longitudinal slices were stained using either Hematoxylin & Eosin (H&E) for cell density and morphology or Picrosirius Red (PSR) for collagen organization. H&E-stained sections were imaged using a brightfield microscope (EVOS M5000, Invitrogen, Waltham, MA). Sections stained with PSR were imaged using circular polarized light microscopy.

Sections stained with H&E were used to quantify the cell density and the cell nuclear aspect ratio (NAR). A custom ImageJ (FIJI) macro was used to segment the nuclei from the tendon [204]. Briefly, we performed color deconvolution (vectors=H&E) followed by Gaussian blur (sigma=2) and contrast enhancement

(0.35%, normalize) to segment nuclei based on their high intensity threshold. Segmented nuclei were masked, and the analyze particles function in ImageJ was used to quantify nuclei number and morphological parameters, specifically NAR. Cell density was calculated based on the nuclei number per mm^2.

PSR stained sections were scored by 3 blinded reviewers using a semi-quantitative scale from 1-5, with 5 being the best organization [5 = extremely organized and yellow, 4 = predominantly organized and orange, 3 = mixed organization and green, 2 = predominantly random and red/green, 1 = extremely random and red/black] as previously [205].

5.2.5 Serial Block Face Scanning Electron Microscopy (SBF-SEM)

5.2.5.1 Sample Preparation

Immediately post-euthanasia, one plantaris tendon from each animal was dissected for use in structural assays, with half the tendon prepared for SBF-SEM, and the other going to histology. Distal and proximal tendon bisections were block randomized between the two assays, with the medial portion of bisection used for imaging. The tendons were cut into 1mm x 1mm pieces before fixation in 2% paraformaldehyde, 2% glutaraldehyde with 2mM calcium chloride in 0.1M sodium cacodylate buffer for a minimum of 5 days. The samples were stained for SBF-SEM by adapting an established protocol that included steps with osmium tetroxide, potassium ferrocyanide, thiocarbohydrazide, 1% uranyl acetate, and en bloc lead aspartate, before dehydration with an ascending ethanol series. Finally, samples were infiltrated with Epon hard resin in an ascending series over 10 days before polymerization in a 60°C oven for 48 hours [169].

5.2.5.2 SBE-SEM Imaging

SBF-SEM image stacks were collected after confirming axial alignment of the samples (FEI Apreo VolumeScope SEM, ThermoFisher Scientific). The samples were sliced every 100 nm with images taken every other image for a total slice thickness of 200 nm and a pixel resolution of 6.6667 nm. Overall, the in-plane field of view was 20.48 μm x 13.65 μm.

5.2.5.3 U-Net Segmentation and Analysis

To segment the collagen fibril cross-sections, an adapted u-net algorithm was used [168]. Raw images were processed with Gaussian and anisotropic diffusions filters to reduce noise while preserving edges. For each sample algorithm training was completed, where 1/6 of 10 slices from a full stack were segmented by hand to use as ground truth. Training of the adapted u-net was completed on a GPU for 200 epochs. The trained u-net was then applied to the full image stack that included the training images and applied to other ROIs from the same sample. Following segmentation, a watershed and two erode functions were applied in ImageJ to separate fibrils for particle analysis to measure area fraction, estimated fibril diameter, and fibril circularity for all slices in the stack.

5.2.6 Multiscale Mechanics

5.2.6.1 Sample Preparation

On the day of mechanical testing, samples were thawed at room temperature before dissection. The plantaris tendons were removed at the calcaneal insertion and the musculotendinous junction, with some muscle and fibrocartilage preserved for gripping [206]. To ensure that tenocytes embedded in between collagen fiber bundles, and not superficial cells, were being imaged for microscale strain analysis, 150 μm of the tendon surface was removed using a freezing-stage microtome. The cross-sectional area was calculated using laser displacement in a custom device across the sample midportion after microtoming [206]. Samples were stained in 0.5 ug/ml Hoechst 33342 (2'-[4-ethoxyphenyl]-5-[4-methyl-1-piperazinyl]-2,5'-bi-1H-benzimidazole, ThermoFisher) for at least 15 min to stain the cell nuclei for fluorescence imaging [136]. Further, a fluorescence fiducial marker was made with CellMask Orange cell membrane stain (ThermoFisher) on the surface of the tendon to assist in locating the same ROI throughout the loading protocol. Two ink markers on the tendon surface at the midportion were used for digital image correlation for tissue strain calculation. All samples were kept at room temperature after thawing and throughout mechanical testing. To maintain tissue hydration, samples were kept in a bathing solution of 8% weight-by-volume PEG (polyethylene glycol, 20kDa) and 15 mM Tris-buffered saline [146,207]**.**

5.2.6.2 Mechanical Testing Protocol

The testing protocol (Fig 5.1A) was like that used in prior studies [44,47,207]. Each sample was tested using a custom uniaxial testing device mounted on an inverted confocal microscope (Zeiss 880 Airyscan, objective Plan-Apochromat 10x/0.45W), which allows for simultaneous imaging and mechanical loading. The sample was gripped and loaded to a reference length by applying a 5 mN (0.5 g) preload and preconditioned for 5 cycles between 0 and 5% strain. Each sample was then ramped to 25% strain, held for 10 minutes at constant 25% grip strain, and unloaded back to the reference length. The sample remained at the reference length for a 15-minute recovery period before undergoing a final ramp until failure. All loading and unloading rates were 0.1%/sec. We chose 25% strain to be within the linear region based on pilot tests and previous work in plantaris tendon [43].

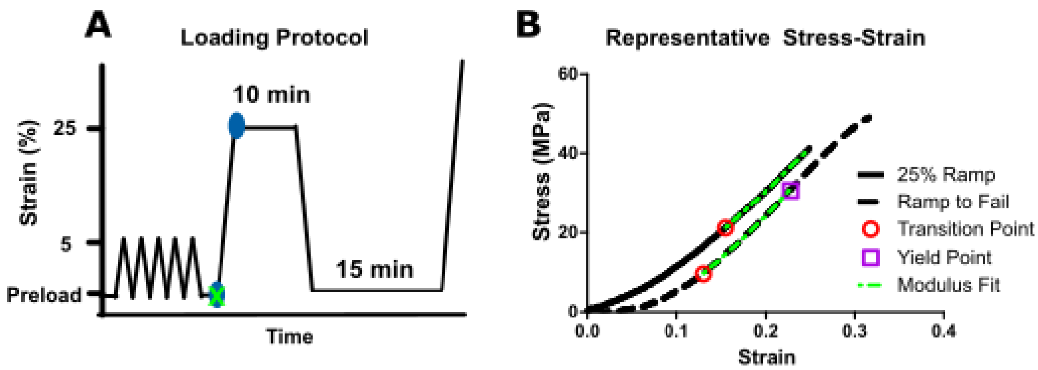

Figure 5.1: Mechanical loading protocol. Time points for confocal imaging shown with blue circles and SHG imaging with green X. B) A representative stress-strain curve from the Intact group, showing the 25% ramp as a solid line and ramp to failure as a dashed line. Transition point (red circle), modulus (dashed green line), and yield point (purple square) are indicated.

5.2.6.3 Imaging and Data Acquisition

To measure the tissue strain, we imaged the tendon with a CCD camera and tracked displacement of the ink markers on the midportion surface using digital image correlation. For microscale analysis, confocal image stacks were taken after preconditioning, and at the beginning of loading with a 10X water-immersion lens (425 x 425 µm). Following pre-conditioning, samples were also imaged with second harmonic generation (SHG) to assess collagen fiber alignment and damage [118].

5.2.6.4 Tissue-Level Data Analysis

The stress-strain ($\boldsymbol{\sigma} - \boldsymbol{\epsilon}$) curves were analyzed for transition point, yield point, and linear region modulus, with the transition point defined as the end of the toe region and yield point as the inflection point where the curve changes from strain-stiffening to strain-softening, as previously described (Fig 5.1B) [43,44,207]. Because some samples lost video tracking for digital image correlation, applied grip strain was used. The yield point was calculated by fitting a cubic smoothing spline with the *csaps* function in MATLAB and finding the first zero crossing point of the second derivative. The stress-strain curve between zero and the yield point was fit to a nonlinear exponential constitutive model which was optimized to obtain the transition strain (p), transition stress (q), and linear region modulus (E):

$$\boldsymbol{\sigma} = \begin{Bmatrix} \boldsymbol{A} * (\mathbf{exp}(\boldsymbol{B\epsilon}) - \mathbf{1}), & |\forall \boldsymbol{\varepsilon} \leq \boldsymbol{p} \\ \boldsymbol{E} * (\boldsymbol{\varepsilon} - \boldsymbol{p}) + \boldsymbol{q}, & |\forall \boldsymbol{\varepsilon} > \boldsymbol{p} \end{Bmatrix} \tag{5.1}$$

The optimization was performed on three of the parameters (p, A, B) and was completed using the MATLAB function *fmincon* to minimize the mean square error. Data analysis was performed for both the ramp to 25% strain and ramp to failure. The ramp to 25% strain did not reach a yield point, so the yield stress and strain, along with the failure stress and strain, were only determined for the ramp to failure, and 25% strain was used as a yield value for curve fitting the 25% ramps.

5.2.6.5 Microscale Data Analysis

Microscale deformations were determined from displacements of stained tenocyte nuclei in confocal images at reference and immediately following the 25% ramp (Fig 5.1A). Deformations were calculated using IMARIS (Oxford Instruments, Abingdon, UK). These displacements were used to calculate two-dimensional deformation gradient ($\boldsymbol{F}$) and Lagrangian strain using a custom MATLAB program [208]. Lagrangian strain was calculated as $\boldsymbol{E} = ½ (\boldsymbol{C} – \boldsymbol{I})$, where $\boldsymbol{I}$ is the identity matrix and $\boldsymbol{C}$ is the right Cauchy-Green deformation tensor ($\boldsymbol{C} = \boldsymbol{F}^{\boldsymbol{T}} \bullet \boldsymbol{F}$, where $\boldsymbol{F}$ is the deformation gradient). To calculate the Lagrangian strain across the field of view, all tracked cells were pooled (n=24-45 cells per sample). Maximum principal strains (e_1) were then calculated, using the relationship:

$$e_1 = \frac{E_{11}+E_{22}}{2} + \sqrt{\left(\frac{E_{11}+E_{22}}{2}\right)^2 + {E_{12}}^2} \tag{5.2}$$

To evaluate load transfer attenuation within the sample, the ratio of tissue to microscale strain at the end of ramp to 25% strain was calculated.

5.2.7 Collagen Organization and Damage Area Fraction from SHG Images

SHG images were taken at the same time and ROI as the reference stacks used for cell tracking (Fig 5.1A), having a 425 x 425 µm FOV and 0.29 µm in-plane pixel resolution (Zeiss 880 Airyscan, objective Plan-Apochromat 10x/0.45W). Quantification of collagen organization from images was automated using MATLAB based on Seresky et al. [118]. SHG images were divided into approximately 850 individual 41x 41-pixel blocks (0.01 x 0.01 mm) and a colormap was created to determine the variance of pixel intensities. Extreme intensities that were not associated with tissue were removed. A Fourier transform followed by a 3x3 Gaussian filter was applied to each block. A high pass filter was then used to remove all pixels except those with the top 20% of intensities to isolate collagen. Next, the image was binarized and ellipses were fit to the remaining pixels. The length of the major and minor axis and orientation of the major axis were collected for each ellipse and plotted against the original image. Fiber angle was calculated by subtracting the angle from the major axis to the x-axis from 90°. Strength of alignment was found for the fiber orientation of each ellipse by subtracting 1 from the ratio of the length of the major axis to the length of the minor axis. The fiber orientation of each block was then compared to the orientations of the adjacent blocks. If the difference between the orientation of the center block and the orientation of both adjacent blocks was greater than 5°, the window was labeled as damaged. Damage Area Fraction (DAF) was then calculated by normalizing the number of damaged blocks by the total number of blocks in the image (Fig 5.2).

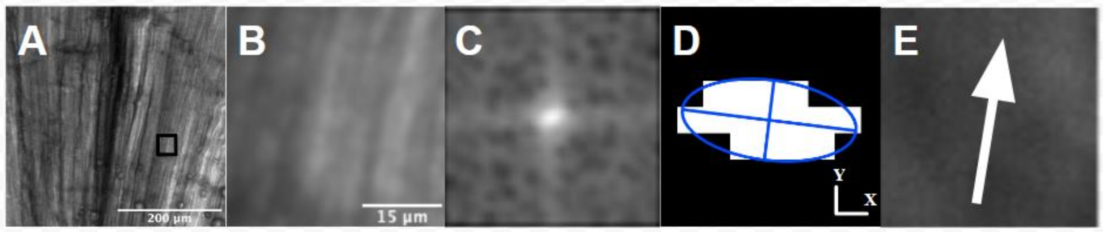

Figure 5.2: Representative damage area fraction method. DAF calculated from SHG images showing A) raw image, B) 41x41 pixel block, C) fast Fourier transform + Gaussian filter, D) best fit ellipse with major and minor axis superimposed, and E) overall fiber orientation of window.

5.2.8 Statistics

Variation in activity within each subject between timepoints was analyzed using a mixed effects model with only time as an effect. Plantaris CSA and eccentricity between groups were compared using a mixed effects model (effects: treatment, time, time x treatment, and between-subject effect) with standard least squares and restricted maximum likelihood estimation followed by Tukey post hoc tests for all pairwise comparisons. The difference in CSA of the granulation tissue between 4- and 8-weeks post-surgery was determined with a pairwise Student's t-test. Differences in cell density, average NAR, fiber orientation, and DAF at 8 weeks were determined with a non-parametric one-way ANOVA and Dunn's multiple comparison tests post-hoc. Differences in matrix organization from PSR at 8 weeks were determined with a Kruskal-Wallis's test. In all the above tests, significance was defined as $p<0.05$. Differences in modulus, transition strain, and transition stress were calculated with a repeated measures two-way ANOVA and multiple comparisons completed using Tukey's HSD tests. Differences in yield strain, yield stress, failure strain, and failure stress were calculated with One-way ANOVAs (as all measures passed normality assessed by Kolmogorov-Smirnov) and multiple comparisons completed with Dunn's multiple comparison tests.

5.3 Results

5.3.1 Activity Monitoring

There was no difference in total distance traveled and total number of rearings over time, specifically post-surgery (Fig 5.3). This indicates that any structural changes are due to overload and not altered number of loading cycles; animals did not alter their activity either due to surgery or developing degeneration. However, we recognize that our current sample size is limited, and activity levels are highly variable between rats and over time.

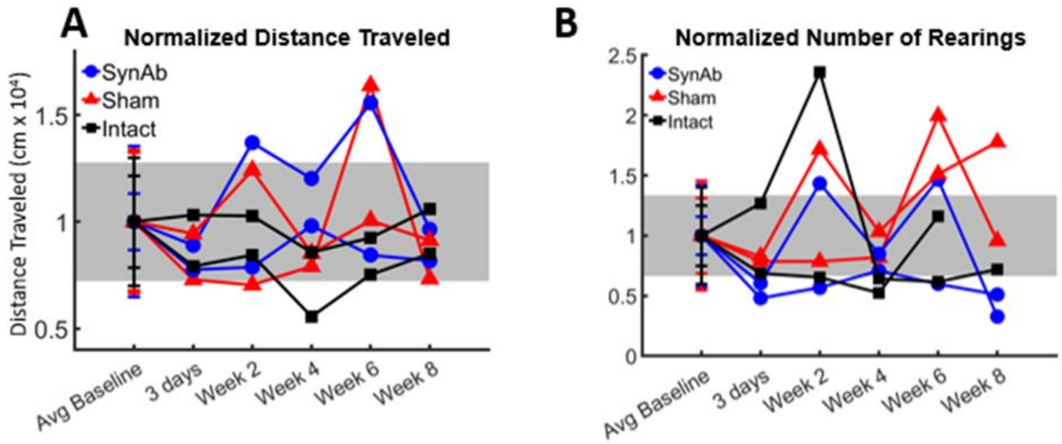

Figure 5.3: Activity monitoring results. Monitoring (n=2 rats/group) for 3 pre-surgical sessions to obtain an average baseline, and then at 3 days, 2-, 4-, 6-, and 8-weeks post-surgery. A) Normalized distance traveled for each animal and B) normalized number of rearings to own average baseline measures. The gray band shows the average baseline standard deviation for all animals.

5.3.2 Tendon Geometry from MRI

In vivo MRI was performed to evaluate the macro-scale changes over time (Fig 5.3, representative mid-tendon slice). The MRIs showed the plantaris tendon against the surrounding fat pad (at baseline and in Intact and Sham groups across time). The plantaris tendon macro-scale measures of CSA and eccentricity were calculated from segmented MR images (Fig 5.4A-B). There was no difference in the median CSA between any groups prior to surgery (0.18 mm2 +/- 0.03 mm2 (n=24), p=0.63). At 8 weeks, the SynAb median CSA was 14% larger than Sham (p=0.001) and 22% larger than Intact (p=0.002). Sham and Intact controls were not different at 8 weeks (p=1.0). Sham and Intact tendons were also not different at 8 weeks compared to their own baseline scans at 0 weeks (p=1.0, p=0.18). At 8 weeks, the SynAb CSA increased by 30% compared to its own 0-week CSA (p=0.06, Fig 5.5A). The median eccentricity was not different with treatment, however, the SynAb tendon had a lower eccentricity compared to its own baseline (p=0.03, Fig 5.5B). The CSA of the granulation tissue decreased from 4 to 8 weeks post-surgery in the SynAb group (p=0.03, Fig 5.6). To check for a potential increase in CSA due to overall animal growth, the correlation in animal weight to median CSA was found to have no effect (R^2=0.01, Fig 5.7).

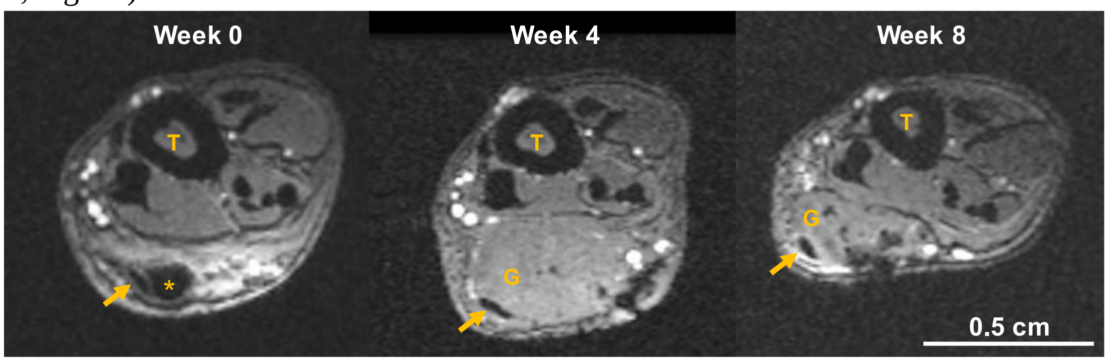

Figure 5.4: MRI of a representative SynAb sample. Before surgery (Week 0), and 4 & 8 weeks after surgery. Week 0 shows normal structures, including the Achilles tendon, while Week 4 and Week 8 show plantaris and formation (then resolution) of granulation tissue filling the Achilles void. Arrow indicates plantaris tendon, * Achilles tendon, G granulation tissue, and T tibia.

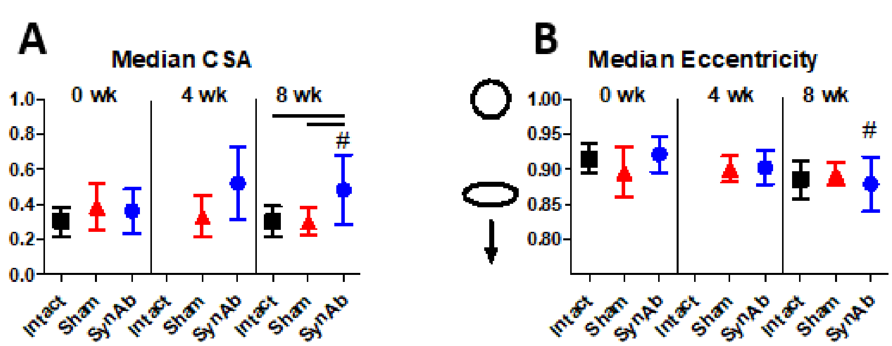

Figure 5.5: Geometry changes measured by MRI. A) Median CSA and B) median eccentricity with standard deviation between Intact, Sham, and SynAb groups at each time point. 8 weeks after surgery, the SynAb tendons were larger in cross-sectional area compared to Intact and Sham at 8 weeks, and SynAb at 0 weeks. 8 weeks after surgery, SynAb tendons were less round than SynAb at 0 weeks, but no differences were observed between groups. Line (between groups) and # (compared to baseline) show $p<0.05$.

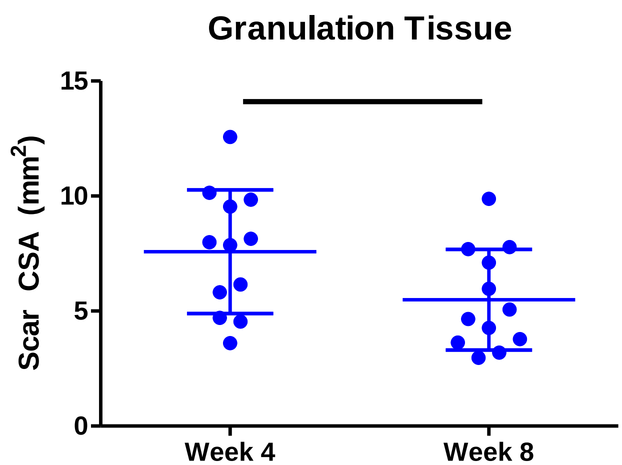

Figure 5.6: Longitudinal analysis of granulation tissue. Average CSA for granulation tissue after surgery for SynAb group. Line indicates $p<0.05$.

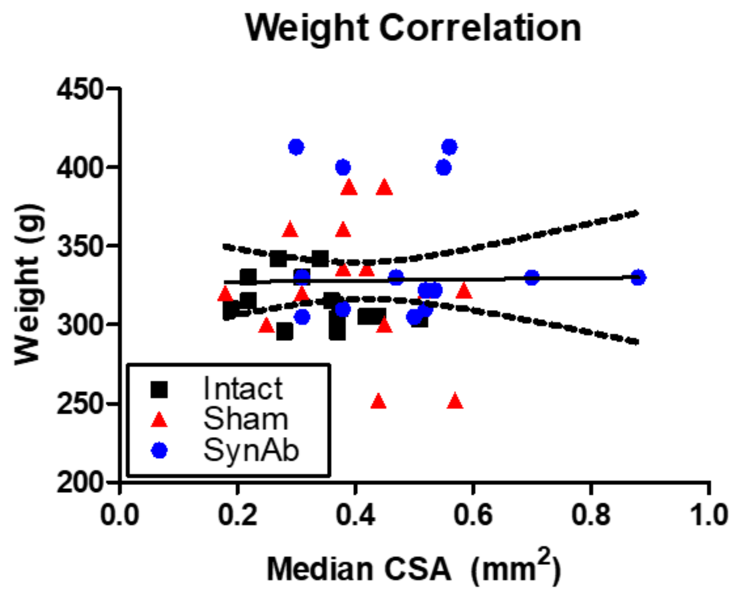

Figure 5.7: Correlation of rodent weight to median CSA. Pooled data correlation plotted with the 95% confidence interval. Table shows R^2 values from each correlation, as well as p-value testing for slope different from zero.

Histology

Histological staining with H&E was conducted to quantify cell density and nuclear aspect ratio (NAR) (Fig 5.8A) and staining with PSR was conducted to quantify collagen alignment in plantaris tendons (Fig 5.8B). At 8 weeks, SynAb cell density was 46% higher than Sham (p=0.03) and Intact (p=0.03, Fig 5.8C). Sham and Intact were not different from each other at 8 weeks (p=0.95) and there were no differences in NAR between any group at 8 weeks (p=0.6, Fig 5.8D). At 8 weeks, SynAb matrix organization was lower than Sham (p=0.04), but not Intact (p=0.18, Fig 5.8E), with Sham and Intact again showing no difference (p=0.67).

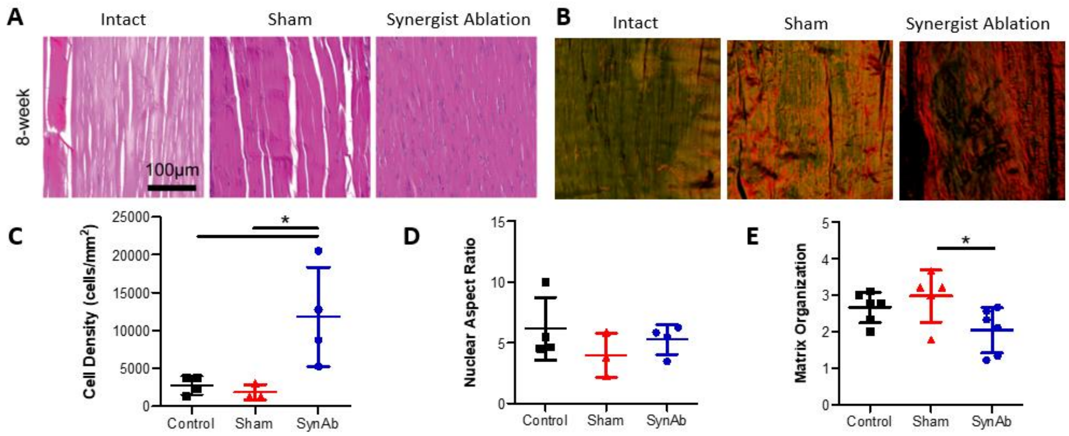

Figure 5.8: Histology results and analysis. A) Representative longitudinal H&E for each group (Intact, Sham, SynAb) at each time point B) Representative longitudinal PSR for each group (Intact, Sham, SynAb) at each time point. B) Cell density, and C) nuclear aspect ratio (NAR) for Intact, Sham, and SynAb at 8 weeks from H&E images. At 8 weeks, SynAb had a higher cell density than Intact and Sham, while no changes were seen in NAR between groups. E) Semi-quantified matrix organization for Intact, Sham, and SynAb at 8 weeks. At 8 weeks, SynAb was more disorganized than Sham, but not Intact. Lines with * show $p<0.05$.

5.3.3 Serial Block Face Scanning Electron Microscopy (SBF-SEM)

SBF-SEM imaging was conducted to investigate changes in collagen fibril structure following overload. SynAb had a larger area fraction of fibrils compared to Intact and Sham, with SynAb having a mean area fraction of 47%, compared to 39% for Intact and 40% for Sham (Fig 5.9). For the examined samples, SynAb also had a larger mean fibril diameter of 0.16 μm, compared to 0.12 μm for both Intact and Sham. There seemed to be no clear trend in circularity, with Intact having a mean circularity of 0.67, Sham of 0.75, and SynAb of 0.71.

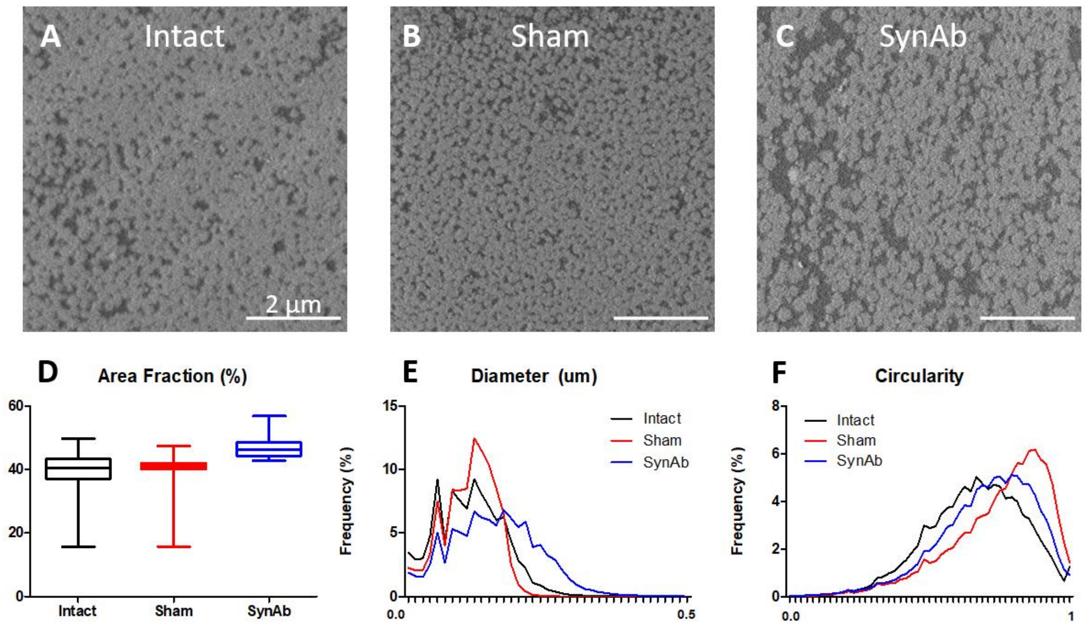

Figure 5.9: SBF-SEM images and analysis. Representative regions (6.8 x 6.8µm) from A) Intact, B) Sham, and C) SynAb SBF-SEM image stacks. D) Mean collagen fibril area fraction with standard deviation and histograms of E) collagen fibril diameter and F) fibril circularity for Intact, Sham, and SynAb tendons.

5.3.4 Multiscale Mechanics

Multiscale mechanics tests were performed to evaluate the functional changes between groups. Mechanical parameters were compared between groups, as well as between the first ramp to 25% and the second ramp to failure for modulus and transition point as a measure of treatment (Intact, Sham, or SynAb) and ramp type. During the initial 25% Ramp, SynAb had a trending decrease in modulus compared to Sham ($p=0.09$), but not compared to Intact ($p=0.21$, Fig 5.10A). During the ramp to failure, SynAb had a lower modulus than Sham ($p=0.04$), but not to Intact ($p=0.20$). There were no differences between groups for transition strain (Fig 5.10B). There was no difference between groups for transition stress ($p=0.15$, Fig 5.10C). As yield and failure parameters were only measured during the Ramp to Failure, the effect of treatment was assessed with a one-factor ANOVA. The SynAb yield stress was 60% lower than Sham ($p=0.02$), but not different from Intact ($p=0.49$), and Sham and Intact were not different from each other ($p=0.16$, Fig 5.10E). There were no differences between any groups for yield strain, failure strain, or failure stress ($p=0.29$, $p=0.50$, $p=0.16$, Fig 5.10D, F, G). Mechanical parameters calculated from tissue strains, rather than grip strains, had overall findings of treatment consistent with these results despite samples lost to tracking errors (Fig 5.11).

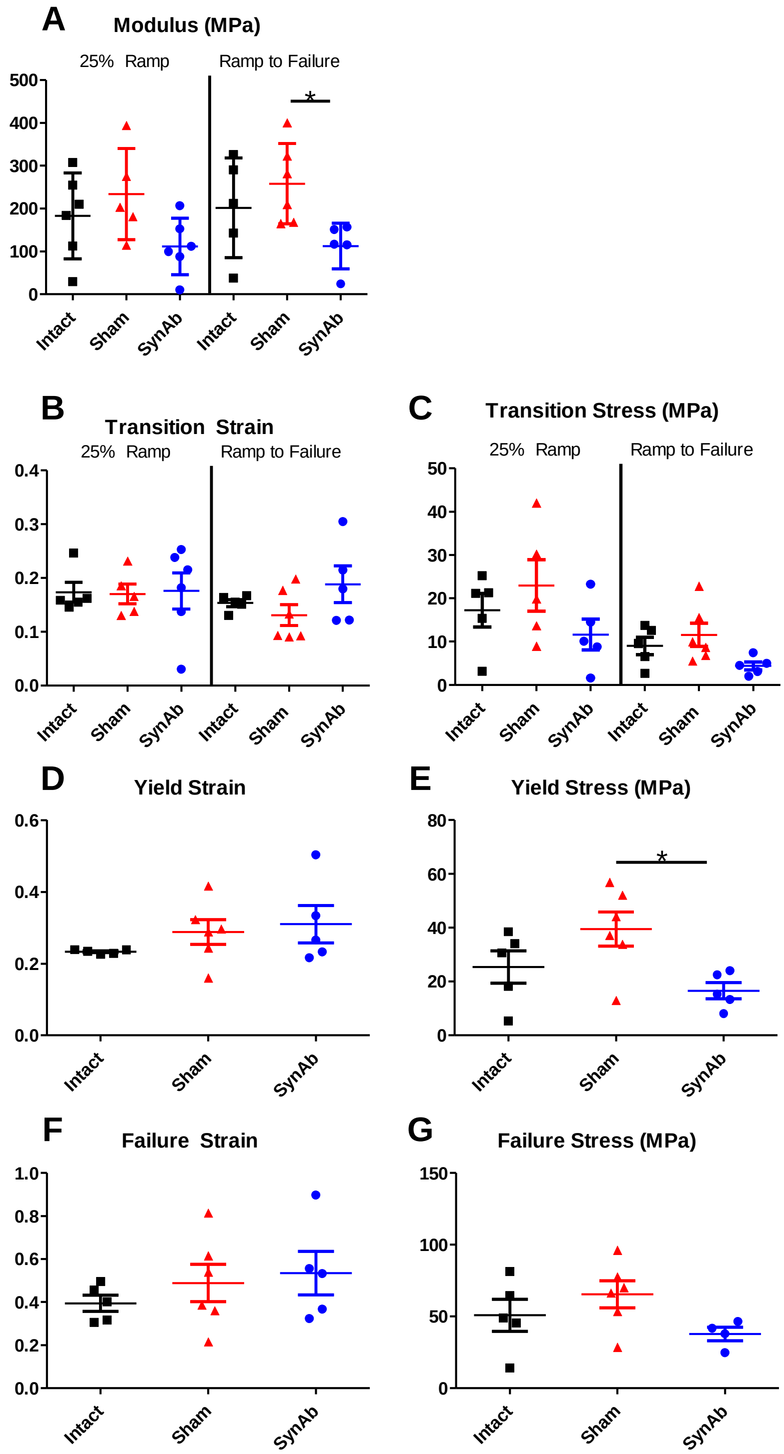
A
Modulus (MPa)
25% Ramp
Ramp to Failure
*
500
400
300
200
100
0
Intact
Sham
SynAb
Intact
Sham
SynAb
B
Transition Strain
25% Ramp
Ramp to Failure
0.4
0.3
0.2
0.1
0.0
Intact
Sham
SynAb
Intact
Sham
SynAb
C
Transition Stress (MPa)
25% Ramp
Ramp to Failure
50
40
30
20
10
0
Intact
Sham
SynAb
Intact
Sham
SynAb
D
Yield Strain
0.6
0.4
0.2
0.0
Intact
Sham
SynAb
E
Yield Stress (MPa)
*
80
60
40
20
0
Intact
Sham
SynAb
F
Failure Strain
1.0
0.8
0.6
0.4
0.2
0.0
Intact
Sham
SynAb
G
Failure Stress (MPa)
150
100
50
0
Intact
Sham
SynAb

Figure 5.10: Mechanics results from grip strain. A) Mean modulus, B) transition strain, C) transition stress, D) yield strain, E) yield stress, F) failure strain, and G) failure stress with standard deviation for Intact, Sham, and SynAb groups. Modulus and transition point were evaluated during both the 25% ramp and ramp to failure, while yield and failure were evaluated only during the ramp to failure. After 8 weeks of overload, SynAb samples had a lower modulus than Sham during ramp to failure as well as a lower yield stress. Line and * show $p<0.05$.

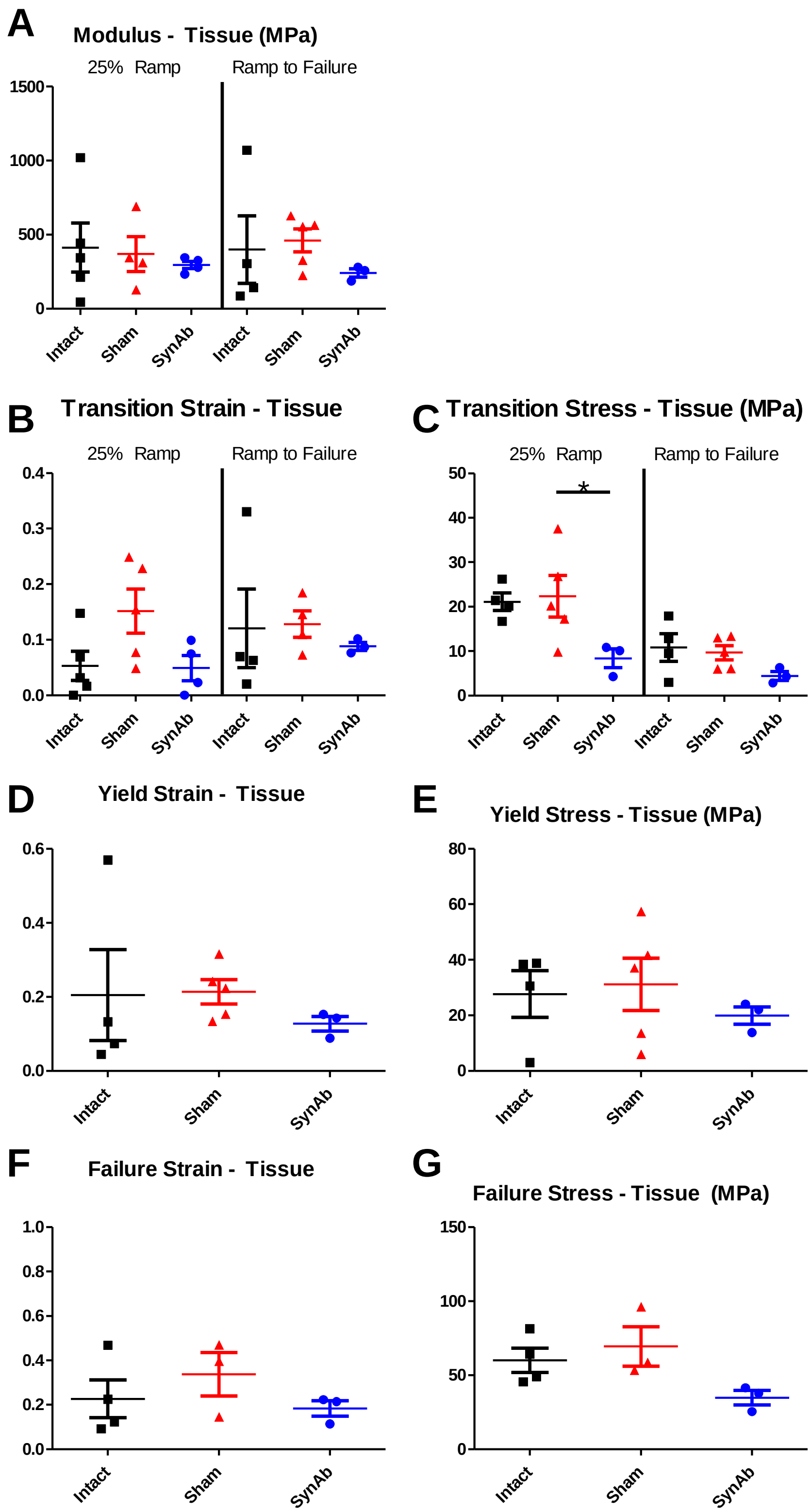
A
Modulus - Tissue (MPa)
25% Ramp
Ramp to Failure
1500
1000
500
0
Intact
Sham
SynAb
Intact
Sham
SynAb
B
Transition Strain - Tissue
25% Ramp
Ramp to Failure
0.4
0.3
0.2
0.1
0.0
Intact
Sham
SynAb
Intact
Sham
SynAb
C
Transition Stress - Tissue (MPa)
25% Ramp
Ramp to Failure
*
50
40
30
20
10
0
Intact
Sham
SynAb
Intact
Sham
SynAb
D
Yield Strain - Tissue
0.6
0.4
0.2
0.0
Intact
Sham
SynAb
E
Yield Stress - Tissue (MPa)
80
60
40
20
0
Intact
Sham
SynAb
F
Failure Strain - Tissue
1.0
0.8
0.6
0.4
0.2
0.0
Intact
Sham
SynAb
G
Failure Stress - Tissue (MPa)
150
100
50
0
Intact
Sham
SynAb

Figure 5.11: Mechanics results from optical strains. Calculated as described in methods, including A) mean modulus, B) transition strain, C) transition stress, D) yield strain, E) yield stress, F) failure strain, and G) failure stress with standard deviation for Intact (n=4), Sham (n=3), and SynAb (n=3) groups. Sample size reduced due to samples dropped for poor optical tracking. Modulus and transition point were evaluated during both the 25% ramp and ramp to failure, while yield and failure were evaluated only during the ramp to failure. Line and * show p<0.05.

To assess load transfer within the tissue, the ratio of microscale to tissue-level strain was calculated at the end of the 25% Ramp (Fig 5.12A). There was no significant difference between groups for the micro: tissue strain ratio with an average micro: tissue strain ratio for SynAb being 0.43, Sham 0.78, and Intact 0.82 (p=0.23, Fig 5.12B).

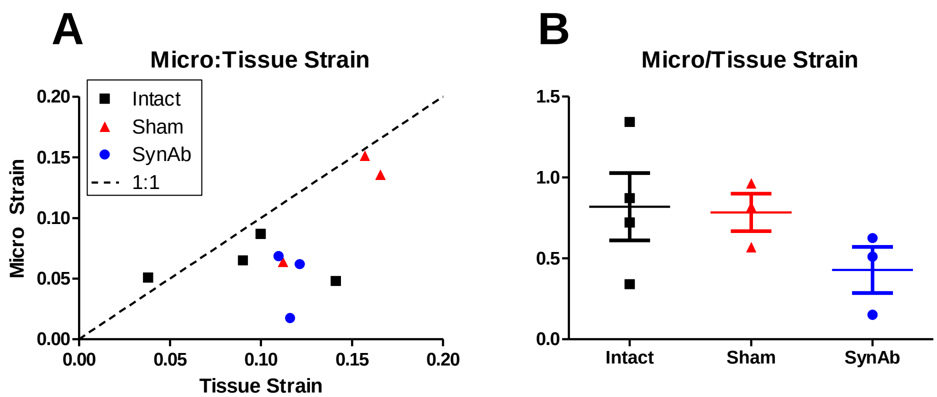

Figure 5.12: Multiscale mechanics results. A) Correlation between microscale strain measured from cell nuclei displacements plotted and sample tissue strain measured from digital image correlation, with 1:1 value showing perfect load transfer across length scales, with a value below the 1:1 line shows strain attenuation down the length scales. and B) mean ratio of micro: tissue strain with standard deviation.

5.3.5 Second Harmonic Generation (SHG)

SHG images at reference were acquired following preconditioning during the mechanical testing to assess collagen fiber orientation and damage (Fig 5.13A-C). After 8 weeks, there was a trending increase in SynAb DAF compared to Intact ($p=0.15$), with SynAb trending 92% larger than Intact ($p=0.15$), but not compared to Sham ($p=0.39$, Fig 5.13D). At 8 weeks, there were no differences between groups in mean fiber angle ($p=0.20$, Fig 5.13E).

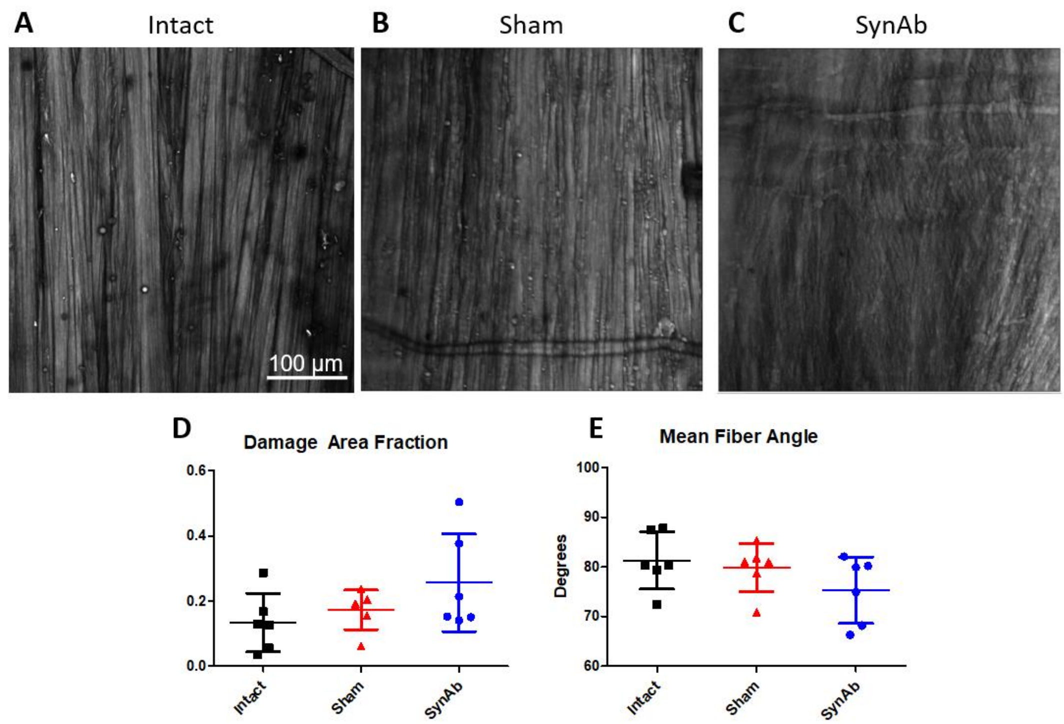

Figure 5.13: Representative SHG images and analysis. Representative z-projections of SHG stacks for A) Intact, B) Sham, and C) SynAb. D) Damage area fraction (DAF) and E) mean fiber orientation with standard deviation between Intact, Sham, and SynAb groups calculated from SHG images taken under preload.

5.4 Discussion

We observed degenerative structural and functional changes in SynAb tendons compared to our Sham and Intact controls. Structurally, there was an increase in tendon CSA at 8 weeks post-surgery, an increase in cell density, a decrease in matrix organization, and an increase in collagen fibril diameter. Mechanically, there was a decrease in modulus and yield stress at 8 weeks post-surgery. These alterations indicate sustained tendon degeneration after 8 weeks of overload.

Overall, SynAb overload led to a decrease in modulus and yield stress when compared to the Sham control, while yield strain, transition behavior, and failure behavior were unchanged. As SynAb tendons experienced an increase in CSA and a concurrent decrease in modulus, the tissue is mechanically inferior. Although the other metrics were not statistically significant, qualitatively there is a clear downward shift for transition, yield, and failure stresses for SynAb. Significance is likely hindered by the relatively low sample size. Interestingly, SynAb tendons also have an increase in collagen area fraction and increase in mean fibril diameter, which are typically correlated with an increase in tendon stiffness [25,209,210]. The lack of explicit impairment at the fibril level also includes the similarity in the micro: tissue strain ratios between the groups, showing that this metric of multiscale load transfer has not been affected. While the fibril level changes may suggest an increase in modulus, they are in balance with the other observed structural changes in the tissue.

While interpreting this work against the landscape of tendon clinical research and animal models of tendon disorders, we developed a new two-dimensional framework to distinguish between overload and overuse and the transition from adaptation (exercise) to degeneration (Fig 5.14). This new framework separates the role of load from cycle number (along the x- and y- axes) and captures many types of activity that are a combination of load and cycle number. This framework suggests that as tendons transition from homeostasis to a degenerative state, there are likely different mechanisms due to overload and overuse environments and this suggests that unique animal models may be important to study these potentially different pathways and mechanisms (Fig 5.14, dashed boxes). This new framework can be applied to include other loading environments important to tendon clinical and basic research such as immobilization and strength training. This framework also includes the positive adaptation that occurs with moderately increased load and cycle number (Fig 5.14). Positive adaptation to increased loading without experiencing detrimental functional changes or pain is observed by increased cross-sectional area and stiffness after habitual exercise [29,78,81,82,211]. The thresholds between tendon homeostasis, tendon adaptation, and tendon degeneration are driven by a combination of loading components, as well as shifts due to other factors including age, genetics, lifestyle, and other medical conditions [29].

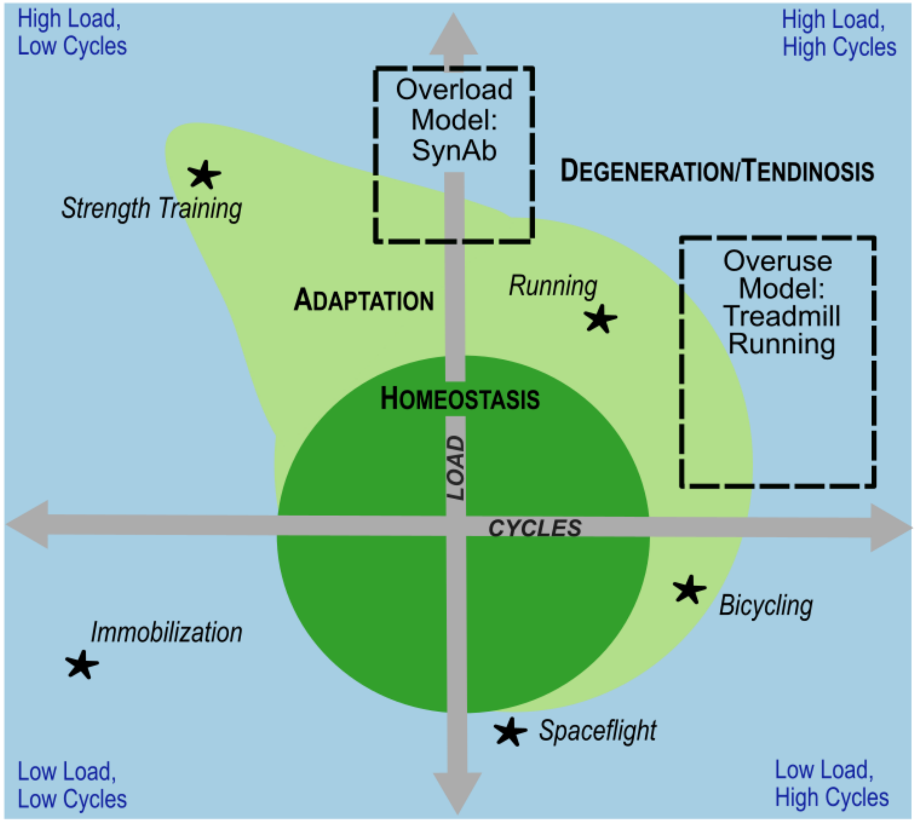

Figure 5.14: Tendon loading framework. Schematic illustrating the changes in response to altered activity via load and frequency. The "Cycles" and "Load" axes allow for differentiation between high load magnitudes and high load cycle numbers. The dark green circle indicates the region in which normal activity incudes no changes, the light green region indicates where increased activity leads to positive adaptation, and the blue region indicates were degeneration and/or impairment occur. Asterisks indicate representative activities. Black, dashed rectangles indicate approximate locations of various animal models.

Our findings and our proposed framework for tendon overload and overuse as different degenerative mechanisms can be compared to changes to the supraspinatus tendon observed Abraham et al. [193]. In the context of our proposed framework (Fig 5.14), the normal cage activity group would be within the homeostatic region, the destabilization group (overload) would be high on the loading y-axis within the degeneration region, and the overuse downhill treadmill running group has both increased load and cycle, so would be in the “High Load, High Cycles” region between the two axes. Notably, the overuse group in their study did not degenerate, but remained within the adaptation region of our proposed framework [193]. This is like several studies of Achilles’ tendon overuse that show adaptation but not degeneration [120,124,184].

We observed an increase in tendon CSA at 8 weeks after SynAb. This finding is consistent with both tendon adaptation and degeneration, thus additional measurements were taken to elucidate where the tendon changes occur along the adaptation to degeneration continuum (boundary between adaptation and degeneration, Fig 5.14). For example, human tendon CSA adaptively increases with both endurance training and resistance training [78,81] and increases with tendinopathy [64,92]. We observed hypercellularity at 8 weeks and trend for decrease in matrix organization after SynAb, consistent with degenerative alterations due to overload in this model. Increased cell density and decreased organization similarly occurs in human tendinosis and ruptured tendons [94,181,191]. We also observed decreases in the overall disorganization of the tendon matrix following overload in our histological PSR images. Matrix disorganization and loss of collagen alignment are hallmark changes observed in degenerative tendon [118,212–214]. While we did not observe a significant decrease in DAF from SHG images, the imaging ROI during mechanical testing was chosen to be an area of tissue with highly aligned tenocytes to allow for cell tracking. As a result, for SynAb samples, the SHG images were taken of the most structurally preserved regions. Finally, our SynAb tendons observed an increase in collagen fibril diameter, consistent with changes seen in human degenerative tendons [215]. While some of the structural changes could be examples of tendon adaptation, the observed decrease in tendon modulus when combined with an increase in matrix disorganization suggests that the SynAb overload results in a degenerate tendon, rather than an adapted one [97–100].

Abraham et al. recently investigated the effect of different loading conditions on mouse supraspinatus tendon, including unloading (via botulinum toxin A), normal activity, overuse (via downhill treadmill running), and joint destabilization (via surgical excision of the synergist infraspinatus tendon) [193]. Though it was not possible to confirm increased load to the remaining supraspinatus tendon following SynAb, the joint destabilization group in this forelimb study is like our SynAb overload group and was noted by the authors to be inspired by the hindlimb synergist ablation models [133,193]. Abraham et al. also observed a similar increase in tendon CSA in their destabilization group akin to our SynAb group. For mechanics they also observed a decrease in stiffness, and their destabilization group lead to decreases in maximum force and ultimate stress as well. Our findings for increased CSA and cell density at 8 weeks are generally consistent with previous SynAb studies of the plantaris tendon, where histology demonstrated an increase in CSA but no increase in cell density at early timepoints of 1 and 4 weeks [133]. However, in a second study by the same group in plantaris tendon, no changes in CSA or cell density were observed 4 weeks post-surgery [134]. More broadly, the mechanical behavior for Intact was consistent with previous findings for healthy tissue [43].

Several animal studies have identified structural and functional changes that occur following overuse, especially in rodent overuse models like treadmill running

[98,102,103,184,194,195]. However, the presence of degenerative changes with treadmill running are highly variable and depend on the duration of training as well as with the incline/decline used during treadmill running, which is correlated with magnitude of load [186]. For rotator cuff and supraspinatus tendon overuse, treadmill running that is done using a downhill incline is consistently degenerative, with increases in collagen fiber disorganization, cell density, CSA, and decreases in modulus and maximum stress [90,98]. However, other overuse protocols, particularly with hind limb tendons, are less consistently degenerative. For example, no differences were found in tendon CSA or elastic properties in a rat Achilles tendon using a downhill running model [184], while another downhill model showed increases in collagen fiber disorganization and cross-sectional area [98]. Some uphill running models show increases in collagen fiber disorganization, and cell density [213], while others show no differences between running subjects and controls [216]. In the context of our proposed framework (Fig 5.14), flat treadmill running studies would be examples of overuse, with uphill/downhill running models representing overuse models with possible moderate overload. Further, these previous results show that varying levels of increased cycles, or cycles in combination with increased load by changing incline during running, can result in adaptation or degeneration, seemingly moving from homeostasis with increasing intensity.

This study has some limitations. First, in vivo loads were not measured. Although the observed changes in tendon size (i.e., increased CSA) partially confirms that the plantaris tendon was effectively overloaded following SynAb, we did not directly confirm increased in vivo loads in this study. Based on a simple ratio of CSA of the plantaris and Achilles, we estimate that the load increased by a factor of 5.

Second, no inflammation assays were performed in this study to account for immunomodulatory effects following SynAb. We saw an early inflammatory response to surgery with the formation of granulation scar tissue in the space where the Achilles' tendon was removed; however, it is likely this inflammation resolved within a short time after surgery. By eight weeks, we did not observe a noticeable inflammatory response, however, the increased cellularity indicated active remodeling that would include upregulation of cytokines [217]. Finally, though previous studies have considered 8 weeks sufficient for chronic changes, it is possible that further mechanical impairment and structural disorganization could occur with prolonged chronic overload.

Inflammation is an important part of the tendon healing cycle; when the healing response is dysregulated or tendon degeneration surpasses the tissue's intrinsic healing ability, aberrant remodeling occurs [218]. In our study, the acute overload from surgical resection, as well as iatrogenic effects from the surgery itself, may illicit an inflammatory response. The presence of inflammatory and degenerative changes in adjacent tissues in tendinopathic limbs shows that inflammation can be cross-tissue and that the granulation tissue caused by the Achilles ablation in our model likely has biological effects on the plantaris tendon [29].

In summary, this study used a SynAb model to overload tendon in vivo and demonstrated the structural and functional changes up to 8-weeks using longitudinal high-resolution MRI, histology, SHG imaging, SBF-SEM, and multiscale mechanics. We observed that overload, without increasing the number of loading cycles, is sufficient to induce degenerative changes in cross-sectional area, cellularity, matrix organization, fibril diameter, modulus, and yield stress at 8-weeks. We also introduce a new framework for evaluating tendon loading that separates overload (increased magnitude) from overuse (increased cycles). It is likely that the landscape of pathology is not uniform between tendon overload and overuse, and these differences may explain the discrepancies between the asymptomatic degeneration that precedes tendon rupture and painful tendinopathy. This work establishes SynAb as a model to study overload-induced degeneration, separate from overuse, and can be used to study different mechanisms and treatments between the tendon overload and overuse injuries. Additionally, this new visual framework more clearly highlights the complexities of tendon's remodeling landscape and can help researchers and clinicians to discuss the effects of tendon loading.

Chapter 6

SUMMARY AND FUTURE DIRECTIONS

6.1 Summary

Chronic tendon injuries, such as tendinopathy, are exceedingly common and can be debilitating for recreational activities, work, and everyday quality of life. Further, there is evidence that acute tendon ruptures may result from unperceived tendon degeneration. While the link between excess mechanical loading and tendon injury is well established, the mechanisms of degenerative progression leading to clinical disorders is not fully elucidated, nor elements which lead to diverging endpoints such as tendinopathy or tendon rupture. As clinical diagnosis of these tendon disorders typically occurs after significant degeneration has already taken place (after pain initiates in tendinopathy, or after acute rupture), *ex vivo* studies and *in vivo* animal models are essential to investigating the changes occurring in tendon with altered loading states.

The objective of this thesis was to evaluate the structural and functional changes occurring after tendon was overloaded in an *in vivo* animal model. In Chapter 3, multiscale mechanical testing and electron microscopy was completed to determine which bathing solution best preserves *in vivo* damage conditions during mechanical testing. This study quantified the mechanical properties of the tendon equilibrated in two different solutions, the microscale damage experienced by the tendon after a single loading ramp, and the collagen fibril diameter and density. Analysis of the tissue-scale mechanics showed that using a solution of saline with 20 kD polyethylene glycol (SPEG) leads to a tendon with higher modulus and higher inflection point stress. The tendons equilibrated in SPEG also showed an increase in damage, measured as a larger delta value between baseline and final loading curves for transition strain, inflection stress, and modulus. However, the SPEG samples had a lower amount non-recoverable sliding from microscale measurements. The TEM images showed that samples equilibrated in SPEG as opposed to another commonly used bath (PBS) had a collagen fibril diameter and density more like that of fresh tendon. This work thus concluded that using SPEG more accurately preserves fresh tendon structure and that swelling caused by other baths effect the multiscale mechanics and damage of tendon.

In Chapter 4, the 3D ultrastructure of collagen fibrils was evaluated in tendons using Serial Block Face Scanning Electron Microscopy (SBF-SEM) and an adapted u-net deep convolutional neural network to segment the collected image stacks. After segmentation, a 3D reconstruction of the collagen fibrils was created to evaluate the differences in ultrastructure between rat tail tendon fascicles, a positional tendon, and rat plantaris tendon, an energy-storing tendon. In this work, a u-net workflow automatically segmented collagen fibril cross sections more accurately than Otsu thresholding, the typical field standard, and orders of magnitude more quickly than manual segmentation. The segmented image stack was also successfully reconstructed and analyzed using a combination of imaging software, to show that the plantaris tendon had a larger fibril tortuosity than the tail tendon. This work not only provided new information on the 3D geometric differences between tendon types, but also established a method to investigate 3D geometries of collagen fibrils for fiber-reinforced tissues.

In Chapter 5, the effect of chronic overload on structural and functional changes in tendon was evaluated. To help describe the differences in overload and overuse, a new framework was developed to interpret the tendon loading environment. To expose tendons to chronic overload, a surgical model called Synergist Ablation (SynAb) was used, where a target tendon (plantaris) was overloaded by surgically ablating its synergist (Achilles) in skeletally mature rats. Changes in gross morphology were quantified from high resolution MRI images taken before and after surgical intervention. Hematoxylin and eosin, as well as picrosirius red with polarized light, histology staining was competed on tendon samples to investigate collagen fiber alignment and cellular morphology. Collagen alignment was also assessed using second harmonic generation (SHG) imaging, while collagen fibril geometry was assessed using serial block face scanning electron microscopy (SBFSEM). Multiscale mechanics were measured from uniaxial tension tests on tendon samples completed during confocal imaging. After 8 weeks, overloaded tendons had larger tendon cross-sectional areas, higher cellular density, decreased collagen fiber alignment, increased collagen fibril diameter, decreased collagen density, and decreased modulus and yield stress. To confirm that our surgical model was increasing the magnitude of the load (overload) without increasing the number of loading cycles (overuse), activity monitoring was used to measure the distance traveled by animals overnight. No differences were seen after surgery, confirming that animal activity level stayed constant. These findings confirmed that chronic overload without overuse is sufficient to induce degeneration in tendon.

6.2 Future Directions

6.2.1 Degeneration Mitigation

While important new findings were elucidated in Chapters 3 to 5, this thesis also establishes methods and questions for further avenues of inquiry. Perhaps most pressingly, the visual framework introduced in Chapter 5 is foundational for translating animal models to humans or large animal models. Clinical researchers have found that eccentric/concentric exercise and strength training can be restorative with regards to symptoms in clinical tendinopathy patients [219–221]. Introducing exercise treatments following the overload model used in this dissertation to evaluate whether tendon structure and function can be restored; or rather, whether the observed degeneration is reversible with intervention. Subjecting animals to a moderate exercise regimen (either with moderate increases in load or moderate increases in loading cycles) prior to inducing overload via SynAb would give insights into the combinations of activity that can lead to tendon adaptation or tendon degeneration, as well as whether metabolically active tissue from moderate exercise is more readily adaptable and resistant to degeneration, or if all loading is additive [82,119,187,193,222]. Exercised tendons have a larger cross-section and increasing mechanical strength, which could prepare tendons to sustain the increases from the overload model, [77–81]. In contrast to introducing additional (preceding moderate exercise or eccentric/concentric exercise after surgery) load to the tendon, an attenuated SynAb model could also be used, to evaluate tendon changes to a lower amount of increased load by ablating the plantaris tendon instead of the Achilles tendon.

6.2.2 Effect of Cells on Multiscale Mechanical Environment

As mentioned in Chapter 3 and Chapter 5, mechanically testing tendon samples leads to multiscale damage. However, in all the work completed in this dissertation, only fresh-frozen, nonviable tissues were used. Evaluating multiscale mechanics with samples where cells are still viable could also help establish the role of cellular response during mechanical loading. Previous work, in addition to the work described in Chapter 3, show non-recoverable fiber sliding at relatively low strains [43,47]. Physiological activity includes numerous cycles at these strains in typical activity, frequently without injury. It is likely that cellular activity is responsible for recovering this sliding and tendon elongation [223]. Though viable and non-viable mechanical testing has been completed and showed little difference macroscale mechanics, investigation at the microscale could determine how tendon equilibrium is maintained [224]. In addition to evaluating how cells contribute to interfibrillar sliding, cellular membranes could be stained in addition to cellular nuclei to measure cellular aspect ratio changes and thus cellular deformation in response to loading. There is currently debate whether tendon degeneration originates from damaged extracellular matrix or aberrant cellular responses to changes in mechanotransduction [56,183,225]. Evaluating the cellular deformations in addition to the cellular nuclei deformations would add needed information into the loading environment of the cell during tendon loading. Even further, multiscale mechanical testing with viable sample could also be used to evaluate how cellular structures such as the actin cytoskeleton deform during mechanical loading [194,226,227].

6.2.3 Collagen Fibrillar Ultrastructure and Multiscale Translation Between Species

In Chapter 4, a new analysis method which allows for high throughput of 3D collagen fibril geometry analysis was introduced and applied to investigating overloaded tendon. Differences between collagen fibril diameter by region within a single tendon has been previously described in equine flexor tendon, but no description for differences in 3D ultrastructure [228]. A study in the intra-tendon regional differences would be helpful to establish the inherent variability of the 3D collagen fibrillar ultrastructure and may shed light on the heterogenous nature of tendon degeneration [229]. In addition, to apply the methods used here in rodents to human, quantification of the 3D collagen fibrillar structure from large animal or human tendon would be useful. Rodents have differing tendons in comparison to larger species like horse and human in that they lack a fascicular structure [206]. As previous work has shown differences in the collagen fibrils near cells, it is possible that differences exist in the ultrastructure of rodent tendon and larger species [16]. Beyond establishing baseline 3D collagen fibrillar structure, traditional electron microscopy has shown collagen disruption following mechanical loading as collagen kinking [35,115,230]. Imaging the 3D structure of collagen fibrils after typical sub-rupture loading would shed light on whether fibrils with a helical ultrastructure that convert tensile load to compressive load are more robust during loading. Another issue in translating the mechanics observed in multiscale testing between the species is the size of tendon necessary for mechanical analysis. In order to discover this relationship, parallel mechanics tests could be completed on whole cadaveric human tendons, then tendon samples appropriately sectioned for use on multiscale tester to see how sectioning effects the load transfer within the tissue. This characterization is important as the intrafascicular matrix is an important contributor to tendon mechanics, and sectioning could disrupt these mechanisms.

Another issue in translating the mechanics observed in multiscale testing between the species is the size of tendon necessary for mechanical analysis. The multiscale mechanical testing used in this dissertation is only possible with tendon samples around 1 mm for the major and minor axis, which are much smaller than human load-bearing tendons. If the effect on sectioning tendons down in size were described, it would be possible to complete the assays in this dissertation on human tissue. To describe this relationship, parallel mechanical tests could be completed on whole cadaveric human tendons, then tendon samples appropriately sectioned for use on multiscale tester to see how sectioning effects the load transfer within the tissue. This characterization is important as the interfascicular matrix is a well-described, important contributor to tendon mechanics, and sectioning could disrupt these mechanisms [231–234].

6.2.4 Loading Protocol Effects on Multiscale Mechanics

The mechanical testing completed in this thesis used only a single ramp and hold before a ramp to failure in the loading protocol. As physiological loading is repetitive, and completed to various levels of applied strain, a more complex loading profile is necessary to better evaluate the role of microscale damage in tendon mechanical behavior. The results of Chapter 3, as well as previous work has suggested that microscale damage via non-recoverable sliding occurs prior to collagen fibril rupture [43,44,47]. It also is clear from previous microtensile tests that microscale sliding increases with increased applied load, and increased applied loads in succession [11,43,44]. However, it is not clear whether this damage threshold for non-recoverable sliding is dependent on the maximum strain reached, or the loading history (applied strain). Repetitive strain at the same target strain could determine how microscale damage accumulates in tendon, while loading protocols with variations in other factors (loading duration, rate, type) could further establish the important factors in tendon damage.

6.2.5 Inflammation in SynAb Model

One of the limitations of the SynAb model used in this thesis is the inflammatory response created by the surgery itself. Inflammatory markers, such as MMPs, TIMPs, cytokines, and prostaglandins, could be used to ascertain the timeline of iatrogenic inflammation as opposed to inflammation resulting from tendon degeneration [29,218,235]. Introducing a short-term anti-inflammatory regimen to this model could more accurately recapitulate the physiology of tendon overload in humans but is dependent on a better understanding of the inflammatory timelines and targets in this model. Once a description of the short-term, iatrogenic inflammatory timeline in the SynAb model is described, the inflammatory profile in overload compared to overuse studies could be assessed for possible therapeutic targets [236].

6.2.6 Relating Fiber and Microscale Strain with Molecular Damage

Previous work investigating the microscale mechanics of tendon has used photobleached lines or grids to evaluate the overall fiber sliding and strains during tensile loading. In this thesis, this method was used in Chapter 3, but the displacements of stained cellular nuclei were used for microscale mechanics in Chapter 5. One of the most surprising results of this thesis was the relatively nonuniform microscale behavior exhibited during unloading by triads of cells

(Appendix 1). To relate the slightly larger scale line/grid deformations to the movement of cellular nuclei, these methods could be completed concurrently. Further, a collagen hybridizing stain could be used with cellular displacement to connect the fibril sliding observed in these microscale measurements with collagen fibril denaturation because of collagen fibril failure [53,54,237,238]. With respect to the overload model introduced in Chapter 5, tendon samples could be stained prior to any *ex vivo* mechanical loading to assess the amount of collagen damage from the *in vivo* loading environment post-surgery. It is possible that the *in vivo* overload is damaging collagen, especially at early time points before tendon can remodel.

6.3 Final Conclusions

This dissertation investigated tendon structure, function, and damage following *in vivo* overload of tendon in a relatively unexplored animal model. To evaluate tendon structure, a full workflow to image and analyze 3D collagen fibrillar ultrastructure using machine learning was created. To help researchers and clinicians discuss and interpret the complexities of tendon loading and tendon injuries, a new visual framework for use in the field was designed. These findings establish that *in vivo* overload is sufficient to induce tendon degeneration and help link both macroscale to microscale mechanics and damage and degenerative structural changes to impaired tendon mechanics. The outcomes from this thesis provide valuable insight into tendon damage and degeneration with mechanical loading, while the novel methods can be deployed to evaluate multi-scale structure-function in tendons and other highly aligned collagenous tissue. Overall, this work shows that overload alone induces multifaceted tendon degeneration, and this new knowledge and experimental assays can be used to inform tendon injury treatment and prevention.

REFERENCES

1. Screen HRC, Berk DE, Kadler KE, Ramirez F, Young MF. Tendon functional extracellular matrix. J Orthop Res [Internet]. NIH Public Access; 2015 [cited 2018 Jul 27];33:793–9. Available from: http://www.ncbi.nlm.nih.gov/pubmed/25640030
2. Riley G. Tendinopathy—from basic science to treatment. Nat Clin Pract Rheumatol [Internet]. 2008;4:82–9. Available from: http://www.nature.com/doifinder/10.1038/ncprheum0700
3. Kastelic J, Galeski A, Baer E. The multicomposite structure of tendon. Connect Tissue Res. England; 1978;6:11–23.
4. Thorpe CT, Birch HL, Clegg PD, Screen HR. The role of the non-collagenous matrix in tendon function INTERNATIONAL JOURNAL OF EXPERIMENTAL PATHOLOGY. 2013;
5. Buckley MR, Evans EB, Matuszewski PE, Chen YL, Satchel LN, Elliott DM, et al. Distributions of types I, II and III collagen by region in the human supraspinatus tendon. Connect Tissue Res [Internet]. Taylor & Francis; 2013 [cited 2020 Nov 13];54:374–9. Available from: https://www.tandfonline.com/doi/abs/10.3109/03008207.2013.847096
6. Murata H, Nishizono H, Miyoshi M. Postnatal Development of Structure and Arrangement of Tendon Cells A Scanning and Transmission Electron Microscope Study in the Rat Calcaneal Tendon. Okajimas Folia Anal Jpn. 2000.
7. Richardson SH, Starborg T, Lu Y, Humphries SM, Meadows RS, Kadler KE. Tendon Development Requires Regulation of Cell Condensation and Cell Shape via Cadherin-11-Mediated Cell-Cell Junctions. Mol Cell Biol [Internet]. American Society for Microbiology; 2007 [cited 2022 Apr 27];27:6218–28. Available from: https://journals.asm.org/journal/mcb
8. Zhang C, Zhu J, Zhou Y, Thampatty BP, Wang JH-C, Li J. Tendon Stem/Progenitor Cells and Their Interactions with Extracellular Matrix and Mechanical Loading. 2019 [cited 2019 Dec 10]; Available from: https://doi.org/10.1155/2019/3674647
9. Svensson RB, Herchenhan A, Starborg T, Larsen M, Kadler KE, Qvortrup K, et al. Evidence of structurally continuous collagen fibrils in tendons. Acta Biomater [Internet]. Acta Materialia Inc.; 2017;50:293–301. Available from: http://dx.doi.org/10.1016/j.actbio.2017.01.006
10. Provenzano PP, Vanderby R. Collagen fibril morphology and organization: Implications for force transmission in ligament and tendon. Matrix Biol

[Internet]. Matrix Biol; 2006 [cited 2020 Sep 30];25:71–84. Available from: https://pubmed.ncbi.nlm.nih.gov/16271455/
11. Szczesny S, Elliott D. Interfibrillar shear stress is the loading mechanism of collagen fibrils in tendon. Acta Biomater. 2008;86:3279–88.
12. Peterson BE, Szczesny SE. Dependence of tendon multiscale mechanics on sample gauge length is consistent with discontinuous collagen fibrils. Acta Biomater [Internet]. 2020;117:302–9. Available from: https://www.sciencedirect.com/science/article/pii/S1742706120305699
13. Heinemeier KM, Kjaer M. In vivo investigation of tendon responses to mechanical loading. J Musculoskelet Neuronal Interact. 2011;11:115–23.
14. Birch HL. Tendon matrix composition and turnover in relation to functional requirements. Int J Exp Pathol [Internet]. Wiley-Blackwell; 2007 [cited 2019 Aug 26];88:241–8. Available from: http://www.ncbi.nlm.nih.gov/pubmed/17696905
15. Herod TW, Chambers NC, Veres SP. Collagen fibrils in functionally distinct tendons have differing structural responses to tendon rupture and fatigue loading. Acta Biomater [Internet]. Acta Materialia Inc.; 2016;42:296–307. Available from: http://dx.doi.org/10.1016/j.actbio.2016.06.017
16. Safa BN, Peloquin JM, Natriello JR, Caplan JL, Elliott DM. Helical fibrillar microstructure of tendon using serial block-face scanning electron microscopy and a mechanical model for interfibrillar load transfer. J R Soc Interface [Internet]. Royal Society Publishing; 2019 [cited 2021 Feb 2];16:20190547. Available from: https://royalsocietypublishing.org/doi/10.1098/rsif.2019.0547
17. Pingel J, Lu Y, Starborg T, Fredberg U, Langberg H, Nedergaard A, et al. 3-D ultrastructure and collagen composition of healthy and overloaded human tendon: evidence of tenocyte and matrix buckling. J Anat [Internet]. 2014;224:548–55. Available from: http://www.ncbi.nlm.nih.gov/pubmed/24571576
18. Kalson NS, Malone PSC, Bradley RS, Withers PJ, Lees VC. Fibre bundles in the human extensor carpi ulnaris tendon are arranged in a spiral. J Hand Surg Eur Vol. 2012;37:550–4.
19. De Campos Vidal B. Image analysis of tendon helical superstructure using interference and polarized light microscopy. Micron [Internet]. 2003;34:423–32. Available from: https://ac.els-cdn.com/S0968432803000398/1-s2.0-S0968432803000398-main.pdf?_tid=f9a6de13-f288-4344-bd37-4add19251400&acdnat=1528729188_ad14b6f2f4a579d97d6c4fdbca43d5f8
20. Franchi M, Ottani V, Stagni R, Ruggeri A. Tendon and ligament fibrillar crimps give rise to left-handed helices of collagen fibrils in both planar and helical crimps. J Anat. 2010;216:301–9.
21. Ottani V, Raspanti M, Ruggeri A. Collagen structure and functional implications. Micron [Internet]. 2001;32:251–60. Available from: https://ac.els-cdn.com/S0968432800000421/1-s2.0-S0968432800000421-main.pdf?_tid=1682d1b1-3a5a-4149-9423-

8e3371fcdc51&acdnat=1528487633_be230b55a6884ccd47aa4112e30aaab5
22. Holmes DF, Lu Y, Starborg T, Kadler KE. Collagen Fibril Assembly and Function. 2018. p. 107–42. Available from: http://linkinghub.elsevier.com/retrieve/pii/S007021531830036X
23. Depalle B, Qin Z, Shefelbine SJ, Buehler MJ. Influence of cross-link structure, density and mechanical properties in the mesoscale deformation mechanisms of collagen fibrils. J Mech Behav Biomed Mater [Internet]. 2015 [cited 2019 Jul 19];52:1–13. Available from: https://linkinghub.elsevier.com/retrieve/pii/S175161611400201X
24. Svensson RB, Mulder H, Kovanen V, Magnusson SP. Fracture mechanics of collagen fibrils: Influence of natural cross-links. Biophys J. 2013;104:2476–84.
25. Parry DAD. The molecular fibrillar structure of collagen and its relationship to the mechanical properties of connective tissue. Biophys Chem. Elsevier; 1988;29:195–209.
26. Evans, Na, Stanish, WD. The basic science of tendon injuries. 2000 [cited 2019 Nov 30]; Available from: http://www.idealibrary.com
27. Lillie JH, MacCallum DK, Scaletta LJ, Occhino JC. Collagen structure: Evidence for a helical organization of the collagen fibril. J Ultrasructure Res [Internet]. 1977;58:134–43. Available from: https://pdfs.semanticscholar.org/44fd/9baec93ea0ebc876fb9f759d37eeffa26dc0.pdf
28. Starborg T, Kadler KE. Serial block face-scanning electron microscopy: A tool for studying embryonic development at the cell-matrix interface. Birth Defects Res Part C - Embryo Today Rev [Internet]. Wiley-Blackwell; 2015;105:9–18. Available from: http://doi.wiley.com/10.1002/bdrc.21087
29. Abate M, Gravare Silbernagel K, Siljeholm C, Di Iorio A, De Amicis D, Salini V, et al. Pathogenesis of tendinopathies: inflammation or degeneration? Arthritis Res Ther [Internet]. BioMed Central; 2009 [cited 2022 Jan 17];11:235. Available from: /pmc/articles/PMC2714139/
30. Fessel G, Li Y, Diederich V, Guizar-Sicairos M, Schneider P, Sell DR, et al. Advanced Glycation End-Products Reduce Collagen Molecular Sliding to Affect Collagen Fibril Damage Mechanisms but Not Stiffness. PLoS One [Internet]. Public Library of Science; 2014 [cited 2022 Apr 27];9. Available from: /pmc/articles/PMC4217736/
31. Bansode S, Bashtanova U, Li R, Clark J, Müller KH, Puszkarska A, et al. Glycation changes molecular organization and charge distribution in type I collagen fibrils. [cited 2020 Mar 7]; Available from: https://doi.org/10.1038/s41598-020-60250-9
32. Silver FH, Kelkar N, Deshmukh T. Molecular Basis for Mechanical Properties of ECMs: Proposed Role of Fibrillar Collagen and Proteoglycans in Tissue Biomechanics. Biomol 2021, Vol 11, Page 1018 [Internet]. Multidisciplinary Digital Publishing Institute; 2021 [cited 2021 Jul

19];11:1018. Available from: https://www.mdpi.com/2218-273X/11/7/1018/htm
33. Szczesny SE, Caplan JL, Pedersen P, Elliott DM. Quantification of interfibrillar shear stress in aligned soft collagenous tissues via notch tension testing. Sci Rep. Nature Publishing Group; 2015;5.
34. Veres SP, Harrison JM, Lee JM. Repeated Subrupture Overload Causes Progression of Nanoscaled Discrete Plasticity Damage in Tendon Collagen Fibrils. 2013;731–7.
35. Fung DT, Wang VM, Laudier DM, Shine JH, Basta-Pljakic J, Jepsen KJ, et al. Subrupture tendon fatigue damage. J Orthop Res. 2009;27:264–73.
36. Sasaki N, Odajima S. Elongation mechanism of collagen fibrils and force-strain relations of tendon at each level of structural hierarchy. J Biomech. 1996;29:1131–6.
37. Miller KS, Edelstein L, Connizzo BK, Soslowsky LJ. Effect of preconditioning and stress relaxation on local collagen fiber re-alignment: Inhomogeneous properties of rat supraspinatus tendon. J Biomech Eng. American Society of Mechanical Engineers Digital Collection; 2012;134.
38. Lynch HA, Johannessen W, Wu JP, Jawa A, Elliott DM. Effect of Fiber Orientation and Strain Rate on the Nonlinear Uniaxial Tensile Material Properties of Tendon. J Biomech Eng [Internet]. American Society of Mechanical Engineers Digital Collection; 2003 [cited 2022 Apr 27];125:726–31. Available from: https://asmedigitalcollection.asme.org/biomechanical/article/125/5/726/449192/Effect-of-Fiber-Orientation-and-Strain-Rate-on-the
39. Szczesny SE, Peloquin JM, Cortes DH, Kadlowec JA, Soslowsky LJ, Elliott DM. Biaxial tensile testing and constitutive modeling of human supraspinatus tendon. J Biomech Eng. 2012;134.
40. Lanir Y. Structure-function relations in mammalian tendon: the effect of geometrical nonuniformity. J Bioeng [Internet]. 1978 [cited 2018 Jul 30];2:119–28. Available from: http://www.ncbi.nlm.nih.gov/pubmed/681314
41. Szczesny SE, Fetchko KL, Dodge GR, Elliott DM. Evidence that Interfibrillar Load Transfer in Tendon is Supported by Small Diameter Fibrils and Not Extrafibrillar Tissue Components HHS Public Access. J Orthop Res [Internet]. 2017 [cited 2019 Aug 16];35:2127–34. Available from: https://www.ncbi.nlm.nih.gov/pmc/articles/PMC5503823/pdf/nihms-843468.pdf
42. Szczesny SE, Elliott DM. Incorporating plasticity of the interfibrillar matrix in shear lag models is necessary to replicate the multiscale mechanics of tendon fascicles. J Mech Behav Biomed Mater. Elsevier Ltd; 2014;40:325–38.
43. Lee AH, Elliott DM. Multi-Scale Loading and Damage Mechanisms of Plantaris and Rat Tail Tendons. J Orthop Res. Wiley; 2019;
44. Lee AH, Elliott DM. Freezing does not alter multiscale tendon mechanics and

damage mechanisms in tension. Ann N Y Acad Sci [Internet]. Wiley/Blackwell (10.1111); 2017 [cited 2018 Jul 30];1409:85–94. Available from: http://doi.wiley.com/10.1111/nyas.13460
45. Shepherd JH, Legerlotz K, Demirci T, Klemt C, Riley GP, Screen HRC. Functionally distinct tendon fascicles exhibit different creep and stress relaxation behaviour. Proc Inst Mech Eng H [Internet]. SAGE Publications; 2014 [cited 2022 Apr 28];228:49. Available from: /pmc/articles/PMC4361498/
46. Puxkandl R, Zizak I, Paris O, Keckes J, Tesch W, Bernstorff S, et al. Viscoelastic properties of collagen: synchrotron radiation investigations and structural model. Philos Trans R Soc B Biol Sci [Internet]. 2002;357:191–7. Available from: http://rstb.royalsocietypublishing.org/cgi/doi/10.1098/rstb.2001.1033
47. Lee AH, Szczesny SE, Santare MH, Elliott DM. Investigating mechanisms of tendon damage by measuring multi-scale recovery following tensile loading. Acta Biomater [Internet]. 2017 [cited 2017 Aug 29];57:363–72. Available from: http://linkinghub.elsevier.com/retrieve/pii/S1742706117302386
48. Lui PPY, Yung PSH. Inflammatory mechanisms linking obesity and tendinopathy. J Orthop Transl [Internet]. Elsevier; 2021 [cited 2021 Dec 16];31:80–90. Available from: https://linkinghub.elsevier.com/retrieve/pii/S2214031X21000784
49. Beach ZM, Bonilla KA, Dekhne MS, Sun M, Adams TH, Adams SM, et al. Biglycan Has a Major Role in Maintenance of Mature Tendon Mechanics. J Orthop Res [Internet]. John Wiley & Sons, Ltd; 2022;0–1. Available from: http://dx.doi.org/10.1002/jor.25299
50. Lujan TJ, Underwood CJ, Henninger HB, Thompson BM, Weiss JA. Effect of dermatan sulfate glycosaminoglycans on the quasi-static material properties of the human medial collateral ligament. J Orthop Res [Internet]. John Wiley & Sons, Ltd; 2007 [cited 2019 Jul 15];25:894–903. Available from: http://doi.wiley.com/10.1002/jor.20351
51. Docking SI, Cook J. How do tendons adapt? Going beyond tissue responses to understand positive adaptation and pathology development: A narrative review. J Musculoskelet Neuronal Interact [Internet]. International Society of Musculoskeletal and Neuronal Interactions (ISMNI); 2019 [cited 2021 Nov 10];19:300. Available from: /pmc/articles/PMC6737558/
52. Nakama LH, King KB, Abrahamsson S, Rempel DM. Evidence of tendon microtears due to cyclical loading in an in vivo tendinopathy model. J Orthop Res. 2005;23:1199–205.
53. Lin AH, Allan AN, Zitnay JL, Kessler JL, Yu SM, Weiss JA. Collagen denaturatio n is initiated upon tissue yield in both positional and energy-stor in g tendons ☆. Acta Biomater [Internet]. ACTBIO; 2020 [cited 2020 Oct 24];17. Available from: https://doi.org/10.1016/j.actbio.2020.09.056
54. Zitnay JL, Seob Jung G, Lin AH, Qin Z, Li Y, Michael Yu S, et al.

Accumulation of collagen molecular unfolding is the mechanism of cyclic fatigue damage and failure in collagenous tissues [Internet]. 2020. Available from: http://advances.sciencemag.org/

55. Lee AH, Elliott DM. Comparative multi-scale hierarchical structure of the tail, plantaris, and Achilles tendons in the rat. J Anat. Blackwell Publishing Ltd; 2019;234:252–62.
56. Cook JL, Purdam CR. Is tendon pathology a continuum? A pathology model to explain the clinical presentation of load-induced tendinopathy. Br J Sports Med. 2009;43:409–16.
57. Kaux JF, Forthomme B, le Goff C, Crielaard JM, Croisier JL. Current opinions on tendinopathy [Internet]. J. Sport. Sci. Med. Dept. of Sports Medicine, Medical Faculty of Uludag University; 2011 [cited 2020 Dec 9]. p. 238–53. Available from: http://www.jssm.org
58. Sharma P, Maffulli N. Biology of tendon injury: Healing, modeling and remodeling. J Musculoskelet Neuronal Interact. 2006;6:181–90.
59. Archambault JM, Wiley JP, Bray RC. Exercise loading of tendons and the development of overuse injuries. A review of current literature. Sports Med [Internet]. Sports Med; 1995 [cited 2023 Jan 5];20:77–89. Available from: https://pubmed.ncbi.nlm.nih.gov/7481284/
60. Woo SL-Y. MECHANICAL PROPERTIES OF TENDONS AND LIGAMENTS I. QUASI-STATIC AND NONLINEAR VISCOELASTIC PROPERTIES. ERRATUM Biorheol. 1983;345:385–96.
61. Heinemeier KM, Schjerling P, Heinemeier J, Magnusson SP, Kjaer M. Lack of tissue renewal in human adult Achilles tendon is revealed by nuclear bomb 14C. FASEB J. 2013;27:2074–9.
62. Arnoczky SP, Lavagnino M, Egerbacher M. The mechanobiological aetiopathogenesis of tendinopathy: Is it the over-stimulation or the under-stimulation of tendon cells? Int J Exp Pathol. 2007;88:217–26.
63. Bass E. Tendinopathy: why the difference between tendinitis and tendinosis matters. Int J Ther Massage Bodywork [Internet]. Massage Therapy Foundation; 2012 [cited 2018 May 15];5:14–7. Available from: http://www.ncbi.nlm.nih.gov/pubmed/22553479
64. Maffulli N, Khan KM, Puddu G. Overuse tendon conditions: Time to change a confusing terminology. Arthroscopy. W.B. Saunders; 1998;14:840–3.
65. Scott A, Backman LJ, Speed C. Tendinopathy: Update on Pathophysiology. J Orthop Sport Phys Ther [Internet]. 2015;45:833–41. Available from: http://www.jospt.org/doi/10.2519/jospt.2015.5884
66. Mutsuzaki H, Nakajima H, Wadano Y, Takahashi H, Sakane M. Influence of mechanical unloading on histological changes of the patellar tendon insertion in rabbits. Knee. Elsevier; 2015;22:469–74.
67. Khayyeri H, Blomgran P, Hammerman M, Turunen MJ, Löwgren A, Guizar-Sicairos M, et al. Achilles tendon compositional and structural properties are altered after unloading by botox. Sci Rep [Internet]. Nature Publishing Group;

2017 [cited 2021 Nov 8];7. Available from: /pmc/articles/PMC5638919/
68. Deymier AC, Schwartz AG, Lim C, Wingender B, Kotiya A, Shen H, et al. Multiscale effects of spaceflight on murine tendon and bone. Bone. Elsevier Inc.; 2020;131.
69. Johnson RB, Tsao AK, St. John KR, Betcher RA, Tucci MA, Benghuzzi HA. Effects of spaceflight on the attachment of tendons to bone in the hindlimb of the pregnant rat. Anat Rec - Part A Discov Mol Cell Evol Biol. 2005;282:147–56.
70. Woo SLY, Gomez MA, Woo YK, Akeson WH. Mechanical properties of tendons and ligaments. Biorheology. IOS Press; 1982;19:397–408.
71. Yamamoto N, Ohno K, Mayashi K, Kuriyama H, Yasuda K, Kaneda K. Effects of Stress Shielding on the Mechanical Properties of Rabbit Patellar Tendon. J Biomech Eng [Internet]. American Society of Mechanical Engineers Digital Collection; 1993 [cited 2022 Jan 19];115:23–8. Available from: http://asmedigitalcollection.asme.org/biomechanical/article-pdf/115/1/23/5766422/23_1.pdf
72. Hannafin JA, Arnoczky SP, Hoonjan A, Torzilli PA. Effect of stress deprivation and cyclic tensile loading on the material and morphologic properties of canine flexor digitorum profundus tendon: An in vitro study. J Orthop Res. 1995;13:907–14.
73. Almeida-Silveira MI, Lambertz D, Pérot C, Goubel F. Changes in stiffness induced by hindlimb suspension in rat Achilles tendon. Eur J Appl Physiol 2000 813 [Internet]. Springer; 2000 [cited 2022 Jan 19];81:252–7. Available from: https://link.springer.com/article/10.1007/s004210050039
74. Matsumoto F, Trudel G, Uhthoff HK, Backman DS. Mechanical Effects of Immobilization on the Achilles' Tendon. Arch Phys Med Rehabil. W.B. Saunders; 2003;84:662–7.
75. Heinemeier KM, Olesen JL, Haddad F, Schjerling P, Baldwin KM, Kjaer M. Effect of unloading followed by reloading on expression of collagen and related growth factors in rat tendon and muscle. J Appl Physiol [Internet]. American Physiological Society; 2009 [cited 2022 Jan 19];106:178–86. Available from: https://journals.physiology.org/doi/abs/10.1152/japplphysiol.91092.2008
76. Kinugasa R, Hodgson JA, Edgerton VR, Shin DD, Sinha S. Reduction in tendon elasticity from unloading is unrelated to its hypertrophy. J. Appl. Physiol. 2010. p. 870–7.
77. Kongsgaard M, Aagaard P, Kjaer M, Magnusson SP. Structural Achilles tendon properties in athletes subjected to different exercise modes and in Achilles tendon rapture patients. J Appl Physiol [Internet]. American Physiological Society; 2005 [cited 2022 Jan 19];99:1965–71. Available from: https://journals.physiology.org/doi/abs/10.1152/japplphysiol.00384.2005
78. Couppé C, Kongsgaard M, Aagaard P, Hansen P, Bojsen-Moller J, Kjaer M, et al. Habitual loading results in tendon hypertrophy and increased stiffness of

the human patellar tendon. J Appl Physiol [Internet]. American Physiological Society; 2008 [cited 2022 Jan 19];105:805–10. Available from: https://journals.physiology.org/doi/abs/10.1152/japplphysiol.90361.2008
79. Kongsgaard M, Reitelseder S, Pedersen TG, Holm L, Aagaard P, Kjaer M, et al. Region specific patellar tendon hypertrophy in humans following resistance training. Acta Physiol [Internet]. John Wiley & Sons, Ltd; 2007 [cited 2022 Apr 28];191:111–21. Available from: https://onlinelibrary.wiley.com/doi/full/10.1111/j.1748-1716.2007.01714.x
80. Kubo K, Ikebukuro T, Yata H, Tsunoda N, Kanehisa H. Time course of changes in muscle and tendon properties during strength training and detraining. J Strength Cond Res [Internet]. 2010;24:322–31. Available from: http://www.ncbi.nlm.nih.gov/pubmed/19996769%5Cnhttp://graphics.tx.ovid.com/ovftpdfs/FPDDNCJCJDAEIG00/fs046/ovft/live/gv023/00124278/00124278-201002000-00005.pdf
81. Magnusson SP, Kjaer M. Region-specific differences in Achilles tendon cross-sectional area in runners and non-runners. Eur J Appl Physiol [Internet]. Springer; 2003 [cited 2022 Apr 11];90:549–53. Available from: https://link.springer.com/article/10.1007/s00421-003-0865-8
82. Svensson RB, Heinemeier KM, Couppé C, Kjaer M, Magnusson SP. Effect of aging and exercise on the tendon. J Appl Physiol [Internet]. 2016 [cited 2018 Jul 30];121:1353–62. Available from: http://www.ncbi.nlm.nih.gov/pubmed/27150831
83. Thornton GM, Hart DA. The interface of mechanical loading and biological variables as they pertain to the development of tendinosis. J Musculoskelet Neuronal Interact. 2011;11:94–105.
84. Xu Y, Murrell GAC. The basic science of tendinopathy. Clin Orthop Relat Res. 2008;466:1528–38.
85. Cook JL, Feller JA, Bonar SF, Khan KM. Abnormal tenocyte morphology is more prevalent than collagen disruption in asymptomatic athletes' patellar tendons. J Orthop Res. 2004;22:334–8.
86. Hashimoto T, Nobuhara K, Hamada T. Pathologic Evidence of Degeneration as a Primary Cause of Rotator Cuff Tear. Clin Orthop Relat Res [Internet]. Lippincott Williams and Wilkins; 2003 [cited 2022 Jan 19];415:111–20. Available from: https://journals.lww.com/clinorthop/Fulltext/2003/10000/Pathologic_Evidence_of_Degeneration_as_a_Primary.15.aspx
87. Longo UG, Ronga M, Maffulli N. Acute ruptures of the achilles tendon. Sports Med Arthrosc. 2009;17:127–38.
88. Simon MJK, Yeoh J, Nevin J, Nimmo M, Regan WD. Histopathology of long head of biceps tendon removed during tenodesis demonstrates degenerative histopathology and not inflammatory changes. BMC Musculoskelet Disord 2022 231 [Internet]. BioMed Central; 2022 [cited 2022 Mar 2];23:1–10. Available from:

https://bmcmusculoskeletdisord.biomedcentral.com/articles/10.1186/s12891-022-05124-z
89. Cho NS, Hwang JH, Lee YT, Chae SW. Tendinosis-like histologic and molecular changes of the Achilles tendon to repetitive stress: A pilot study in rats. Clin Orthop Relat Res. 2011;469:3172–80.
90. Carpenter JE, Flanagan CL, Thomopoulos S, Yian EH, Soslowsky LJ. The effects of overuse combined with intrinsic or extrinsic alterations in an animal model of rotator cuff tendinosis. Am J Sports Med. American Orthopaedic Society for Sports Medicine; 1998;26:801–7.
91. Leadbetter WB. Cell-matrix response in tendon injury. Clin. Sports Med. 1992. p. 533–78.
92. Astrom M, Rausing A. Chronic Achilles tendinopathy: A survey of surgical and histopathologic findings. Clin Orthop Relat Res. Springer New York LLC; 1995;151–64.
93. Öhberg L, Lorentzon R, Alfredson H. Neovascularisation in Achilles tendons with painful tendinosis but not in normal tendons: An ultrasonographic investigation. Knee Surgery, Sport Traumatol Arthrosc. 2001;9:233–8.
94. Parkinson J, Samiric T, Ilic MZ, Cook J, Feller JA, Handley CJ. Change in proteoglycan metabolism is a characteristic of human patellar tendinopathy. Arthritis Rheum [Internet]. John Wiley & Sons, Ltd; 2010 [cited 2022 Apr 15];62:3028–35. Available from: https://onlinelibrary.wiley.com/doi/full/10.1002/art.27587
95. Smith MM, Sakurai G, Smith SM, Young AA, Melrose J, Stewart CM, et al. Modulation of aggrecan and ADAMTS expression in ovine tendinopathy induced by altered strain. Arthritis Rheum. 2008;58:1055–66.
96. Järvinen M, Józsa L, Kannus P, Järvinen TLN, Kvist M, Leadbetter W. Histopathological findings in chronic tendon disorders. Scand J Med Sci Sports. Wiley; 2007;7:86–95.
97. Arya S, Kulig K. Tendinopathy alters mechanical and material properties of the Achilles tendon. J Appl Physiol. 2010;108:670–5.
98. Soslowsky LJ, Thomopoulos S, Tun S, Flanagan CL, Keefer CC, Mastaw J, et al. Neer Award 1999: Overuse activity injures the supraspinatus tendon in an animal model: A histologic and biomechanical study. J Shoulder Elb Surg [Internet]. Elsevier; 2018;9:79–84. Available from: http://dx.doi.org/10.1067/mse.2000.101962
99. Shim VB, Hansen W, Newsham-West R, Nuri L, Obst S, Pizzolato C, et al. Influence of altered geometry and material properties on tissue stress distribution under load in tendinopathic Achilles tendons – a subject-specific finite element analysis. J Biomech [Internet]. Elsevier LTD; 2018; Available from: https://www.sciencedirect.com/science/article/pii/S0021929018308042?dgcid=raven_sd_aip_email
100. Kongsgaard M, Qvortrup K, Larsen J, Aagaard P, Doessing S, Hansen P, et

al. Fibril Morphology and Tendon Mechanical Properties in Patellar Tendinopathy. Am J Sports Med. 2010;38:749–56.
101. Soslowsky LJ, Thomopoulos S, Tun S, Flanagan CL, Keefer CC, Mastaw J, et al. Neer Award 1999: Overuse activity injures the supraspinatus tendon in an animal model: A histologic and biomechanical study. J Shoulder Elb Surg. Mosby; 2000;9:79–84.
102. Lui PPY, Maffulli N, Rolf C, Smith RKW. What are the validated animal models for tendinopathy? Scand J Med Sci Sport. 2011;21:3–17.
103. S. T, W.C. P, D.B. R. Mechanisms of tendon injury and repair. J Orthop Res [Internet]. 2015;33:832–9. Available from: http://www.interscience.wiley.com/jpages/0736-0266%5Cnhttp://ovidsp.ovid.com/ovidweb.cgi?T=JS&PAGE=reference&D=emed13&NEWS=N&AN=2015916370
104. Hast MW, Zuskov A, Soslowsky LJ. The role of animal models in tendon research. Bone Jt Res [Internet]. British Editorial Society of Bone and Joint Surgery; 2014 [cited 2022 Jul 12];3:193–202. Available from: https://online.boneandjoint.org.uk/doi/abs/10.1302/2046-3758.36.2000281
105. Dideriksen K, Boesen AP, Reitelseder S, Couppé C, Svensson R, Schjerling P, et al. Tendon collagen synthesis declines with immobilization in elderly humans: No effect of anti-inflammatory medication. J Appl Physiol [Internet]. American Physiological Society; 2017 [cited 2021 Nov 8];122:273–82. Available from: https://journals.physiology.org/doi/abs/10.1152/japplphysiol.00809.2015
106. Dietrich-Zagonel F, Hammerman M, Eliasson P, Aspenberg P. Response to mechanical loading in rat Achilles tendon healing is influenced by the microbiome. PLoS One [Internet]. Public Library of Science; 2020 [cited 2021 Nov 8];15. Available from: /pmc/articles/PMC7064237/
107. Eliasson P, Andersson T, Aspenberg P. Rat Achilles tendon healing: Mechanical loading and gene expression. J Appl Physiol [Internet]. American Physiological Society; 2009 [cited 2021 Nov 8];107:399–407. Available from: https://journals.physiology.org/doi/abs/10.1152/japplphysiol.91563.2008
108. Killian ML, Lim CT, Thomopoulos S, Charlton N, Kim HM, Galatz LM. The effect of unloading on gene expression of healthy and injured rotator cuffs. J Orthop Res [Internet]. John Wiley & Sons, Ltd; 2013 [cited 2021 Nov 11];31:1240–8. Available from: https://onlinelibrary.wiley.com/doi/full/10.1002/jor.22345
109. Oshima J, Sasaki K, Yamamoto N, Kiyosawa T, Sekido M. Visualization of microstructural change affected by mechanical stimulation in tendon healing with a novel tensionless model. Microscopy [Internet]. Oxford Academic; 2021 [cited 2022 Jan 19];70:186–91. Available from: https://academic.oup.com/jmicro/article/70/2/186/5879807
110. Khayyeri H, Hammerman M, Turunen MJ, Blomgran P, Notermans T,

Guizar-Sicairos M, et al. Diminishing effects of mechanical loading over time during rat Achilles tendon healing. PLoS One [Internet]. Public Library of Science; 2020 [cited 2021 Nov 8];15. Available from: /pmc/articles/PMC7735574/
111. Johnson RB. The bearable lightness of being: Bones, muscles, and spaceflight. Anat Rec. 1998;253:24–7.
112. Dirks RC, Warden SJ. Models for the study of tendinopathy. J. Musculoskelet. Neuronal Interact. 2011. p. 141–9.
113. Archambault JM, Hart DA, Herzog W. Response of rabbit achilles tendon to chronic repetitive loading. Connect Tissue Res. 2001;42:13–23.
114. Warden SJ. Animal models for the study of tendinopathy. BrJSports Med. 2007;41:232–40.
115. Fung DT, Wang VM, Andarawis-Puri N, Basta-Pljakic J, Li Y, Laudier DM, et al. Early response to tendon fatigue damage accumulation in a novel in vivo model. J Biomech. 2010;43:274–9.
116. Andarawis-Puri N, Sereysky JB, Sun HB, Jepsen KJ, Flatow EL. Molecular response of the patellar tendon to fatigue loading explained in the context of the initial induced damage and number of fatigue loading cycles. J Orthop Res. 2012;30:1327–34.
117. Andarawis-Puri N, Philip A, Laudier D, Schaffler MB, Flatow EL. Temporal Effect of In Vivo Tendon Fatigue Loading on the Apoptotic Response Explained in the Context of Number of Fatigue Loading Cycles and Initial Damage Parameters. J Orthop Res [Internet]. NIH Public Access; 2014 [cited 2021 Nov 8];32:1097. Available from: /pmc/articles/PMC4209741/
118. Sereysky JB, Andarawis-Puri N, Jepsen KJ, Flatow EL. Structural and mechanical effects of in vivo fatigue damage induction on murine tendon. J Orthop Res. 2012;30:965–72.
119. Michna H, Hartmann G. Adaptation of tendon collagen to exercise. Int Orthop [Internet]. 1989 [cited 2019 Nov 30];13:161–5. Available from: http://www.ncbi.nlm.nih.gov/pubmed/2633778
120. Heinemeier KM, Skovgaard D, Bayer ML, Qvortrup K, Kjaer A, Kjaer M, et al. Uphill running improves rat Achilles tendon tissue mechanical properties and alters gene expression without inducing pathological changes. J Appl Physiol [Internet]. American Physiological Society Bethesda, MD; 2012 [cited 2021 Nov 9];113:827–36. Available from: https://journals.physiology.org/doi/abs/10.1152/japplphysiol.00401.2012
121. Carpenter JE, Flanagan CL, Thomopoulos S, Yian EH, Soslowsky LJ. The effects of overuse combined with intrinsic or extrinsic alterations in an animal model of rotator cuff tendinosis. Am J Sports Med [Internet]. American Orthopaedic Society for Sports Medicine; 1998 [cited 2022 Apr 15];26:801–7. Available from: https://journals.sagepub.com/doi/10.1177/03635465980260061101?url_ver=Z39.88-2003&rfr_id=ori%3Arid%3Acrossref.org&rfr_dat=cr_pub++0pubmed

122. K.A. R, A.M. P, B.R. F, L.J. S. Supraspinatus tendons have different mechanical properties across sex. J Orthop Res [Internet]. 2017;35. Available from: http://www.embase.com/search/results?subaction=viewrecord&from=export&id=L616815925%0Ahttp://rug.on.worldcat.org/atoztitles/link/?sid=EMBASE&issn=1554527X&id=doi:&atitle=Supraspinatus+tendons+have+different+mechanical+properties+across+sex&stitle=J.+Ortho
123. Brown DA, Johnson MS, Armstrong CJ, Lynch JM, Caruso NM, Ehlers LB, et al. Short-term treadmill running in the rat: What kind of stressor is it? J Appl Physiol [Internet]. American Physiological Society; 2007 [cited 2020 Dec 9];103:1979–85. Available from: http://www.jap.org
124. Xu SY, He Y Bin, Deng SY, Liu SY, Xu L, Ni GX. Intensity-dependent effect of treadmill running on rat Achilles tendon. Exp Ther Med [Internet]. Spandidos Publications; 2018 [cited 2022 Jan 17];15:5377. Available from: /pmc/articles/PMC5958711/
125. Kirby TJ, McCarthy JJ, Peterson CA, Fry CS. Synergist ablation as a rodent model to study satellite cell dynamics in adult skeletal muscle. Methods Mol Biol. Humana Press Inc.; 2016;1460:43–52.
126. Fry CS, Lee JD, Jackson JR, Kirby TJ, Stasko SA, Liu H, et al. Regulation of the muscle fiber microenvironment by activated satellite cells during hypertrophy. FASEB J. FASEB; 2014;28:1654–65.
127. Terena SML, Fernandes KPS, Bussadori SK, Deana AM, Mesquita-Ferrari RA. Systematic review of the synergist muscle ablation model for compensatory hypertrophy. Rev. Assoc. Med. Bras. Associacao Medica Brasileira; 2017. p. 164–72.
128. Pérez-Schindler J, Summermatter S, Santos G, Zorzato F, Handschin C. The transcriptional coactivator PGC-1α is dispensable for chronic overload-induced skeletal muscle hypertrophy and metabolic remodeling. Proc Natl Acad Sci U S A. 2013;110:20314–9.
129. Mendias CL, Schwartz AJ, Grekin JA, Gumucio JP, Sugg KB. Changes in muscle fiber contractility and extracellular matrix production during skeletal muscle hypertrophy. J Appl Physiol [Internet]. 2017;122:571 LP – 579. Available from: http://jap.physiology.org/content/122/3/571.abstract
130. Zamora a J, Marini JF. Tendon and myo-tendinous junction in an overloaded skeletal muscle of the rat. Anat Embryol [Internet]. 1988;179:89–96. Available from: http://www.ncbi.nlm.nih.gov/entrez/query.fcgi?cmd=Retrieve&db=PubMed&dopt=Citation&list_uids=3213959
131. Goodman CA, Mabrey DM, Frey JW, Miu MH, Schmidt EK, Pierre P, et al. Novel insights into the regulation of skeletal muscle protein synthesis as revealed by a new nonradioactive in vivo technique. FASEB J. 2011;25:1028–39.
132. Flood MD, Phan AC, Gumucio JP, Mendias CL. Achilles Tendon Ablation

Induces Scleraxis Expression and Neotendon Formation in the Plantaris Tendon. FASEB J [Internet]. 2012;26:1142.52-1142.52. Available from: http://www.fasebj.org/content/26/1_Supplement/1142.52.abstract

133. Gumucio JP, Phan AC, Ruehlmann DG, Noah AC, Mendias CL. Synergist ablation induces rapid tendon growth through the synthesis of a neotendon matrix. J Appl Physiol [Internet]. 2014;117:1287–91. Available from: http://jap.physiology.org/cgi/doi/10.1152/japplphysiol.00720.2014

134. Schwartz AJ, Sarver DC, Sugg KB, Dzierzawski JT, Gumucio JP, Mendias CL. P38 MAPK signaling in postnatal tendon growth and remodeling. PLoS One. 2015;10:1–21.

135. Olesen JL, Heinemeier KM, Haddad F, Langberg H, Flyvbjerg A, Kjær M, et al. Expression of insulin-like growth factor I, insulin-like growth factor binding proteins, and collagen mRNA in mechanically loaded plantaris tendon. J Appl Physiol [Internet]. American Physiological Society; 2006 [cited 2021 Nov 11];101:183–8. Available from: https://journals.physiology.org/doi/abs/10.1152/japplphysiol.00636.2005

136. Han WM, Heo SJ, Driscoll TP, Delucca JF, McLeod CM, Smith LJ, et al. Microstructural heterogeneity directs micromechanics and mechanobiology in native and engineered fibrocartilage. Nat Mater. Nature Publishing Group; 2016;15:477–84.

137. Screen HRC, Shelton JC, Chhaya VH, Kayser M V., Bader DL, Lee DA. The influence of noncollagenous matrix components on the micromechanical environment of tendon fascicles. Ann Biomed Eng. 2005;33:1090–9.

138. Andrews SHJ, Rattner JB, Shrive NG, Ronsky JL. Swelling significantly affects the material properties of the menisci in compression. J Biomech [Internet]. Elsevier; 2015 [cited 2019 Jul 12];48:1485–9. Available from: https://www.sciencedirect.com/science/article/pii/S0021929015000676

139. Chimich D, Shrive N, Frank C, Marchuk L, Bray R. Water content alters viscoelastic behaviour of the normal adolescent rabbit medial collateral ligament. J Biomech [Internet]. Elsevier; 1992 [cited 2019 Jul 19];25:831–7. Available from: https://www.sciencedirect.com/science/article/pii/002192909290223N

140. Han WM, Nerurkar NL, Smith LJ, Jacobs NT, Mauck RL, Elliott DM. Multi-scale Structural and Tensile Mechanical Response of Annulus Fibrosus to Osmotic Loading. Ann Biomed Eng [Internet]. Springer US; 2012 [cited 2018 May 16];40:1610–21. Available from: http://link.springer.com/10.1007/s10439-012-0525-4

141. Baylon EG, Levenston ME. Title Page Osmotic Swelling Responses are Conserved Across Cartilaginous Tissues with Varied Sulfated-Glycosaminoglycan Contents. 2018 [cited 2019 Jul 15]; Available from: http://dx.doi.org/10.1101/459115

142. Eisenberg SR, Grodzinsky AJ. Swelling of Articular Cartilage and Other Connective Tissues: Electrornechanochemical Forces [Internet]. Available

from: https://onlinelibrary.wiley.com/doi/pdf/10.1002/jor.1100030204
143. Hannafin JA, Arnoczky SP. Effect of cyclic and static tensile loading on water content and solute diffusion in canine flexor tendons: Anin Vitro study. J Orthop Res [Internet]. John Wiley & Sons, Ltd; 1994 [cited 2019 Jul 15];12:350–6. Available from: http://doi.wiley.com/10.1002/jor.1100120307
144. O Hara BP, G Urban JP, Maroudas A. Influence of cyclic loading on the nutrition of articular cartilage. Ann ofthe Rheum Dis [Internet]. 1990 [cited 2019 Jul 15];49:536–9. Available from: http://ard.bmj.com/
145. Travascio F, Jackson AR, Brown MD, Gu WY. Relationship between solute transport properties and tissue morphology in human annulus fibrosus. J Orthop Res [Internet]. John Wiley & Sons, Ltd; 2009 [cited 2019 Jul 15];27:1625–30. Available from: http://doi.wiley.com/10.1002/jor.20927
146. Safa BN, Meadows KD, Szczesny SE, Elliott DM. Exposure to buffer solution alters tendon hydration and mechanics. 2017 [cited 2018 Apr 15]; Available from: http://www.jbiomech.com/article/S0021-9290(17)30355-X/pdf
147. Katz EP, Li ST. The intermolecular space of reconstituted collagen fibrils. J Mol Biol [Internet]. Academic Press; 1973 [cited 2019 Jul 15];73:351–69. Available from: https://www.sciencedirect.com/science/article/pii/0022283673903471
148. Sverdlik A, Lanir Y. Time-Dependent Mechanical Behavior of Sheep Digital Tendons, Including the Effects of Preconditioning. J Biomech Eng [Internet]. American Society of Mechanical Engineers; 2002 [cited 2019 Jul 15];124:78. Available from: http://biomechanical.asmedigitalcollection.asme.org/article.aspx?articleid=1407347
149. Parsegian VA, Rand RP, Fuller NL, Rau DC. [29] Osmotic stress for the direct measurement of intermolecular forces. Methods Enzymol [Internet]. Academic Press; 1986 [cited 2019 Jul 15];127:400–16. Available from: https://www.sciencedirect.com/science/article/pii/0076687986270329
150. Shahmirzadi D, Hsieh AH. An efficient technique for adjusting and maintaining specific hydration levels in soft biological tissues in vitro. Med Eng Phys [Internet]. Elsevier; 2010 [cited 2019 Jul 15];32:795–801. Available from: https://www.sciencedirect.com/science/article/pii/S1350453310000950
151. Steuter AA, Mozafar A, Goodin JR. Water potential of aqueous polyethylene glycol. Plant Physiol [Internet]. American Society of Plant Biologists; 1981 [cited 2019 Jul 15];67:64–7. Available from: http://www.ncbi.nlm.nih.gov/pubmed/16661635
152. Screen HRC, Chhaya VH, Greenwald SE, Bader DL, Lee DA, Shelton JC. The influence of swelling and matrix degradation on the microstructural integrity of tendon. Acta Biomater [Internet]. Elsevier; 2006 [cited 2018 May 16];2:505–13. Available from: https://www.sciencedirect.com/science/article/pii/S1742706106000638

153. KarisAllen JJ, Veres SP. Effect of testing temperature on the nanostructural response of tendon to tensile mechanical overload. J Biomech [Internet]. Elsevier; 2020 [cited 2020 Mar 7];109720. Available from: https://linkinghub.elsevier.com/retrieve/pii/S0021929020301366
154. Muench JR, Thelen DG, Henak CR. Interfibrillar shear behavior is altered in aging tendon fascicles. Biomech Model Mechanobiol [Internet]. [cited 2020 Jan 6]; Available from: https://doi.org/10.1007/s10237-019-01251-0
155. Leikin S, Parsegian VA, Yang W-H, Walrafen GE. Raman spectral evidence for hydration forces between collagen triple helices. Proc Natl Acad Sci [Internet]. 1997 [cited 2020 May 26];94:11312–7. Available from: http://www.pnas.org/cgi/doi/10.1073/pnas.94.21.11312
156. Li Y, Douglas EP. Effects of various salts on structural polymorphism of reconstituted type I collagen fibrils. Colloids Surfaces B Biointerfaces [Internet]. 2013 [cited 2020 May 26];112:42–50. Available from: https://linkinghub.elsevier.com/retrieve/pii/S0927776513004736
157. Lozano PF, Scholze M, Babian C, Scheidt H, Vielmuth F, Waschke J, et al. Water-content related alterations in macro and micro scale tendon biomechanics. Sci Rep [Internet]. Nature Publishing Group; 2019 [cited 2019 Jul 19];9:7887. Available from: http://www.nature.com/articles/s41598-019-44306-z
158. Michna H. Morphometric analysis of loading-induced changes in collagen-fibril populations in young tendons. Cell Tissue Res. 1984;236:465–70.
159. Goulam Houssen Y, Gusachenko I, Schanne-Klein MC, Allain JM. Monitoring micrometer-scale collagen organization in rat-tail tendon upon mechanical strain using second harmonic microscopy. J Biomech [Internet]. Elsevier; 2011;44:2047–52. Available from: http://dx.doi.org/10.1016/j.jbiomech.2011.05.009
160. Sivaguru M, Durgam S, Ambekar R, Luedtke D, Fried G, Stewart A, et al. Quantitative analysis of collagen fiber organization in injured tendons using Fourier transform-second harmonic generation imaging. Opt Express [Internet]. 2010 [cited 2019 Nov 30];18:24983–93. Available from: http://www.ncbi.nlm.nih.gov/pubmed/21164843
161. Birk DE, Zycband EI, Winkelmann DA, Trelstad RL. Collagen fibrillogenesis in situ: fibril segments are intermediates in matrix assembly. Proc Natl Acad Sci U S A [Internet]. National Academy of Sciences; 1989 [cited 2023 Jan 8];86:4549. Available from: /pmc/articles/PMC287308/?report=abstract
162. Starborg T, Kalson NS, Lu Y, Mironov A, Cootes TF, Holmes DF, et al. Using transmission electron microscopy and 3View to determine collagen fibril size and three-dimensional organization. Nat Protoc [Internet]. 2013;8:1433–48. Available from: http://www.nature.com/doifinder/10.1038/nprot.2013.086
163. Raymond-Hayling H, Lu Y, Kadler KE, Shearer T. A fibre tracking algorithm for volumetric microstructural data - application to tendons. Acta Biomater.

Elsevier; 2022;154:335–48.
164. Takahashi N, Kametani K, Ota R, Prasarn Tangkawattana |, Iwasaki T, Hasegawa Y, et al. Three-dimensional ultrastructure reconstruction of tendinous components at the bifurcation of the bovine superficial digital flexor tendon using array and STEM tomographies. J Anat. 2020;00:1–10.
165. Kalson NS, Starborg T, Lu Y, Mironov A, Humphries SM, Holmes DF, et al. Nonmuscle myosin II powered transport of newly formed collagen fibrils at the plasma membrane. Proc Natl Acad Sci U S A [Internet]. National Academy of Sciences; 2013;110:E4743--52. Available from: http://www.ncbi.nlm.nih.gov/pubmed/284347
166. Kalson NS, Lu Y, Taylor SH, Starborg T, Holmes DF, Kadler KE. A structure-based extracellular matrix expansion mechanism of fibrous tissue growth. Elife [Internet]. 2015;4. Available from: http://www.ncbi.nlm.nih.gov/pubmed/25992598
167. Hadate S, Takahashi N, Kametani K, Iwasaki T, Hasega Y, Tangkawattana P, et al. Ultrastructural study of the three-dimensional tenocyte network in newly hatched chick Achilles tendons using serial block face-scanning electron microscopy.
168. Ronneberger O, Fischer P, Brox T. U-net: Convolutional networks for biomedical image segmentation. Lect Notes Comput Sci (including Subser Lect Notes Artif Intell Lect Notes Bioinformatics) [Internet]. Springer Verlag; 2015 [cited 2021 Feb 2]. p. 234–41. Available from: http://lmb.informatik.uni-freiburg.de/http://lmb.informatik.uni-freiburg.de/people/ronneber/u-net.
169. Hua Y, Laserstein P, Helmstaedter M. Large-volume en-bloc staining for electron microscopy-based connectomics. Nat Commun [Internet]. Nature Publishing Group; 2015 [cited 2020 Dec 23];6. Available from: https://pubmed.ncbi.nlm.nih.gov/26235643/
170. Schindelin J, Arganda-Carreras I, Frise E, Kaynig V, Longair M, Pietzsch T, et al. Fiji: an open-source platform for biological-image analysis. Nat Methods 2012 97 [Internet]. Nature Publishing Group; 2012 [cited 2022 Nov 27];9:676–82. Available from: https://www.nature.com/articles/nmeth.2019
171. Otsu N. THRESHOLD SELECTION METHOD FROM GRAY-LEVEL HISTOGRAMS. IEEE Trans Syst Man Cybern. 1979;SMC-9:62–6.
172. CIBC. Seg3D: Volumetric Image Segmentation and Visualization. Scientific Computing and Imaging Institute (SCI), Download from: http://www.seg3d.org. 2016.
173. Safa BN, Peloquin JM, Natriello JR, Caplan JL, Elliott DM. 3D Microstructure of Tendon Collagen Fibrils using Serial Block-Face SEM and a Mechanical Model for Load Transfer. bioRxiv [Internet]. Cold Spring Harbor Laboratory; 2019 [cited 2019 Nov 30];547281. Available from: https://www.biorxiv.org/content/10.1101/547281v1
174. Sein ML, Walton J, Linklater J, Appleyard R, Kirkbride B, Kuah D, et al.

Shoulder pain in elite swimmers: primarily due to swim-volume-induced supraspinatus tendinopathy. Br J Sports Med [Internet]. British Association of Sport and Excercise Medicine; 2010 [cited 2022 Apr 15];44:105–13. Available from: https://bjsm.bmj.com/content/44/2/105

175. Hopkins C, Fu SC, Chua E, Hu X, Rolf C, Mattila VM, et al. Critical review on the socio-economic impact of tendinopathy. Asia-Pacific J Sport Med Arthrosc Rehabil Technol [Internet]. Elsevier Ltd; 2016;4:9–20. Available from: http://dx.doi.org/10.1016/j.asmart.2016.01.002

176. Auerbach JD, Weidner ZD, Milby AH, Diab M, Lonner BS. Musculoskeletal disorders among spine surgeons: Results of a survey of the scoliosis research society membership. Spine (Phila Pa 1976) [Internet]. 2011 [cited 2022 Apr 15];36. Available from: https://journals.lww.com/spinejournal/Fulltext/2011/12150/Musculoskeletal_Disorders_Among_Spine_Surgeons_.27.aspx

177. Kannus P, Natri A. Etiology and pathophysiology of tendon ruptures in sports. Scand J Med Sci Sports [Internet]. John Wiley & Sons, Ltd; 1997 [cited 2022 Apr 15];7:107–12. Available from: https://onlinelibrary.wiley.com/doi/full/10.1111/j.1600-0838.1997.tb00126.x

178. Longo UG, Rittweger J, Garau G, Radonic B, Gutwasser C, Gilliver SF, et al. No influence of age, gender, weight, height, and impact profile in achilles tendinopathy in masters track and field athletes. Am J Sports Med. SAGE Publications Inc.; 2009;37:1400–5.

179. Nyyssöen T, Lüthje P. Achilles tendon ruptures in South-East Finland between 1986-1996, with special reference to epidemiology, complications of surgery and hospital costs [Internet]. Scand. J. Surg. 2000 [cited 2022 Apr 15]. p. 53–7. Available from: https://www.researchgate.net/publication/12525019_Achilles_tendon_ruptures_in_South-East_Finland_between_1986-1996_with_special_reference_to_epidemiology_complications_of_surgery_and_hospital_costs

180. Maffulli N, Longo UG, Maffulli GD, Rabitti C, Khanna A, Denaro V. Marked pathological changes proximal and distal to the site of rupture in acute Achilles tendon ruptures. Knee Surgery, Sport Traumatol Arthrosc [Internet]. Springer; 2011 [cited 2022 Mar 8];19:680–7. Available from: https://link.springer.com/article/10.1007/s00167-010-1193-2

181. Tallon C, Maffulli N, Ewen SWB. Ruptured Achilles tendons are significantly more degenerated than tendinopathic tendons. Med Sci Sports Exerc. 2001;33:1983–90.

182. Kannus P, Jozsa L. Histopathological changes preceding spontaneous rupture of a tendon. A controlled study of 891 patients. J Bone Joint Surg Am. United States; 1991;73:1507–25.

183. Williamson PM, Freedman BR, Kwok N, Beeram I, Pennings J, Johnson J, et al. Tendinopathy and tendon material response to load: What can we learn

from small Animal studies. Acta Biomater [Internet]. NIH Public Access; 2021 [cited 2022 Jun 17];134:43. Available from: /pmc/articles/PMC8542586/

184. Huang T-F, Perry SM, Soslowsky LJ. The Effect of Overuse Activity on Achilles Tendon in an Animal Model: A Biomechanical Study. Ann. Biomed. Eng. 2004.
185. Sommer HM. The biomechanical and metabolic effects of a running regime on the Achilles tendon in the rat. Int Orthop [Internet]. Int Orthop; 1987 [cited 2022 Apr 11];11:71–5. Available from: https://pubmed.ncbi.nlm.nih.gov/3557758/
186. Thampatty BP, Wang JHC. Mechanobiology of young and aging tendons: In vivo studies with treadmill running. J Orthop Res. 2017;1–9.
187. Patterson-Kane JC, Wilson AM, Firth EC, Parry' DAD, Goodshipt AE. Comparison of collagen fibril populations in the superficial digital flexor tendons of exercised and nonexercised Thoroughbreds. EQUINE Vet. J. Equine vet. J. 1997.
188. Patterson-Kane JC, Parry DAD, Birch HL, Goodship AE, Firth EC. An Age-Related Study of Morphology and Cross-Link Composition of Collagen Fibrils in the Digital Flexor Tendons of Young Thoroughbred Horses. http://dx.doi.org/103109/03008209709160225 [Internet]. Taylor & Francis; 2009 [cited 2022 Feb 25];36:253–60. Available from: https://www.tandfonline.com/doi/abs/10.3109/03008209709160225
189. Bank RA, Tekoppele JM, Oostingh G, Hazleman BL, Riley GP. Lysylhydroxylation and non-reducible crosslinking of human supraspinatus tendon collagen: changes with age and in chronic rotator cuff tendinitis. Ann Rheum Dis [Internet]. BMJ Publishing Group; 1999 [cited 2022 Jan 19];58:35. Available from: /pmc/articles/PMC1752756/
190. Riley GP, Harrall H, Constant CR, Chard MD, Cawston TE, Hazleman BL. Tendon degeneration and chronic shoulder pain: changes in the collagen composition of the human rotator cuff tendons in rotator cuff tendinitis. Ann Rheum Dis [Internet]. BMJ Publishing Group; 1994 [cited 2022 Jan 19];53:359. Available from: /pmc/articles/PMC1005350/?report=abstract
191. Corps AN, Robinson AHN, Movin T, Costa ML, Hazleman BL, Riley GP. Increased expression of aggrecan and biglycan mRNA in Achilles tendinopathy. Rheumatology. 2006;45:291–4.
192. Bell R, Gendron R, Brenneman J, Flatow EL, Andarawis-puri N. STRUCTURAL REMODELING OF FATIGUE DAMAGED TENDONS BY EXERCISE IS ASSOCIATED WITH INTEGRIN SUBUNITS α V AND α 5. 2017;24–5.
193. Abraham AC, Fang F, Golman M, Oikonomou P, Thomopoulos S. The role of loading in murine models of rotator cuff disease. J Orthop Res [Internet]. John Wiley & Sons, Ltd; 2022 [cited 2022 Apr 8];40:977–86. Available from: https://onlinelibrary.wiley.com/doi/full/10.1002/jor.25113

194. Freedman BR, Rodriguez AB, Leiphart RJ, Newton JB, Ban E, Sarver JJ, et al. Dynamic Loading and Tendon Healing Affect Multiscale Tendon Properties and ECM Stress Transmission. Sci Rep [Internet]. Nature Publishing Group; 2018 [cited 2018 Jul 31];8:10854. Available from: http://www.nature.com/articles/s41598-018-29060-y
195. Loppini M, Longo U, Niccoli G, Khan W, Maffulli N, Denaro V. Histopathological Scores for Tissue-Engineered, Repaired and Degenerated Tendon: A Systematic Review of the Literature. Curr Stem Cell Res Ther. Bentham Science Publishers Ltd.; 2014;10:43–55.
196. Esser KA, White TP. Mechanical load affects growth and maturation of skeletal muscle grafts. J Appl Physiol. 1995;78:30–7.
197. Kirby TJ, Mccarthy JJ, Peterson CA, Fry CS. Skeletal Muscle Regeneration in the Mouse. 2016;1460:43–52. Available from: http://link.springer.com/10.1007/978-1-4939-3810-0
198. Astrom M, Rausing A. Chronic Achilles Tendinopathy. Clin Orthop Relat Res [Internet]. 1995;151–64. Available from: http://www.ncbi.nlm.nih.gov/pubmed/7634699
199. Killian ML, Cavinatto LM, Ward SR, Havlioglu N, Thomopoulos S, Galatz LM. Chronic Degeneration Leads to Poor Healing of Repaired Massive Rotator Cuff Tears in Rats. Am J Sports Med [Internet]. NIH Public Access; 2015 [cited 2022 Jan 19];43:2401. Available from: /pmc/articles/PMC4750378/
200. Backman C, Boquist L, Fridén J, Lorentzon R, Toolanen G. Chronic achilles paratenonitis with tendinosis: An experimental model in the rabbit. J Orthop Res [Internet]. John Wiley & Sons, Ltd; 1990 [cited 2022 Jan 19];8:541–7. Available from: https://onlinelibrary.wiley.com/doi/full/10.1002/jor.1100080410
201. Järvinen M, Józsa L, Kannus P, Järvinen TLN, Kvist M, Leadbetter W. Histopathological findings in chronic tendon disorders. Scand J Med Sci Sports [Internet]. 2007;7:86–95. Available from: http://doi.wiley.com/10.1111/j.1600-0838.1997.tb00124.x
202. Zhu M, Musson D, Oliver M, Firth E, Cornish J, Munro J. Modelling gluteus medius tendon degeneration and repair in a large animal model. Arch Orthop Trauma Surg [Internet]. Springer; 2020 [cited 2020 Oct 24];1:3. Available from: https://doi.org/10.1007/s00402-020-03573-6
203. Yushkevich PA, Piven J, Hazlett HC, Smith RG, Ho S, Gee JC, et al. User-guided 3D active contour segmentation of anatomical structures: Significantly improved efficiency and reliability. Neuroimage [Internet]. Neuroimage; 2006 [cited 2021 Feb 3];31:1116–28. Available from: https://pubmed.ncbi.nlm.nih.gov/16545965/
204. Lemmon EA, Locke RC, Szostek AK, Ganji E, Killian ML. Partial-width injuries of the rat rotator cuff heal with fibrosis. Connect Tissue Res [Internet]. NIH Public Access; 2018 [cited 2022 Apr 18];59:437. Available

from: /pmc/articles/PMC6324170/
205. Locke RC, Lemmon EA, Dudzinski E, Kopa SC, Wayne JM, Soulas JM, et al. Photobiomodulation does not influence maturation and mildly improves functional healing of mouse achilles tendons. J Orthop Res. 2020;38:1866–75.
206. Lee AH, Elliott DM. Comparative multi-scale hierarchical structure of the tail, plantaris, and Achilles tendons in the rat. J Anat [Internet]. Wiley-Blackwell; 2019 [cited 2021 Nov 10];234:252. Available from: /pmc/articles/PMC6326909/
207. Bloom ET, Lee AH, Elliott DM. Tendon Multiscale Structure, Mechanics, and Damage Are Affected by Osmolarity of Bath Solution. Ann Biomed Eng [Internet]. Springer; 2020 [cited 2020 Nov 11];1–11. Available from: https://doi.org/10.1007/s10439-020-02649-z
208. Han WM, Heo SJ, Driscoll TP, Smith LJ, Mauck RL, Elliott DM. Macro- to microscale strain transfer in fibrous tissues is heterogeneous and tissue-specific. Biophys J. 2013;105:807–17.
209. Rigozzi S, Mü Ller R, Snedeker JG. Collagen fibril morphology and mechanical properties of the Achilles tendon in two inbred mouse strains. [cited 2022 Nov 8]; Available from: https://onlinelibrary.wiley.com/doi/10.1111/j.1469-7580.2010.01225.x
210. Derwin KA, Soslowsky LJ. A Quantitative Investigation of Structure-Function Relationships in a Tendon Fascicle Model. J Biomech Eng [Internet]. American Society of Mechanical Engineers Digital Collection; 1999 [cited 2022 Nov 8];121:598–604. Available from: https://asmedigitalcollection.asme.org/biomechanical/article/121/6/598/398709/A-Quantitative-Investigation-of-Structure-Function
211. Rosager S, Aagaard P, Dyhre-Poulsen P, Neergaard K, Kjaer M, Magnusson SP. Load-displacement properties of the human triceps surae aponeurosis and tendon in runners and non-runners. Scand J Med Sci Sports [Internet]. John Wiley & Sons, Ltd; 2002 [cited 2022 Apr 11];12:90–8. Available from: https://onlinelibrary.wiley.com/doi/full/10.1034/j.1600-0838.2002.120205.x
212. Abraham T, Fong G, Scott A. Second harmonic generation analysis of early Achilles tendinosis in response to in vivo mechanical loading. BMC Musculoskelet Disord [Internet]. BioMed Central; 2011 [cited 2022 Nov 8];12:26. Available from: /pmc/articles/PMC3045393/
213. Glazebrook MA, Wright JR, Langman M, Stanish WD, Lee JM. Histological analysis of achilles tendons in an overuse rat model. J Orthop Res [Internet]. John Wiley & Sons, Ltd; 2008 [cited 2022 Jan 17];26:840–6. Available from: https://onlinelibrary.wiley.com/doi/full/10.1002/jor.20546
214. Fung DT, Sereysky JB, Basta-Pljakic J, Laudier DM, Huq R, Jepsen KJ, et al. Second harmonic generation imaging and fourier transform spectral analysis reveal damage in fatigue-loaded tendons. Ann Biomed Eng. 2010;38:1741–51.
215. Józsa L, Lehto M, Kvist M, Bálint JB, Reffy A. Alterations in Dry Mass

Content of Collagen Fibers in Degenerative Tendinopathy and Tendon-Rupture. Matrix. 1989;9:140–6.
216. Dirks RC, Richard JS, Fearon AM, Scott A, Koch LG, Britton SL, et al. Uphill treadmill running does not induce histopathological changes in the rat Achilles tendon. BMC Musculoskelet Disord [Internet]. BioMed Central; 2013 [cited 2022 Apr 15];14:1–5. Available from: https://bmcmusculoskeletdisord.biomedcentral.com/articles/10.1186/1471-2474-14-90
217. Ellis I, Schnabel L V., Berglund AK. Defining the profile: Characterizing cytokines in tendon injury to improve clinical therapy. J Immunol Regen Med [Internet]. 2022 [cited 2022 Mar 7];100059. Available from: https://linkinghub.elsevier.com/retrieve/pii/S2468498822000014
218. Chisari E, Rehak L, Khan WS, Maffulli N. Tendon healing in presence of chronic low-level inflammation: a systematic review. [cited 2020 Sep 2]; Available from: https://academic.oup.com/bmb/article/132/1/97/5678072
219. Millar NL, Silbernagel KG, Thorborg K, Kirwan PD, Galatz LM, Abrams GD, et al. Tendinopathy. Nat Rev Dis Prim 2021 71 [Internet]. Nature Publishing Group; 2021 [cited 2022 Nov 26];7:1–21. Available from: https://www.nature.com/articles/s41572-020-00234-1
220. Woodley BL, Newsham-West RJ, Baxter GD. Chronic tendinopathy: effectiveness of eccentric exercise. Br J Sports Med [Internet]. BMJ Publishing Group; 2007 [cited 2022 Nov 26];41:188. Available from: /pmc/articles/PMC2658941/
221. Dimitrios S. Exercise for tendinopathy. World J Methodol [Internet]. Baishideng Publishing Group Inc; 2015 [cited 2022 Nov 26];5:51. Available from: /pmc/articles/PMC4482821/
222. Hae Yoon J, Brooks R, Hwan Kim Y, Terada M, Halper J. Proteoglycans in chicken gastrocnemius tendons change with exercise. Arch Biochem Biophys. Academic Press; 2003;412:279–86.
223. Pang X, Wu JP, Allison GT, Xu J, Rubenson J, Zheng MH, et al. Three dimensional microstructural network of elastin, collagen, and cells in Achilles tendons. J Orthop Res. 2017;35:1203–14.
224. Hammer N, Huster D, Fritsch S, Hä drich C, Koch H, Schmidt P, et al. Do Cells Contribute to Tendon and Ligament Biomechanics? [cited 2022 Nov 26]; Available from: www.plosone.org
225. Siadat SM, Zamboulis DE, Thorpe CT, Ruberti JW, Connizzo BK. Tendon Extracellular Matrix Assembly, Maintenance and Dysregulation Throughout Life. Adv Exp Med Biol [Internet]. Springer, Cham; 2021 [cited 2021 Nov 29];1348:45–103. Available from: https://link.springer.com/chapter/10.1007/978-3-030-80614-9_3
226. Gardner K, Lavagnino M, Egerbacher M, Arnoczky SP. Re-establishment of cytoskeletal tensional homeostasis in lax tendons occurs through an actin-mediated cellular contraction of the extracellular matrix. J Orthop Res.

2012;30:1695–701.
227. Inguito KL, Schofield MM, Faghri AD, Bloom ET, Heino M, West VC, et al. Stress Deprivation of Tendon Explants or Tpm3.1 Inhibition in Tendon Cells Reduces F-actin to Promote a Tendinosis-like Phenotype.
228. Watanabe T, Imamura Y, Hosaka Y, Ueda H, Takehana K. Graded Arrangement of Collagen Fibrils in the Equine Superficial Digital Flexor Tendon. http://dx.doi.org/101080/03008200701692800 [Internet]. Taylor & Francis; 2009 [cited 2022 Nov 26];48:332–7. Available from: https://www.tandfonline.com/doi/abs/10.1080/03008200701692800
229. De Mos M, Koevoet W, Van Schie HTM, Kops N, Jahr H, Verhaar JAN, et al. In vitro model to study chondrogenic differentiation in tendinopathy. Am J Sports Med [Internet]. Am J Sports Med; 2009 [cited 2022 Nov 26];37:1214–22. Available from: https://pubmed.ncbi.nlm.nih.gov/19279223/
230. Szczesny SE, Aeppli C, David A, Mauck RL. Fatigue Loading of Tendon Results in Collagen Kinking and Denaturation but Does Not Change Local Tissue Mechanics. J Biomech [Internet]. 2018; Available from: http://linkinghub.elsevier.com/retrieve/pii/S0021929018301118
231. Thorpe CT, Godinho MSC, Riley GP, Birch HL, Clegg PD, Screen HRC. The interfascicular matrix enables fascicle sliding and recovery in tendon, and behaves more elastically in energy storing tendons. J Mech Behav Biomed Mater [Internet]. 2015 [cited 2018 Jul 31];52:85–94. Available from: http://www.ncbi.nlm.nih.gov/pubmed/25958330
232. Thorpe CT, Klemt C, Riley GP, Birch HL, Clegg PD, Screen HRC. Helical sub-structures in energy-storing tendons provide a possible mechanism for efficient energy storage and return. Acta Biomater [Internet]. Acta Materialia Inc.; 2013;9:7948–56. Available from: http://dx.doi.org/10.1016/j.actbio.2013.05.004
233. Thorpe CT, Udeze CP, Birch HL, Clegg PD, Screen HRC. Specialization of tendon mechanical properties results from interfascicular differences.
234. Thorpe CT, Riley GP, Birch HL, Clegg PD, Screen HRC. Effect of fatigue loading on structure and functional behaviour of fascicles from energy-storing tendons. Acta Biomater [Internet]. Acta Biomater; 2014 [cited 2022 Nov 26];10:3217–24. Available from: https://pubmed.ncbi.nlm.nih.gov/24747261/
235. Kjaer M, Bayer ML, Eliasson P, Heinemeier KM. What is the impact of inflammation on the critical interplay between mechanical signaling and biochemical changes in tendon matrix? J Appl Physiol [Internet]. 2013;115:879–83. Available from: http://jap.physiology.org/cgi/doi/10.1152/japplphysiol.00120.2013
236. Choi HJ, Choi S, Kim JG, Song MH, Shim KS, Lim YM, et al. Enhanced tendon restoration effects of anti-inflammatory, lactoferrin-immobilized, heparin-polymeric nanoparticles in an Achilles tendinitis rat model. Carbohydr Polym. Elsevier Ltd; 2020;241:116284.
237. Zitnay JL, Lin AH, Weiss JA. Tendons exhibit greater resistance to tissue and

molecular-level damage with increasing strain rate during cyclic fatigue. Acta Biomater [Internet]. Elsevier; 2021 [cited 2021 Jul 26]; Available from: https://linkinghub.elsevier.com/retrieve/pii/S1742706121004839

238. Zitnay JL, Li Y, Qin Z, San BH, Depalle B, Reese SP, et al. Molecular level detection and localization of mechanical damage in collagen enabled by collagen hybridizing peptides. Nat Commun [Internet]. Nature Publishing Group; 2017 [cited 2018 May 16];8:14913. Available from: http://www.ncbi.nlm.nih.gov/pubmed/28327610

Appendix A

SBF-SEM FIXATION PROTOCOL

1. Tissues were cut into 1mm x 1mm segments and fixed with 2% glutaraldehyde and 2% paraformaldehyde in 0.1M sodium cacodylate buffer with 2mM calcium chloride. Samples were held in fixative at 4°C.
2. Samples were transferred to 2% glutaraldehyde containing 1% tannic acid in 0.1M sodium cacodylate buffer with 2mM calcium chloride and fixed overnight at 4°C.

Day 1:

1. Samples were washed 3 x 15 min with 0.1M sodium cacodylate buffer with 2mM calcium chloride
2. Incubate the samples in 2% osmium tetroxide in 0.15M cacodylate buffer with 2mM calcium chloride, pH 7.4, for 1.5 h at RT.
3. **Without a wash step**, remove the osmium tetroxide and incubate the samples in 2.5% potassium ferrocyanide in 0.15M cacodylate buffer with 2mM calcium chloride, pH 7.4, for 1.5 h at RT.
4. During the initial osmium incubation, prepare thiocarbohydrazide (TCH) solution. This reagent needs to be fresh and available right at the end of step 7 (see page 2).
    a. Add 0.1 g thiocarbohydrazide to 10 ml ddH_2O and place in a 60°C oven for 1 h, (agitate by swirling gently every 10 min to facilitate dissolving). Filter this solution through a 0.22 μm Millipore syringe filter right before use.
5. Samples were washed 3 x 15 min with 0.1M sodium cacodylate buffer
6. Incubate samples in the TCH solution (0.22 μm Millipore filtered) for 45 min at 40˚C.
7. Samples were washed 3 x 15 min in ddH_2O at RT.
8. Incubate samples in 2% osmium tetroxide in ddH_20 (NOT ferrocyanide reduced osmium) for 1.5 hrs. at RT.
9. Rinse samples in ddH_2O for 3 x 15 min at RT. You may need to transfer the samples to a new scintillation vial if there is a lot of osmium tetroxide residue present on the vial.
10. Incubate samples in 2% uranyl acetate and leave in a refrigerator (~4°C) overnight.

Day 2:

1. Next day, incubate the samples in the same solution for an additional 2 h at 50°C.
2. Rinse samples in ddH_2O for 3 x 15 min at RT followed by *en bloc* lead aspartate (see page 2) staining for 2 hrs. at 50°C (0.02 M lead nitrate in 0.03 M sodium aspartate, pH 5.5; Walton, j. Histochem Cytochem., 1979).
3. Prepare an aspartic acid stock solution by dissolving 0.998 g of L-aspartic acid in 250 ml of ddH_2O. Note: the aspartic acid will dissolve more quickly if the pH is 3.8. This stock solution is stable for 1-2 months if refrigerated.
    a. To make the stain dissolve 0.066 g of lead nitrate in 10 ml of aspartic acid stock and pH adjusted to 5.5 with 1N KOH. The lead aspartate solution is placed in a 60°C oven for 30 minutes (no precipitate should form).
    b. Wash samples with ddH_2O for 3 x 15 min at RT.
    c. Dehydrate samples with graded series of acetone (25%, 50%, 75%, 95%) for 1 h each. Samples can be held in 95% acetone overnight.

Day 3-12:

1. Dehydrate with 100% anhydrous acetone 2 x 1 h each
2. Infiltrate with 1 part propylene oxide: 1 part acetone for 1h
3. Infiltrate with 100% propylene oxide for 1 h
4. Infiltrate with EMBed-812 resin:
5. 1 part Embed-812: 3 parts propylene oxide for overnight
6. 1 part Embed-812: 2 parts propylene oxide for 8 h
7. 1 part Embed-812: 1 part propylene oxide for overnight
8. parts Embed-812: 1 part propylene oxide for 8 h
9. parts Embed-812: 1 part propylene oxide for overnight
10. 100% Embed-812 for 8 h with vacuum
11. 100% Embed-812 for overnight with vacuum
12. 100% Embed-812 for 8 h with vacuum
13. Polymerize samples in aluminum dishes with Embed-812 resin at 60˚C under vacuum for 48 hr.

Appendix B

IACUC APPROVAL

University of Delaware
Institutional Animal Care and Use Committee
Application to Use Animals in Research
(New and 3-Yr submission)

Title of Protocol: Synergistic ablation model of tendinosis	
AUP Number: 1296-2022-0	**← (4 digits only — if new, leave blank)**
Principal Investigator: Dawn Elliott, PhD	
Common Name (Strain/Breed if Appropriate): rat **Genus Species:** rattus norvegicus	
Date of Submission: 11/28/21	

Official Use Only

IACUC Approval Signature: [illegible], DVM

Date of Approval: 2.1.2022

Revised: 05/2020

Page **1** of **24**

Appendix C

PERMISSIONS

Figure 2.1 Rights Link: https://marketplace.copyright.com/rs-ui-web/mp/license/62998e50-e7a9-470e-97b3-64c1b05e929a/f0cd937d-9e2e-46e8-8e2f-6c8ad99c2ce7

Figure 2.2 Rights Link: https://marketplace.copyright.com/rs-ui-web/mp/license/66bcc720-cbd7-44c9-a003-05264a301d29/12d36615-86c3-4b08-ba83-17ad97e186a0

Figure 2.3 Rights Link: https://marketplace.copyright.com/rs-ui-web/mp/license/d7791795-f8ba-43b6-a30e-57f2b5a3ec3e/0d434729-ff7e-41e3-bf43-e7a1fda0a5f2

Figure 2.4 Rights Link: https://marketplace.copyright.com/rs-ui-web/mp/license/3e9da864-6acb-4c30-81f1-22a5cbe582ab/34d29a49-8c6f-4e61-bcaf-a4bdebbccf88

Figure 2.5 Rights Link: https://marketplace.copyright.com/rs-ui-web/mp/license/da98b376-ccae-4612-b4dd-1906a35d17fd/6294b7fe-38c3-4f05-b1b2-acb3cb890cd8

Chapter 3 Rights Link: https://s100.copyright.com/CustomerAdmin/PLF.jsp?ref=55ca00b7-43c1-42a6-9fd1-aeb967748a3c